The Interaction of Small Molecules and Short Intense Laser Fields

By

Arthur Gerald Russakoff

Dissertation

Submitted to the Faculty of the

Graduate School of Vanderbilt University

in partial fulfillment of the requirements

for the degree of

DOCTOR OF PHILOSOPHY

in

Physics

May, 2016

Nashville, Tennessee

Approved:

Kalman Varga, Ph.D.

Richard Haglund, Ph.D.

Volker Oberacker, Ph.D.

Norman Tolk, Ph.D.

Greg Walker, Ph.D.

To my brother for his love of knowledge.

To my mother and sister for their love and support.

And of course to my father.

Our Sundays together will always be precious to me.

They are the reason I became a scientist.

ACKNOWLEDGEMENTS

This work has been supported by the National Science Foundation (NSF) under Grants No. Phy 1314463 and No. IIA126117, and the Vanderbilt University Discovery Grant.

TABLE OF CONTENTS

LIST OF TABLES

LIST OF FIGURES

Chapter 1

Introduction

1.1 Ionization Induced by Intense Ultrashort Laser Fields

In 1905 Einstein began the quantum revolution with his famous paper on the photoelectric effect [1]. The quantum revolution fundamentally changed our philosophical and practical understandings of the physical universe. In 1917, Einstein expanded on his photoelectric effect work and proposed the stimulated emission. This prediction eventually lead to the invention of the laser in 1960 [2]. Since then the generation of laser fields has been greatly refined. Today laser pulses with femtosecond (10^{-15} s) duration are ubiquitous. The femtosecond is the time scale of motion for the molecular nuclei, and femtosecond pulses are therefore very important in probing the quantum chemistry [3]. Due to their smaller mass relative to the nuclei, electrons in small molecules move on an attosecond (10^{-18} s) time scale. While our focus is on the femtosecond pulses, attosecond pulses are generated more and more readily with each passing year [4].

Short pulses with intensities on the order of $10^{14} - 10^{15} \frac{\mathrm{W}}{\mathrm{cm}^2}$ may be readily generated on a small optical bench. At an intensity of $10^{15} \frac{\mathrm{W}}{\mathrm{cm}^2}$ the peak electric field is $\approx 8.68\,\mathrm{V/Å}$, where $\mathrm{Å} = 10^{-10}$ m. The peak electric field may be compared to the electric field at a distance of one Bohr radius (≈ 0.529 Å) from the nucleus of a hydrogen atom, which is $\approx 51.4\,\mathrm{V/Å}$. The peak field of the laser pulse is a significant fraction of the electric field experienced by an electron in the hydrogen atom. The high intensity and short duration of these pulses ensure that their effect on molecules is strictly nonperturbative.

The most fundamental ionization process is single-electron ionization driven by a linearly polarized laser field. At low intensity an electron may be ionized by absorbing multiple photons, as first predicted by Maria Göppert-Mayer [5]. An electron may even absorb more than the minimum number of photons, leading to the so called above threshold ion-

ization [6]. At higher intensity, the electric potential of the laser field will modulate the Coulomb well(s) of the atom or molecule. By lowering the potential barrier, the electron may tunnel into the continuum. The so called Keldysh parameter [7], which determines which of these ionization regimes applies, is given by,

$$\gamma = \sqrt{\frac{V_{\mathrm{IE}}}{2U_p}}. \tag{1.1}$$

In the above equation, V_{IE} is the vertical ionization potential of the molecule or atom, which is the minimum energy required to directly ionize one electron. U_p is the ponderomotive energy [8] of the laser field, which is the cycle averaged energy of a free electron driven by the laser field. U_p is given by,

$$U_p = \frac{e^2\langle E^2\rangle}{4m_e\omega^2}, \tag{1.2}$$

where e is the charge of the electron, m_e is the electron mass, ω is the angular frequency of the laser field, and $\langle E^2\rangle$ is the average of the electric field squared. If $\gamma >> 1$ then multiphoton ionization will dominate, and if $\gamma << 1$ then tunneling ionization will dominate. In this thesis we consider wavelengths of 800 nm and small molecules with ionization potentials of ≈ 10 eV. The lowest intensity we shall consider is $4 \cdot 10^{14} \frac{\mathrm{W}}{\mathrm{cm}^2}$. Given these parameters, $U_p \approx 23.9$ eV and $\gamma \approx 0.457$. This represents an upper bound on γ for the laser fields we will consider since γ decreases with higher intensity. When $\gamma < 0.5$, the Keldysh theory places the phenomena in the tunneling ionization regime. Hence tunneling ionization will dominate for the laser fields and molecules considered in this thesis. The Keldysh parameter, while useful, does not provide an exact or complete picture of the strong field laser phenomena. We will discuss the Keldysh parameter and its limitations in more detail in Chapter II.

The complexity of the ionization phenomena is greatly increased once the ionization of multiple electrons is considered since the correlation between electrons must be accounted for [9]. Broadly speaking, there are two possibilities for the multiple ionization. The first

is that the electrons are ionized one after another and their dynamics are independent of one another. This is so called sequential ionization. The second case is the nonsequential multiple ionization, where the electron dynamics are highly correlated. Nonsequential double ionization is observable, for instance, in the so called "knee" in the He^{2+} ion yield of helium [10–12]. The nonsequential double ionization has also been observed in the ion yields of molecules [13, 14].

An important and simple model of the ionization of two correlated electrons is the tunneling and recollision model proposed by Corkum [15] in 1993. In this model, an electron is first ionized via tunneling ionization. Then upon the reversal of the laser field the electron is driven back to the parent ion and ionizes a second electron through collision. The recolliding electron may instead recombine with the parent ion. The recombination converts the electron's kinetic energy into the generation of high harmonics of the fundamental laser frequency [16].

1.2 Ionization and Fragmentation of Small Molecules

Our interest in this thesis is the dynamics of both the electrons and the nuclei in a molecule driven by intense, ultrashort laser fields. The dynamics involves both the correlation between electrons, and the correlation between the electrons and the nuclei. In this section we consider some of the unique challenges posed by small molecules.

Small molecules have an orbital electronic structure. Each molecular orbital has a particular nodal symmetry, which may be calculated with electronic structure calculations using ab initio theories such as Hartree Fock or density functional theory. We shall discuss these ab initio theories in Chapter II. Early attempts to understand the ionization of molecules made use of the so-called molecular-orbital Ammosov, Delone, Krainov (MO-ADK) model [17]. The original Ammosov, Delone, Krainov (ADK) model [18] gave the tunneling ionization rates of an atom assuming a single, active electron interacting with a quasi-static external laser field. The main feature of the MO-ADK model is the assump-

tion that only the highest occupied molecular orbital (HOMO) interacts with the laser field. More deeply bound orbitals are treated as a frozen core. On the other hand, ionization from inner-valence molecular orbitals has been experimentally observed [19–21, 21–28]. Multiple ionization may occur from several orbitals either sequentially [25] or nonsequentially [28].

Unlike atoms, molecules have a geometric structure defined by the positions of the nuclei. Of particular importance is the alignment of the molecular geometry relative to the polarization vector of the laser field. Typically an ensemble of molecules are inserted into the experimental apparatus as a gas jet. These molecules, being in the gas phase, are initially aligned randomly. Recently, the use of pump-probe techniques has allowed the study of the ionization of aligned molecules [29–35]. In this experimental setup first a nonionizing pump pulse aligns the molecular ensemble along a particular axis. With an aligned system in hand, ionization and fragmentation may be induced by the probe pulse.

The fragmentation of molecules induced by strong laser fields involves the coupled dynamics between the electrons and the nuclei. The laser field will induce several fragmentation and ionization channels. Each channel has an associated quantum mechanical probability of occurring. Modern experimental tools such as the Cold Target Recoil Ion Momentum Spectroscopy [36] (COLTRIMS) allow a complete coincidence mapping of the final momentum of both the ionized electrons and the fragmented ions. From these coincidence measurements the ionization and fragmentation channel of each event may be determined.

Given that the probability of the various fragmentation channels of a molecule may be determined for a given laser pulse, one asks if a particular set of laser pulse parameters may be chosen which shall optimally drive the molecule along a desirable dissociation channel? More generally, can sculpted laser pulses be used to drive chemical reactions? This is the topic of the next section.

1.3 Quantum Control of Chemistry

The advent of ultrashort laser pulse durations brings the promise of quantum control of chemical reactions. Broadly speaking, the goal of chemistry is to drive a set of initial reactants towards a set of products. An active control of chemical reactions using short sculpted laser pulses is highly desirable as it would allow an enhancement of product yields with a minimization of waste products, or even allow reaction pathways not accessible in traditional chemistry. Quantum control has attracted considerable interest and many reviews are available [37–39]. In this section we highlight the most important aspects.

Progress in sculpting laser fields permitted early attempts at quantum control using open loop algorithms [40]. In such a scheme the known molecular properties are used to construct the optimal sculpted laser pulse using optimal control theory. These algorithms proved sensitive to disturbances and experimental uncertainties, leading to the development of robust quantum control [41] to construct sculpted pulses which are insensitive to disturbance.

Levis et al. [42, 43] introduced closed loop algorithms, which proved to be a significant advancement in the study of quantum control. There are two flavors of closed loop algorithms: machine learning and quantum feedback. In both cases the algorithm begins with some initial test pulse. With the machine learning, the pulse drives the reactants completely to their products. The yield of desired products is used to derive the shape of a new pulse. The experiment is repeated with identical initial reactants which are now driven by the newly constructed pulse. Several iterations of this scheme allow the construction of an optimal pulse. With quantum feedback, instantaneous feedback is obtained as the reactants are driven towards the products and the pulse parameters are adjusted in real time.

The most significant limitation on quantum control is pulse duration [37], with shorter pulses allowing for a more complete control over the dynamics. In recent years, laser pulses with sub-5 fs duration have been used to induce selective bond cleavage [44], and the steering of dissociation channels [45, 46]. Further advancements will be rapidly achieved

as attosecond pulses become more readily implemented into quantum control experiments.

1.4 Thesis Outlook

In this chapter we have discussed the phenomenology of the ionization of small molecules and atoms. We have also observed the long-standing desire for the quantum control of chemical reactions. The purpose of this thesis is to theoretically investigate the ionization and fragmentation of small molecules induced by intense, ultrashort laser fields. In particular we shall consider the coupling of electronic and nuclear dynamics, the dependence of molecular alignment, and the dependence on pulse intensity and duration for both linearly and circularly polarized femtosecond laser pulses. Our tool is *ab initio* time dependent density functional theory (TDDFT) coupled with Ehrenfest dynamics. We also consider algorithms to enhance the computational speed of the solution of the TDDFT equations.

In Chapter II we will review various *ab initio* theoretical approaches to the study of molecular systems with a particular emphasis on the TDDFT. We will also provide the computational details of our implementation. In Chapter III we shall investigate various time propagation schemes for the solution of the TDDFT equations in the pursuit of propagators which are both accurate and computationally efficient. In Chapter IV we shall use the TDDFT coupled with the Ehrenfest dynamics to investigate the ionization and fragmentation of small molecules driven by linearly polarized laser pulses. We shall find that the results are in agreement with an enhanced ionization (EI) model. In Chapter V we shall further investigate the EI model by considering fixed ion TDDFT calculations. In chapter VI we use the TDDFT coupled with the Ehrenfest dynamics to investigate the ionization and fragmentation of small molecules driven by circularly polarized laser pulses, and compare these results to the dynamics as driven by linearly polarized pulses. In Chapter VII we shall summarize and conclude the thesis.

Chapter 2

Theoretical Approaches

2.1 Many-Body Quantum Theory

Lying at the foundation of the non-relativistic many-body quantum theory is the time-dependent Schrödinger equation (TDSE),

$$i\hbar\frac{\partial\Psi(\mathbf{r_1},...,\mathbf{r_2})}{\partial t} = H\Psi(\mathbf{r_1},...,\mathbf{r_N}). \tag{2.1}$$

The two main ingredients of this equation are the Hamiltonian and the many-body wavefunction. As we are interested in the quantum chemistry of molecules, we shall restrict our focus to systems containing only electrons. The dynamics of the nuclei are also important, and we shall consider their treatment in section 2.6, Ab-initio Molecular Dynamics.

Since electrons are identical fermions, the many-body wavefunction must be antisymmetric, $\Psi(...,\mathbf{r_i},...,\mathbf{r_j},...) = -\Psi(...,\mathbf{r_j},...,\mathbf{r_i},...)$. The many-body wavefunction is extremely complicated as it is a function of $3N$ coordinates, $\mathbf{r_1},...,\mathbf{r_N}$, where N is the number of particles. The computational expense of solving the many-body TDSE becomes intractable for systems containing more than a few electrons. In this chapter we discuss the *ab initio* (first principles) theoretical advancements which have made tractable the solution of many-body quantum systems. In particular we consider the application of these *ab initio* theories to small molecules driven by intense, ultrashort laser fields.

2.2 Ab Initio Theories

The most straightforward ab initio theory would be the solution of the TDSE itself. However, as noted above, this remains intractable for more than a few electrons. The single-active-electron (SAE) approximation, in which one electron interacts with the laser field

and the others are frozen, has been successfully applied to atoms [47–50]. The application of the SAE approximation in three dimensions has proven successful for the H_2 molecule [51]. The SAE approximation has also been applied to the intense laser field ionization in three dimensions of other small molecules such as N_2, O_2, CO_2, and H_2O [52, 53]. Effects from multiple molecular orbitals have been considered within an independent-active-electron (IAE) approach, where each molecular orbital independently interacts with the laser field [52]. The SAE and IAE approaches do not account for either electron exchange or correlation effects.

Another ab initio approach is the time-dependent Hartree-Fock (TDHF) [54] theory. Hartree Fock makes the assumption that the many-body electron wavefunction may be approximated by a single optimal Slater determinant of non-interacting orbitals. Using a variational principle a set of Schrödinger-like equations for these non-interacting orbitals may be derived. One of the advantages of the Hartree Fock theory is that it includes exactly the effects of electron exchange. Pioneering efforts in the application of TDHF to the ionization of atoms was made by Kulander [55] in 1987. The TDHF has been applied to the study of the optical properties of molecules [56, 57], the strong field ionization of acetylene [58–60], and the dissociation of ethylene [61].

Of particular relevance to this thesis is the density functional theory (DFT) [62] and its extension into the time domain, the time-dependent density functional theory (TDDFT) [63, 64]. TDDFT remains one of the most robust tools in the study of strong field phenomena, and has become ubiquitous to the investigation of the strong field excitation and ionization of atoms and small molecules. With coupling to a molecular dynamics scheme, the TDDFT has also been applied to the dissociation of small molecules. Among the phenomena investigated are the correlated double ionization of helium [65, 66], the high-order harmonic generation [67–69], and the Coulomb explosion of various molecules [70–74]. In the next section we shall discuss the formalism of the DFT theory, which lies at the foundation of TDDFT. In the subsequent section we shall discuss the formalism of the

TDDFT.

2.3 Density Functional Theory Formalism

DFT is one of the most powerful ab initio theories. From a formal mathematical point of view, DFT is an exact reformulation of the time independent Schrödinger equation of many-body quantum theory. DFT is strictly a ground state theory. The extension of DFT to include excited states and time-dependence may be found in the TDDFT, which is discussed in the next section. We shall begin with a sketch of the formal foundations of the DFT, motivating and stating the relevant theorems without proof. More complete discussions and formal proofs may be found in many textbooks, for instance in Ref. [75]. We shall conclude with a discussion of the approximations required for practical use of the theory.

In the usual quantum theory all of the information about the ground state of a physical system is contained within the ground state many-body wavefunction, Ψ_0. DFT instead takes the ground state one-body density $\rho_0(\mathbf{r})$ as the fundamental physical quantity. The foundations of the DFT theory are the Hohenberg-Kohn (HK) theorems [76]. They establish that the density also contains all of the information about the physical system. The first theorem is as follows:

Theorem 1: *For every ground state density, ρ_0, the external potential, V_{external} is uniquely determined up to a choice of additive constant.*

The external potential here may be, for instance, an applied electric field or the Coulomb wells generated by atomic nuclei. As Hohenberg and Kohn [76] explain, through the Schrödinger equation V_{external} uniquely determines the ground state wavefunction, Ψ_0. From Ψ_0 any physical observable, and in particular the ground state energy, $\langle\Psi_0|H|\Psi_0\rangle$, may be determined. Hence the ground state energy is uniquely determined once the external potential is specified. Since Theorem 1 states that ρ_0 determines the external potential,

and since the external potential uniquely determines the ground state energy, mathematically there must exist a functional which maps the ground state density to the ground state energy. More formally, we have theorem 2:

Theorem 2: *There exists a universal energy functional:*
$E[\rho(\mathbf{r})] = F[\rho(\mathbf{r})] + \int V_{\text{external}}(\mathbf{r}) \cdot \rho(\mathbf{r}) d\mathbf{r}$.
The minimum of this functional is the ground state energy, and is obtained when $\rho(\mathbf{r}) = \rho_0(\mathbf{r})$.

While Theorem 2 establishes the existence of the energy functional it does not tell us how to construct it. In 1965, Kohn and Sham [77] partitioned the so called Hohenberg-Kohn functional, $F[\rho]$, into three parts,

$$F[\rho] = T[\rho] + \frac{e^2}{2} \int \int \frac{\rho(\mathbf{r})\rho(\mathbf{r}')}{|\mathbf{r} - \mathbf{r}'|} + E_{xc}[\rho]. \tag{2.2}$$

The first term in the above equation is the total kinetic energy. The second is the Hartree energy, which is simply the electrostatic Coulomb energy between the electrons. The third is the so called exchange-correlation energy. Through a variational principle in which one minimizes the energy functional, a Schrödinger-like equation for N fictitious non-interacting electrons, known as the Kohn-Sham equation, can be obtained,

$$E_k \phi_k(\mathbf{r}) = H_{\text{KS}}[\rho_0]\phi_k(\mathbf{r}). \tag{2.3}$$

The Kohn-Sham orbitals, ϕ_k, exactly reproduce the ground state electron density,

$$\rho_0 = \sum_{k=1}^{N} 2 |\phi_k|^2 . \tag{2.4}$$

The factor of 2 in the above equation represents spin degeneracy. We shall not concern

ourselves with spin dependence in this thesis.

The careful reader observes that one needs ρ_0 to solve Eq. (2.3) for ϕ_k, but simultaneously requires ϕ_k to calculate ρ_0. In practice this complication is overcome by solving eqs. 2.3 and 2.4 self consistently. We briefly sketch this algorithm. First choose an initial guess for ϕ_k and use this guess to calculate ρ_0. Compute $H_{\mathrm{KS}}[\rho_0]$ and solve Eq. (2.3) to obtain an updated guess for ϕ_k. Repeat these steps until ρ_0 converges. Now that we know how to solve the DFT equations, let us turn to the construction of the Kohn-Sham Hamiltonian.

The Kohn-Sham Hamiltonian is given by,

$$H_{\mathrm{KS}}[\rho_0] = -\frac{\hbar^2}{2m}\nabla^2 + V_{\mathrm{external}} + V_{\mathrm{Hartree}}[\rho_0] + V_{\mathrm{XC}}[\rho_0]. \tag{2.5}$$

Observe that each term in the Hamiltonian corresponds to one of the terms in the Kohn-Sham partitioning of the energy functional. The first term is the kinetic energy operator. The second term is the external potential. The third term is the Hartree potential, given by

$$V_{\mathrm{Hartree}} = \int \frac{\rho_0(\mathbf{r}')}{|\mathbf{r}-\mathbf{r}'|} d\mathbf{r}'. \tag{2.6}$$

The final term is the exchange-correlation (XC) potential.

Up until now the theorems and equations that we have written down have been formally exact. Compared to the time independent Schrödinger equation, the DFT promises a computationally tractable solution for the ground state of many-body quantum systems. Unfortunately, the XC potential is unknown and will likely remain so for the foreseeable future. The XC potential must therefore be approximated, and it is here that the practical DFT theory diverges from the ground state many-body quantum theory. Many approximations are currently in use [78], and we give a quick overview here. The simplest XC potential is the the local density approximation (LDA) [79], where the XC potential is approximated as the exact XC potential of a homogeneous degenerate electron gas. The generalized gradient approximation (GGA) [79] class of XC potentials makes use of functionals of the

gradient of the density in addition to the density itself. Other examples of XC potentials in current use include the meta-GGA functionals [80] and Van der Waals functionals [81]. Despite the advancements in developing these XC potentials, a general XC potential which has both broad applicability and accurate predictions remains elusive.

The DFT remains one of the robust and powerful ab initio theories. With the foundation laid in this section we may now proceed into the time domain with TDDFT.

2.4 Time Dependent Density Functional Theory Formalism

In the year 1984, Runge and Gross extended the DFT to time-dependent systems [82]. The foundation of DFT was that the ground state density uniquely determined the external potential. Similarly, Runge and Gross lay the foundation of TDDFT with the following theorem:

Theorem 1: *Given a known initial state, Ψ_0, and a time-dependent single-particle potential, $v(\mathbf{r},t)$, there exists a unique density, $\rho(\mathbf{r},t)$, obtained by solving the Schrödinger equation. Similarly, for every time-dependent density, $\rho(\mathbf{r},t)$, there exists a single-particle potential, $v(\mathbf{r},t)$, which is uniquely determined up to a choice of additive constant.*

The proof may be found in the original paper by Runge and Gross [82]. Runge and Gross proceeded to prove that there exists a time-dependent Kohn-Sham equation,

$$i\hbar\frac{\partial\phi_k(\mathbf{r},t)}{\partial t} = H_{\mathrm{KS}}[\rho]\phi_k(\mathbf{r},t). \tag{2.7}$$

The solution of this equation gives the time-dependent Kohn-Sham orbitals, which may be used to construct the true time-dependent density of the many-body quantum theory,

$$\rho(\mathbf{r},t) = \sum_{k=1}^{\infty} 2|\psi_k(\mathbf{r},t)|^2. \tag{2.8}$$

The time-dependent Kohn-Sham Hamiltonian is given by,

$$H_{\mathrm{KS}}[\rho] = -\frac{\hbar^2}{2m}\nabla^2_{\mathbf{r}} + V_{\mathrm{H}}[\rho](\mathbf{r},t) + V_{\mathrm{XC}}[\rho](\mathbf{r},t) + V_{\mathrm{ext}}(\mathbf{r},t). \tag{2.9}$$

Again we have the kinetic energy operator, the Hartree potential, an exchange-correlation potential, and an external potential.

The benefits of the TDDFT are the same as the DFT, which is a much improved computational cost relative to the time-dependent many-body Schrödinger equation. The weakness of the TDDFT is the also the same, which is that the exact time-dependent exchange-correlation potential is unknown. One might expect that the exchange-correlation potential is a functional of the density at a given time, t. However it is well known that V_{XC} has a so called memory effect where its functional form depends on the entire history of the density. Nevertheless, one of the most common and well tested approaches to approximating the exchange-correlation potential is the so called adiabatic approximation. Here the form of the exchange-correlation potential is taken to be the ground state functional from DFT with the density at time t inserted. That is,

$$v_{XC}^{\mathrm{adiabatic}}[\rho(\mathbf{r},t)] = v_{XC}^{\mathrm{gs}}[\rho(\mathbf{r},t)]. \tag{2.10}$$

Any of the exchange-correlation potentials discussed in the previous section may be used as v_{XC}^{gs}. With the insertion of the LDA XC potential one obtains the adiabatic LDA (ALDA).

Optical properties, such as the absorption spectrum, may be determined through the Linear Response TDDFT (LR-TDDFT), introduced by Casida [83] in 1995. The LR-TDDFT equations are derived by inserting a first order perturbation for the external potential into Eq. (2.7). The resulting equations are very cheap, computationally speaking. In this thesis we consider the effects of strong fields and the LR-TDDFT does not apply. Non-perturbative TDDFT may be obtained through the direct solution of the Kohn-Sham equations. In practice, this is accomplished through the construction of a time propagator.

In Chapter III we shall discuss the theory of the propagator and investigate various schemes for its approximation.

2.5 Electrodynamics and Gauge Choice

In the previous section we laid out the formalism of the TDDFT theory. We are nearly in a position to put this formalism to use for practical application to many-body electron systems. First we must introduce the external potentials which will drive the electron dynamics, i.e. the applied laser field and the Coulomb potentials generated by the nuclei. In this section we will discuss the laser fields. We begin with a discussion of the fundamental electrodynamics. We next discuss gauge choice, and in particular introduce the length gauge. We shall also motivate the dipole approximation and demonstrate its applicability to the laser fields considered in this thesis.

The application of the TDDFT to systems involving the interaction of molecules and strong laser fields involves the coupling of the time-dependent Kohn-Sham equations with the Maxwell's equations of the electrodynamics. Strictly speaking, this coupling is not theoretically rigorous unless a closed surface may be found on which the Kohn–Sham orbitals are zero at all times. If such a surface cannot be found then the Runge-Gross theorem is invalid and TDDFT does not apply. Maitra et al. [84] showed that the Runge-Gross theorem is violated by a homogeneous field applied to a bulk material. The failure of the Runge-Gross theorem in this case is nontrivial, and the resolution of this complication requires the time-dependent current density functional theory (TDCDFT) of Ghosh-Dhara [85]. In the TDCDFT the fundamental variable is the single-particle current density. Our interest is in small molecules rather than bulk materials, and we shall work within the adiabatic approximation where the Hamiltonian is only a functional of the density. With these assumptions we may continue to use the TDDFT theory as developed thus far.

The Maxwell's equations written in differential form are given by,

$$\nabla \cdot \mathbf{E} = \frac{\rho}{\varepsilon_0} \tag{2.11}$$

$$\nabla \cdot \mathbf{B} = 0 \tag{2.12}$$

$$\nabla \times \mathbf{E} = -\frac{\partial \mathbf{B}}{\partial t} \tag{2.13}$$

$$\nabla \times \mathbf{B} = \mu_0 \left(\mathbf{J} + \varepsilon_0 \frac{\partial \mathbf{E}}{\partial t} \right) \tag{2.14}$$

For the construction of a quantum mechanical Hamiltonian, potentials are required instead of electric and magnetic fields. The scalar potential, U, and vector potential, $\mathbf{A}$, are related to the electric and magnetic fields by,

$$\mathbf{B} = \nabla \times \mathbf{A} \tag{2.15}$$

$$\mathbf{E} = -\nabla U - \frac{1}{c} \frac{\partial \mathbf{A}}{\partial t}. \tag{2.16}$$

Before moving forward to the integration of the Maxwell's equations to the TDDFT theory, we first ask if the non-relativistic many-body quantum theory formalism is applicable to the laser fields under consideration. One such measure may be found [86, 87] in the following unitless intensity parameter,

$$z_f = \frac{2U_p}{m_e c^2}, \tag{2.17}$$

where U_p is the ponderomotive energy, and m_e is the electron rest mass. If $z_f << 1$ then the regime is non-relativistic. The largest intensity we shall consider in this thesis is $14 \cdot 10^{14} \frac{\mathrm{W}}{\mathrm{cm}^2}$, for which the ponderomotive energy is $U_p = 83.66$ eV. Since $m_e c^2 = 0.511 \cdot 10^6$ eV, one is well justified in using the non-relativistic theory.

The vector potential may be incorporated into the time-dependent Kohn-Sham equations by replacing the momentum operator, $\hat{p} = i\hbar\nabla$, with $\hat{p} - \frac{e}{c}\hat{A} = i\hbar\nabla - \frac{e}{c}\hat{A}$. This re-

placement yields Kohn-Sham equations of the form,

$$i\hbar\frac{\partial\phi_k(\mathbf{r},t)}{\partial t}=\left[\frac{1}{2m_e}(i\hbar\nabla_{\mathbf{r}}-\frac{e}{c}\mathbf{A}(\mathbf{r},t))^2+V_{\mathrm{H}}[\rho](\mathbf{r},t)+V_{\mathrm{XC}}[\rho](\mathbf{r},t)+V_{\mathrm{ions}}(\mathbf{r},t)+U(\mathbf{r},t)\right]\phi_k. \tag{2.18}$$

Now let us turn to the question of whether the magnetic field is relevant to the dynamics or may be safely neglected. In Chapter I, we introduced the concept of the Keldysh parameter, Eq. (1.1). It was observed that low intensities would give a large Keldysh parameter, and that this implied that multi-photon ionization would dominate the physical phenomena. At high intensities, the laser field could be considered a classical field which would modulate the Coulomb wells of the atom or molecule. This modulation would induce tunneling ionization. Implicit to this discussion were the assumptions that the magnetic field of the laser was negligibly small and that the laser fields are quasi-static. As Reiss [86, 87] points out, the success of the Keldysh parameter has relied on the accident that wavelengths of 800 nm, the typical wavelength of Ti:Sapphire lasers, and 1 μm, the typical wavelength of Nd lasers, are experimentally convenient and in wide use. Strictly speaking, one must show that the magnetic field of the laser is negligible before applying the tunneling theory of Keldysh. We shall now show that this is the case for wavelengths of 800 nm, which is the regime we wish to consider.

In order to judge the importance of the magnetic field, Reiss [86] suggests that one considers the classical motion of a free electron driven by a strong linearly polarized electromagnetic plane wave. For convenience, consider the frame of reference where the average motion of the electron is at rest. For a plane wave, the electric field will take the form $\mathbf{E}=E_0\hat{n}\cos(k\cdot r-\omega t+\delta)$, where E_0 is the amplitude of the electric field, $\hat{n}$ is the polarization vector, k is the wave vector, ω is the angular frequency, δ is the phase. If the magnetic field is negligibly small then the classical dynamical equation of motion for the

electron becomes

$$\mathbf{F} = -e\mathbf{E} - e\left(\mathbf{v} \times \mathbf{B}\right) = -eE_0\hat{n}\cos(\mathbf{k}\cdot\mathbf{r} - \omega t + \delta) = m_e\frac{d^2\mathbf{r}}{dt^2}, \tag{2.19}$$

where e is the elementary charge, and m_e is the mass of the electron. By solving this differential equation, one finds that the electron will engage in a simple harmonic oscillatory motion parallel to the electric field, with a given amplitude. As the magnetic field is ramped up the motion will become a figure eight (see e.g. [88]) with an additional amplitude parallel to the propagation vector of the laser field, β_0, given by

$$\beta_0 = \frac{U_p\lambda}{8\pi(1+z_f)m_ec^2} \approx \frac{U_p\lambda}{8\pi m_ec^2}. \tag{2.20}$$

In the above equation, U_p is the ponderomotive energy of the laser field, c is the speed of light, m_e is the mass of the electron, λ is the wavelength of the laser field, and z_f is the unitless parameter introduced in eq. (2.17). The amplitude of the figure eight parallel to the electric field is longer than the amplitude of the figure eight parallel to the propagation vector.

If $\frac{\beta_0}{a_0} << 1$, where a_0 is the Bohr radius, then the magnetic field is negligible. Once again, the maximum intensity we shall consider is about $10^{15}\frac{\mathrm{W}}{\mathrm{cm}^2}$, and the wavelength is 800 nm. This gives an upper bound of $\frac{\beta_0}{a_0} \approx 0.0985$, implying that magnetic fields may safely be neglected.

2.5.1 Choice of Gauge

Classically, it is well known that only the electric and magnetic fields represent true physical quantities and that the potentials are only defined up to a choice of gauge. The

so-called gauge transformations are induced as follows,

$$\begin{aligned} \mathbf{A}'(\mathbf{r},t) &= \mathbf{A}(\mathbf{r},t) + \nabla\chi(\mathbf{r},t) \\ U'(\mathbf{r},t) &= U(\mathbf{r},t) - \frac{\partial}{\partial t}\chi(\mathbf{r},t). \end{aligned} \tag{2.21}$$

Since the gauge transformation does not effect a change in the electric and magnetic fields, the classical electrodynamics is said to be gauge invariant.

In quantum mechanics, a gauge transformation will simply lead to a unitary transformation of the wavefunction. Since physical observables, which are the expectation values of operators, are invariant under unitary transformation, gauge invariance is preserved in the quantum mechanics.

The Kohn-Sham equations with the adiabatic approximation to the XC functional are also gauge invariant. This may be formally proven by first turning to the TDCDFT, which is formally gauge invariant. By showing that the TDCDFT reduces to the normal TDDFT under adiabatic conditions, the TDDFT theory in the adiabatic approximation is also shown to be gauge invariant [89]. In practice gauge invariance may be lost since one must choose an incomplete basis on which to represent the KS orbitals and the Hamiltonian. The accuracy produced with a given truncated basis will vary with gauge choice [89], breaking the gauge invariance. The gauge and basis in TDDFT must be chosen with some care if high accuracy is desired.

One of the most useful gauges in the study of plane waves is the Coulomb gauge,

$$\nabla \cdot \mathbf{A}(\mathbf{r},t) = 0. \tag{2.22}$$

This gauge is fully consistent with the complete Maxwell's equations including both magnetic and electric fields.

As we have noted above, for the intensities and wavelengths which are considered in this thesis the magnetic field is negligibly small. This is the origin of the so called dipole

approximation. Within the dipole approximation, the Coulomb gauge reduces to the so called velocity gauge,

$$\begin{aligned} \mathbf{A}(t) &= -c\int_0^t \mathbf{E}(t^{'})dt^{'}, \\ U(t) &= 0. \end{aligned} \tag{2.23}$$

Now the scalar potential is 0 and the vector potential is a function only of the time-dependent electric field. A derivation of Eq. (2.23) may be found in, for example, [90].

Still working within the dipole approximation, one may choose to instead eliminate the vector potential in favor of the scalar potential. This leads to the so called length gauge, which was first introduced by Göppert-Mayer [5]. The potentials in this gauge take the form,

$$\begin{aligned} \mathbf{A}(\mathbf{r},t) &= \mathbf{0}, \\ U(\mathbf{r},t) &= -\mathbf{r}\cdot\mathbf{E}(\mathbf{r},t). \end{aligned} \tag{2.24}$$

The length gauge is highly favorable for its simplicity of form and is therefore in wide use. A derivation of the form of the scalar potential found in Eq. (2.24) starting with the plane wave solution of the Maxwell's equations in the position gauge may be found here [91].

As shown in this section, one may safely ignore the magnetic field for the laser field parameters under consideration in this thesis. We are therefore justified in the use of the length gauge and dipole approximation.

2.6 Ab Initio Molecular Dynamics

In this section we review a few of the common ab-initio molecular dynamics schemes. In particular, we shall consider the Born-Oppenheimer and Ehrenfest molecular dynamics. A more complete review of the ab-initio molecular dynamics may be found, for instance,

in Ref. [92]. Our particular interest is the Ehrenfest dynamics.

Up until now we have considered the nuclei of molecules only as an external potential of the many-body electron system. The full molecular wavefunction must involve coordinates for both the electrons and the nuclei, giving $\Psi(\mathbf{r_1},...,\mathbf{r_{N_{\text{electron}}}},\mathbf{R_1},...,\mathbf{R_{N_{\text{nuclei}}}})$. The full many-body molecular wavefunction may be made tractable by recalling that the electrons and nuclei move on the attosecond and femtosecond time scales, respectively. This suggests that the wavefunction may be approximated as a product of an electron wavefunction and a nuclei wavefunction,

$$\begin{aligned}\Psi(\mathbf{r_1},...,\mathbf{r_{N_{\text{electron}}}},\mathbf{R_1},...,\mathbf{R_{N_{\text{nuclei}}}}) &= \sum_{\lambda}\Psi_e^{\lambda}(\mathbf{r_1},...,\mathbf{r_{N_{\text{electron}}}})\cdot\Psi_n^{\lambda}(\mathbf{R_1},...,\mathbf{R_{N_{\text{nuclei}}}}) \\ &= \Psi_e(\mathbf{r_1},...,\mathbf{r_{N_{\text{electron}}}})\cdot\Psi_n(\mathbf{R_1},...,\mathbf{R_{N_{\text{nuclei}}}}),\end{aligned} \tag{2.25}$$

where λ is set equal to 1. This is the so-called Born-Oppenheimer approximation, first proposed in 1927 [93].

Next one must decide how to approach the nuclear and electronic wavefunctions. We shall work within either the DFT or the TDDFT to describe the electron system. To make the nuclear dynamics tractable, we shall consider the nuclei as point particles which move along classical trajectories. Born and Oppenheimer proposed a further approximation that these classical trajectories move along a Potential Energy Surface (PES) which is derived from the ground state electronic wavefunction [93]. This scheme is known as the Born-Oppenheimer molecular dynamics (BOMD). Using the Ehrenfest theorem [94], the forces which drive the motion of the nuclei are calculated by taking derivatives of the ground state electronic energy with respect to the ionic positions. In the case of DFT this gives,

$$M_j\frac{d^2R_j}{dt^2} = \nabla_j E_{KS}[\rho_0], \tag{2.26}$$

where ρ_0 is the ground state density. Hence in each molecular dynamics (MD) step, one

first calculates the ground state electronic density using DFT for a given set of nuclear coordinates. Then one updates the nuclear coordinates using Eq. (2.26) and repeats the process. Since the BOMD deals only with the ground state electronic energy, it necessarily will not produce the correct dynamics in cases where the electronic wavefunction significantly diverges from the ground state. For this reason the BOMD is often referred to as an adiabatic molecular dynamics. We note that the term adiabatic here is used in a different sense than in the adiabatic exchange-correlation potentials discussed in previous sections.

One non-adiabatic classical trajectory approach is the so-called Ehrenfest dynamics. In this case one takes derivatives of the total electronic energy of TDDFT with respect to the ionic positions,

$$M_j \frac{d^2 R_j}{dt^2} = \nabla_j E_{KS}[\rho]. \tag{2.27}$$

One solves Eq. (2.27) simultaneously with the equations of TDDFT. In adiabatic BOMD, one solves for the electronic ground state and then calculates the forces on the ions. This implies that the BOMD provides an incomplete picture in cases where the electronic excited states are significantly occupied. The nonadiabatic Ehrenfest approach is therefore favorable in these cases, since the effects of excited states is accounted for.

The benefit of the ab-initio classical trajectory methods are their computational tractability. Nonetheless any classical trajectory method, whether adiabatic or non-adiabatic, will necessarily suffer from some drawbacks. For instance, in the case of molecular dissociation multiple fragmentation channels are possible. The Ehrenfest dynamics give only one set of nuclear trajectories and represent some averaging of the possible fragmentation channels. A calculation of the nuclear wave function would allow access to all of these fragmentation channels. We shall discuss these wave function approaches in Chapter VII, wherein we consider the outlook for future research in the field of quantum chemistry.

2.7 Our TDDFT Code Implementation

In this chapter we have discussed the formalism of TDDFT, described the ALDA[79] exchange-correlation functional, specified the form of the electrodynamic potentials in the length gauge, and described the nonadiabatic Ehrenfest dynamics. In this section put these pieces together and introduce the additional details which fully specify the implementation used in our research group. In particular we shall describe the implementation as used in chapters IV, V, and VI. In Chapter III most of the details are the same, with the exception of the different time propagation schemes implemented.

The first additional detail which must be specified is the basis on which the TDDFT equations are solved. We make use of a real space basis, where the KS orbitals are represented at discrete points. The advantage of this method is its flexibility. In practice these discrete points are organized in a uniform rectangular grid. The accuracy of the simulations are controlled by adjusting a single parameter, the grid spacing.

At the walls of the simulation cell we enforce the boundary condition that the Kohn-Sham orbitals are zero. When a strong laser field is applied, ionization may occur and the zero-boundary condition can lead to an unphysical reflection of the wavefunction off the walls of the simulation cell. To prevent this we implement a complex absorbing potential (CAP) with the following form, given by Manolopoulos [95]:

$$-iw(x) = -i\frac{\hbar^2}{2m}\left(\frac{2\pi}{\Delta x}\right)^2 f(y), \tag{2.28}$$

where x_1 is the start and x_2 is the end of the absorbing region, $\Delta x = x_2 - x_1$, $c = 2.62$ is a numerical constant, m is the electron's mass and

$$f(y) = \frac{4}{c^2}\left(\frac{1}{(1+y)^2} + \frac{1}{(1-y)^2} - 2\right), \quad y = \frac{(x-x_1)}{\Delta x}. \tag{2.29}$$

An example of a complex absorbing potential using the above form is shown in Fig. 2.1.

As the molecule is ionized by the laser field, electron density will travel to the edge of the simulation box where it is absorbed by the CAP. The total electron number, The integral of the electron density over the volume of the box,

$$N(t) = \int_V \rho(\mathbf{r},t) d^3x, \tag{2.30}$$

where V is the volume of the simulation box, will therefore diverge from the initial electron number, $N(0)$. Since, in general, $N(t)$ is not an integer, we will refer to it henceforth as the fractional electron number. We interpret $N(0) - N(t)$ as the total ionization of the molecule.

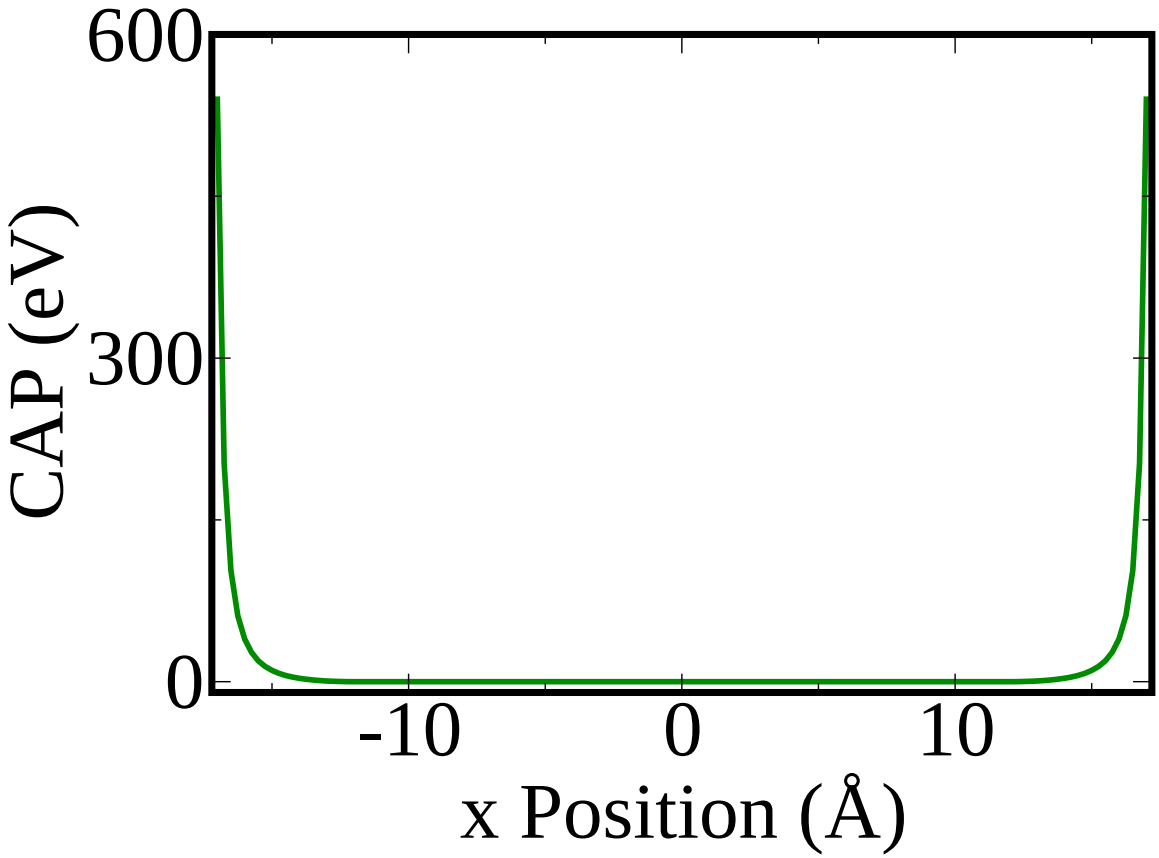

Figure 2.1: One dimensional representation of the magnitude of two complex absorbing potentials (CAP). The first CAP has $x_1 = -12\,\text{Å}$ and $x_2 = -17\,\text{Å}$. The second CAP has $x_1 = 12\,\text{Å}$ and $x_2 = 17\,\text{Å}$.

In an atom, the electrons occupy atomic orbitals. Each atomic orbital has its own binding energy and some electrons are more deeply bound than others. Electrons that are very deeply bound, the so called core electrons, do not participate in chemistry. Their ionization probabilities in the strong fields we shall consider are also small. The wavefunctions of these core electrons tend to oscillate rapidly, making them difficult to represent on a real space grid. In practice one may take the approximation of simulating only the dynamics of the valence electrons, which are not so deeply bound, and freeze the core electrons. To represent the Coulomb well of the atomic nucleus and the frozen core electrons we the use norm-conserving Troullier-Martins pseudopotentials [96]. These pseudopotentials preserve the scattering properties of the nucleus+core electron system.

Before the TDDFT calculation begins, the ground state of the system is prepared by performing a DFT calculation. Next, the time-dependent Kohn-Sham orbitals, $\psi_k(\mathrm{r},t)$, are determined by solving the time-dependent Kohn-Sham equation

$$i\hbar\frac{\partial\psi_k(\mathbf{r},t)}{\partial t} = H\psi_k(\mathbf{r},t), \tag{2.31}$$

where k is a quantum number labelling the orbital. The Kohn-Sham Hamiltonian is given by

$$H = -\frac{\hbar^2}{2m}\nabla^2_{\mathbf{r}} + V_{\mathrm{H}}[\rho](\mathbf{r},t) + V_{\mathrm{XC}}[\rho](\mathbf{r},t) + V_{\mathrm{ext}}(\mathbf{r},t). \tag{2.32}$$

Here ρ denotes the electron density, which is defined by a sum over all occupied orbitals:

$$\rho(\mathbf{r},t) = \sum_{k=1}^{\infty} 2|\psi_k(\mathbf{r},t)|^2, \tag{2.33}$$

where the factor of 2 accounts for there being two electrons in each orbital (via spin degeneracy).

V_{H} in Eq. (2.32) is the Hartree potential, defined by

$$V_{\mathrm{H}}[\rho](\mathbf{r},t) = \int d\mathbf{r}' \frac{\rho(\mathbf{r}',t)}{|\mathbf{r}-\mathbf{r}'|}, \tag{2.34}$$

and accounts for the electrostatic Coulomb interactions between electrons. V_{XC} is the exchange-correlation potential, whose exact form is a complicated functional of the entire history of the electron density. This functional is approximated using the adiabatic local-density approximation (ALDA) with the parameterization of Perdew and Zunger [79]. The last term in Eq. (2.32), V_{ext}, is the external potential, which includes the implicitly time–dependent potential due to the ions, V_{ion}, and the explicitly time-dependent potential due to the electric field of the laser V_{laser}. V_{ion} is a sum of norm-conserving pseudopotentials of the form given by Troullier and Martins [96] centered at each ion.

We are interested in the dynamics driven by both linearly and circularly polarized fields. V_{laser} is given by the dipole approximation in the length gauge: $V_{\mathrm{laser}} = \mathbf{r}\cdot\mathbf{E}(t)$. A linearly polarized electric field has the form,

$$\mathbf{E}(t) = E_{\max} \exp\left[-\frac{(t-t_0)^2}{2a^2}\right] \hat{\mathbf{k}} \sin(\omega t). \tag{2.35}$$

The parameters a, t_0, and $E_{\max}$ define the width, initial position of the center, and the maximum amplitude of the Gaussian envelope, respectively. ω describes the frequency of the laser, and $\hat{\mathbf{k}}$ is a unit vector defining the polarization of the electric field.

A time-dependent circularly polarized electric field is given by,

$$\mathbf{E}(t) = E_{\max} \exp\left[-\frac{(t-t_0)^2}{2a^2}\right] \Bigg(\hat{\mathbf{k_1}} \sin(\omega t) + \hat{\mathbf{k_2}} \sin(\omega t + \frac{\pi}{2}) \Bigg). \tag{2.36}$$

Here $\hat{\mathbf{k_1}}$ and $\hat{\mathbf{k_2}}$ are the orthogonal unit vectors defining the polarization of the circularly polarized electric field.

The time-dependent orbitals may be formally time-propagated from the initial state to some time, t, by using the time-evolution operator,

$$U(0,t) = \mathscr{T} \exp\left[-\frac{i}{\hbar}\int_0^t H(\mathbf{r},t')dt'\right], \tag{2.37}$$

where $\mathscr{T}$ denotes time ordering. In practice, $U(t,0)$ is split into a product of multiple time-evolution operators, each corresponding to a short time step δt,

$$U(0,t) = \prod_q U(t_q, t_q+\delta t), \quad t_q = q\delta t. \tag{2.38}$$

In Chapters IV, V, and VI, the time-dependent orbitals are propagated using a fourth-order Taylor expansion of the propagator, so that the propagation of the Kohn-Sham orbitals over a very short time step, δt, is given by,

$$\psi_k(\mathbf{r}, t_q+\delta t) \approx \sum_{n=0}^{m} \frac{1}{n!}\left(-\frac{i\delta t}{\hbar}H(\mathbf{r},t_q)\right)^n \psi_k(\mathbf{r},t_q), \tag{2.39}$$

where $m = 4$. The operator is applied for N time steps until the final time, $t_{\text{final}} = N \cdot \delta t$, is obtained. While the Taylor-propagation is not unconditionally stable, for time steps chosen to suitably small the propagation is numerically stable. The advantage of the Taylor-propagation is that its simple form only requires the repeated action of the Hamiltonian on the Kohn-Sham orbitals.

Motion of the ions in the simulations are treated classically. Using the Ehrenfest dynamics, the quantum forces on the ions due to the electrons are given by the derivatives of the expectation value of the total electronic energy with respect to the ionic positions. These forces are then fed into Newton's Second Law, giving

$$\begin{aligned} M_i \frac{d^2\mathbf{R}_i}{dt^2} = Z_i \mathbf{E}_{\text{laser}}(t) + \sum_{j\neq i}^{N_{\text{ions}}} \frac{Z_i Z_j (\mathbf{R}_i - \mathbf{R}_j)}{|\mathbf{R}_i - \mathbf{R}_j|^3} \\ - \nabla_{\mathbf{R}_i} \int V_{\text{ion}}(\mathbf{r},\mathbf{R}_i)\rho(\mathbf{r},t)d\mathbf{r}, \end{aligned} \tag{2.40}$$

where M_i and Z_i are the mass and pseudocharge (valence) of the i-th ion, respectively, and N_{ions} is the total number of ions.

Chapter 3

Time Propagation Algorithms for the Time Dependent Density Functional Theory

3.1 Introduction

Solving the equations of TDDFT in real-time requires the construction of a time propagation operator. This construction tends to be very expensive, and the development of new propagation schemes is highly desirable. In this chapter we consider two propagation schemes in which the propagator is constructed on a reduced basis, the Lanczos basis and the eigenbasis of the Kohn-Sham Hamiltonian. We compare to the Taylor propagation scheme, which is known to give very accurate results. We find that the Lanczos and spectral schemes can yield computational speed ups of a factor of 3 relative to Taylor propagation, with only a small loss in accuracy.

3.2 Time Propagator Formalism

In this chapter we discuss time propagation algorithms for the solution of the time-dependent Kohn-Sham equations of the TDDFT,

$$i\hbar\frac{\partial\psi_k(\mathbf{r},t)}{\partial t} = H_{\mathrm{KS}}\psi_k(\mathbf{r},t). \tag{3.1}$$

One's goal is to obtain $\psi_k(\mathbf{r},t)$ for all times t.

Let us define an operator, $U(t_1,t_2)$, known as the propagator, such that

$$\psi_k(\mathbf{r},t_2) = U(t_1,t_2)\psi_k(\mathbf{r},t_1). \tag{3.2}$$

The propagator transforms a Kohn-Sham orbital from time t_1 into time t_2. Eq. (3.1) may be

formally solved to obtain the propagator,

$$\psi_k(\mathbf{r},t_2) = U(t_1,t_2)\psi_k(\mathbf{r},t_1) = \mathscr{T}\exp\left[-\frac{i}{\hbar}\int_{t_1}^{t_2} H_{\mathrm{KS}}(t')dt'\right]\psi_k(\mathbf{r},t_1), \tag{3.3}$$

where $\mathscr{T}$ denotes time ordering. The time ordering operator is necessary since the Hamiltonians at different times, say $H_{\mathrm{KS}}(t)$ and $H_{\mathrm{KS}}(t')$, typically do not commute. That is, $H_{\mathrm{KS}}(t)H_{\mathrm{KS}}(t') \neq H_{\mathrm{KS}}(t')H_{\mathrm{KS}}(t)$. A formal proof of Eq. (3.3) may be found in Fetter and Walecka [97].

In practice, one wishes to obtain the Kohn-Sham orbitals not only at the beginning and the end of the simulation but also at all possible times in between. It is therefore convenient to use the property $U(t_3,t_1) = U(t_3,t_2)U(t_2,t_1)$ to split $U(t,0)$ into a product of multiple time-evolution operators, each corresponding to a short time step δt,

$$U(0,t) = \prod_q U(t_q, t_q+\delta t), \quad t_q = q\delta t. \tag{3.4}$$

There is an additional benefit to the partitioning of the propagator into products which is that for any time, t, and sufficiently small time step, δt, $H_{\mathrm{KS}}(t)$ and $H_{\mathrm{KS}}(t+\delta t)$ must approximately commute. We therefore drop the time ordering operator and the time integration in Eq. (3.3) and obtain,

$$U(t_q, t_q+\delta t) = \exp\left[-\frac{i}{\hbar}H_{\mathrm{KS}}(t_q)\delta t\right]. \tag{3.5}$$

For the remainder of the chapter we shall focus on the construction of approximations to $U(t_q, t_q+\delta t)$.

The first question which must be answered is how to adequately select the time step, δt. The time-energy uncertainly relation, $\delta E\,\delta t \leq \hbar$, gives an absolute upper bound: $\delta t \leq \frac{\hbar}{\delta E_{\max}}$. Put simply, the more rapidly the total energy of the electronic system changes the smaller the time step required to resolve it. The size of δt is therefore dependent on the

physics of the specific system and external potential we wish to consider. Below this physical limitation, the choice of propagator approximation scheme will further limit the choice of δt. In selecting a propagation scheme we should, as Castro et al. [98] notes, minimize the computational cost of propagation per unit time. The remainder of this chapter will detail three propagation schemes and analyze their computational cost and accuracy.

3.3 Taylor, Lanczos, and Spectral Propagator Approximation Schemes

3.3.1 Taylor Expansion of the Propagator

One of the most robust methods for approximating the time propagator is the polynomial expansion using a Taylor series. While we do not consider other polynomial schemes in this thesis, the choice to use a Taylor expansion is not unique. Another example would be the Chebychev polynomial expansion [98, 99]. The advantage of the Taylor scheme is that it only requires the repeated action of the Hamiltonian on the Kohn-Sham orbitals. Taylor propagation has been successfully applied to many systems[72, 100–104], and we shall use it as a benchmark by which the accuracy of other schemes are compared. In this section we motivate and derive the Taylor propagation scheme, and give a discussion of its limitations.

Recall that our goal is to approximate the exponential given in Eq. (3.5). If $H_{\mathrm{KS}}(t_q)$ were a c-number (classical number), one would naturally turn to the usual Taylor expansion,

$$\exp\left[-\frac{i}{\hbar}H_{\mathrm{KS}}(t_q)\right] = \sum_{n=0}^{\infty}\frac{1}{n!}\left(-\frac{i\delta t}{\hbar}H_{\mathrm{KS}}(t_q)\right), \tag{3.6}$$

and simply truncate the series at order N_{taylor} to achieve whatever accuracy is desired. However $H_{\mathrm{KS}}(t_q)$ is a matrix, not a c-number, and the Taylor expansion is not necessarily unconditionally stable. The nature of the stability depends on the order of truncation [98].

For the remainder of this chapter and in the calculations for all subsequent chapters, we

consider the fourth-order Taylor expansion,

$$\psi_k(\mathbf{r}, t_q + \delta t) \approx \sum_{n=0}^{4} \frac{1}{n!} \left(-\frac{i\delta t}{\hbar} H_{\mathrm{KS}}(\mathbf{r}, t_q) \right)^n \psi_k(\mathbf{r}, t_q). \tag{3.7}$$

The critical computational operation in this algorithm is the application of H_{KS} to the an orbital ψ_k. The number of critical operations per time step of the fourth order Taylor propagation is,

$$\frac{N_{\mathrm{critical}}}{\delta t} = 4 \cdot N_{orbitals}, \tag{3.8}$$

where $N_{orbitals}$ is the number of Kohn-Sham orbitals. The fourth-order Taylor-propagation, though not unconditionally stable, gives a very stable propagation provided that the time step is chosen to be suitably small. In practice, we have found that the convergence of the Taylor expansion requires $\delta t \leq 0.001$ fs. This limitation holds regardless of the physical system. For systems with $\frac{\hbar}{\delta E_{\max}} >> 0.001$ fs one wishes to circumvent the restrictions imposed by the Taylor-propagation.

3.3.2 Projection of the Propagator into the Lanczos Basis

In the previous section we considered the polynomial expansion of the time propagator using a Taylor series. By definition, the polynomial terms involved are H_{KS}, H_{KS}^2,..., H_{KS}^n. Can a method be found to use powers of the Hamiltonian to construct the propagator without the convergence concerns typical of polynomial expansions? Consider the so called Krylov subspace of order m,

$$K_k^m(|\psi_k\rangle, \hat{H}_{\mathrm{KS}}) = span\{|\psi_k\rangle, \hat{H}_{\mathrm{KS}}|\psi_k\rangle, \hat{H}_{\mathrm{KS}}^2|\psi_k\rangle, \cdots, \hat{H}_{\mathrm{KS}}^{m-1}|\psi_k\rangle\}. \tag{3.9}$$

In our definition each Kohn-Sham orbital, $|\psi_k\rangle$, has its own Krylov basis which must be calculated separately.

The basis vectors used to span the Krylov subspace in Eq. (3.9) are inconvenient since

they are, in general, neither orthogonal nor normalized. We therefore use the Gram-Schmidt procedure to construct an orthonormal set of vectors which span the Krylov subspace,

$$
\begin{aligned}
|q_{k1}\rangle &= \frac{1}{\beta_{k1}}|\psi_k\rangle \\
|q_{k2}\rangle &= \frac{1}{\beta_{k2}}\left[\hat{H}_{\mathrm{KS}}|\psi_k\rangle - \langle q_{1k}|H_{\mathrm{KS}}|\psi_k\rangle|q_{k1}\rangle\right] \\
|q_{k3}\rangle &= \frac{1}{\beta_{k3}}\left[\hat{H}^2|\psi_k\rangle - \langle q_{k1}|\hat{H}^2_{\mathrm{KS}}|\psi_k\rangle|q_{k1}\rangle - \langle q_{k2}|\hat{H}^2|\psi_k\rangle|q_{k2}\rangle\right] \\
&\cdots
\end{aligned}
\tag{3.10}
$$

The set of basis vectors, q_{ki}, are known as the Lanczos basis. Following the Lanczos algorithm [105], we shall first tridiagonalize the Hamiltonian in the Lanczos basis. Then we diagonalize the tridiagonal Hamiltonian to obtain the m eigenvalues, E_{kj}, and m eigenvectors, $|a_{kj}\rangle$. With E_{kj}, $|a_{kj}\rangle$, and $|q_{ki}\rangle$ in hand we may construct an approximate form for the propagator. First observe that since $H_{\mathrm{KS}}|a_{kj}\rangle = E_{kj}|a_{kj}\rangle$, it may be proven that

$$
\hat{U}(t_q, t_q+\delta t)|a_{kj}\rangle = \exp\left[-\frac{i}{\hbar}\hat{H}_{\mathrm{KS}}(t_q)\delta t\right]|a_{kj}\rangle \tag{3.11}
$$

$$
= \exp\left[\frac{-i\delta t E_{kj}}{\hbar}\right]|a_{kj}\rangle. \tag{3.12}
$$

We now construct the propagator as,

$$
\begin{aligned}
\hat{U}(t_q, t_q+\delta t) &= \sum_{i,j,n,l} |q_{ki}\rangle\langle q_{ki}|a_{kj}\rangle\langle a_{kj}|\hat{U}(t_q, t_q+\delta t)|a_{kn}\rangle\langle a_{kn}|q_{kl}\rangle\langle q_{kl}| \\
&= \sum_{i,j,n,l} |q_{ki}\rangle\langle q_{ki}|a_{kj}\rangle\langle a_{kj}|a_{kn}\rangle \exp\left[\frac{-i\delta t E_{kn}}{\hbar}\right]\langle a_{kn}|q_{kl}\rangle\langle q_{kl}| \\
&= \sum_{i,j,n,l} |q_{ki}\rangle\langle q_{ki}|a_{kj}\rangle\delta_{jn} \exp\left[\frac{-i\delta t E_{kn}}{\hbar}\right]\langle a_{kn}|q_{kl}\rangle\langle q_{kl}| \\
&= \sum_{i,j,l} |q_{ki}\rangle\langle q_{ki}|a_{kj}\rangle \exp\left[\frac{-i\delta t E_{kj}}{\hbar}\right]\langle a_{kj}|q_{kl}\rangle\langle q_{kl}|
\end{aligned}
\tag{3.13}
$$

This approximate form for the operator will only give accurate results when applied to $|\psi_k\rangle$. In our scheme we construct a separate approximation to the propagator for each of the N_{orbitals} Kohn-Sham orbitals. Just as for the Taylor propagation, in this algorithm the most expensive operation is the application of $\hat{H}_{\text{KS}}$ to $|\psi_k\rangle$, which is necessary in this case to construct the Krylov basis in Eq. (3.9). If there are m Lanczos basis vectors then the number of critical steps per time step is $m \cdot N_{\text{orbitals}}$.

In practice, greater than 4 Lanczos vectors are required for accurate propagation and the computational scaling of the algorithm as described thus far is poor compared to Taylor. To improve the computational scaling we make use of two observations: (1) The application of the propagator to the Kohn-Sham orbitals on the Lanczos basis is inexpensive, and (2) the accuracy provided by the approximate form for the propagator remains robust even after multiple time steps. The first claim holds since the Lanczos basis is quite small compared to, for instance, a real-space grid and hence the matrix multiplication required is inexpensive. The veracity of the second claim will be shown in the results section later in this chapter. These two observations suggest that one should update the propagator only once every N_{update} time steps while applying the propagator to the Kohn-Sham orbitals on every time step. The cost per time step of this algorithm then becomes,

$$\frac{N_{\text{critical}}}{\delta t} = \frac{m \cdot N_{\text{orbitals}}}{N_{\text{update}}}. \tag{3.14}$$

3.3.3 Projection of the Propagator into the Spectral Basis

In the previous subsection we considered propagation on a Krylov subspace. In this subsection we construct the propagator on a spectral subspace consisting of eigenvalues and eigenvectors of the Hamiltonian, $H_{\text{KS}}(t_q)$. As for propagation on the Lanczos basis, the majority of the cost will be in the construction of the basis. In this case the construction of the spectral basis will involve the diagonalization of the Hamiltonian. We use the conjugate gradient algorithm to diagonalize the Hamiltonian and obtain N_{spectral} eigenvalues, E_j, and

eigenvectors, $|p_j\rangle$. From these the components of the Hamiltonian on the spectral basis may be constructed as,

$$H^{ij}_{\text{spectral}}(t_q) = \langle p_j | H_{\text{KS}}(t_q) | p_i \rangle \tag{3.15}$$

From this spectral basis Hamiltonian we construct the Crank-Nicholson [106] approximation to the propagator on the spectral basis,

$$\hat{U}(t_q, t_q + \delta t) = (\hat{O} + \frac{i\delta t}{2\hbar}\hat{H}_{\text{spectral}})^{-1} \cdot (\hat{O} - \frac{i\delta t}{2\hbar}\hat{H}_{\text{spectral}}). \tag{3.16}$$

Just as for the Lanczos basis in the previous section, we update the basis only every N_{update} time steps. In order to improve accuracy we update the Hamiltonian each time step. The Hamiltonian may be separated as a sum of a static matrix, $\hat{H}^0_{\text{spectral}}$, and a time-dependent matrix, $\hat{H}^t_{\text{spectral}}$. That is, $\hat{H}_{\text{spectral}} = \hat{H}^0_{\text{Spectral}} + \hat{H}^t_{\text{spectral}}$. The time-dependent piece is given as,

$$\hat{H}^t_{\text{spectral}} = V_{\text{xc}} + V_{\text{Hartree}}. \tag{3.17}$$

The time-dependent part of the Hamiltonian is very easy to compute and therefore updating the Hamiltonian each time step is very inexpensive in comparison to the update of the basis. We prepare the initial basis at the start of the calculation with 160 conjugate-gradient iterations. Subsequent updates to the basis are performed with $16 \cdot N_{\text{spectral}}$ conjugate-gradient iterations. The initial upstart costs of the calculation are negligible for long computational times. The initial preparation may also be combined into the cost of preparing the initial ground state using DFT, which we do not consider here. We will therefore only consider the cost of updating the basis in our algorithm analysis. In our implementation, updating the basis with conjugate-gradient requires $22 \cdot N_{\text{spectral}}$ $H|\phi\rangle$ matrix multiplications, and $20 \cdot N_{\text{spectral}}$ orthogonalizations of the basis for a total of $42 \cdot N_{\text{spectral}}$ critical computational

operations. The number of critical operations per time step is,

$$\frac{N_{\text{critical}}}{\delta t} = \frac{42 \cdot N_{\text{spectral}}}{N_{\text{update}}}. \tag{3.18}$$

3.4 Computational Details and Results

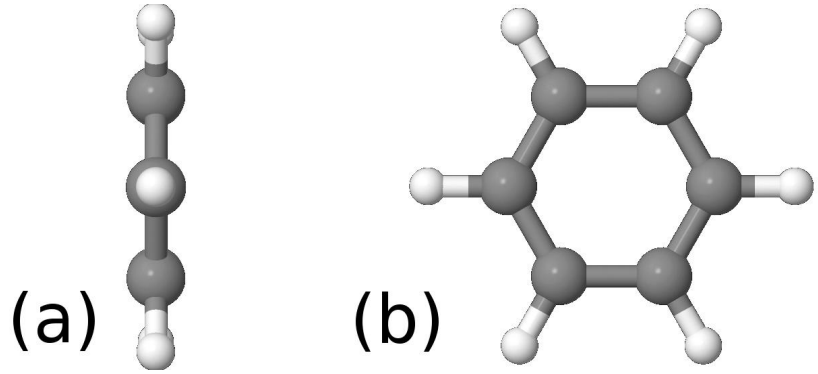

Figure 3.1: Geometry of the benzene molecule. In the simulations, the benzene molecule is aligned with the plane of the molecular perpendicular to the x axis. The geometry is shown for slices of the simulation box in the the (a) x-y plane and (b) y-z plane.

We compare the three time-propagation approximation schemes outlined in the previous section using two physical systems with complex electron dynamics or coupled electron-ion dynamics. In the first subsection, we consider the optical absorption of the benzene molecule. In the next subsection we consider a 200 eV proton which is fired through the center ring of the benzene molecule, extending our benchmarks to the Ehrenfest dynamics.

3.4.1 Optical Absorption of Benzene

The real–space grid has dimensions $L_x = L_y = L_z = 9.8$ Å and a grid spacing of $dx = dy = dz = 0.2$ Å. This is represented by 50 grid points in each direction, for a total of $50 \times 50 \times 50 = 125000$ grid points. We propagate the system for 10 fs. Benzene has

30 valence electrons, which are represented by 15 Kohn-Sham orbitals. The plane of the molecule lies along the y-z plane. These parameters are not fit for comparison of the optical absorption spectrum to experiment. We only seek agreement relative to the benchmark Taylor propagation scheme, which is sufficient to prove the viability of the Lanczos and spectral propagation schemes.

At the start of the simulation a first order linear perturbation is induced by applying a phase factor to the ground state Kohn-Sham orbitals,

$$\phi_k'(\mathbf{r},0) = \exp(i \cdot f \cdot \frac{r_i}{\delta r_i})\phi_k(\mathbf{r},0), \tag{3.19}$$

where f is the strength of the perturbation. We set $f = 0.01$. r_i is the spatial direction along which the perturbation is applied, with $r_1 = x$, $r_2 = y$, or $r_3 = z$. The simulation is repeated three times, once for each choice of the spatial direction, r_i. δr_i is the grid spacing along the r_i direction, which has been set to 0.2 Å for all three spatial directions. $\phi_k'(\mathbf{r},0)$ is then propagated in real time using one of the three schemes outlined in the previous section, yielding the time-dependent Kohn-Sham orbitals, $\phi_k(\mathbf{r},t)$. After calculating the time-dependent Kohn-Sham orbitals for a perturbation along the r_i direction, we then calculate the dipole moment along the same direction,

$$d_{r_i}(t) = \int r_i \cdot \rho(\mathbf{r},t) d\mathbf{r}, \tag{3.20}$$

where $\rho(\mathbf{r},t)$ is the time-dependent electron density calculated from Kohn-Sham orbitals.

Fourier transforming the dipole moment yields the optical absorption spectrum along the r_i direction, S_{r_i}. The optical absorption spectrum, S, of the molecule is calculated by averaging the three spatial directions,

$$S = \frac{1}{3}(S_x + S_y + S_z). \tag{3.21}$$

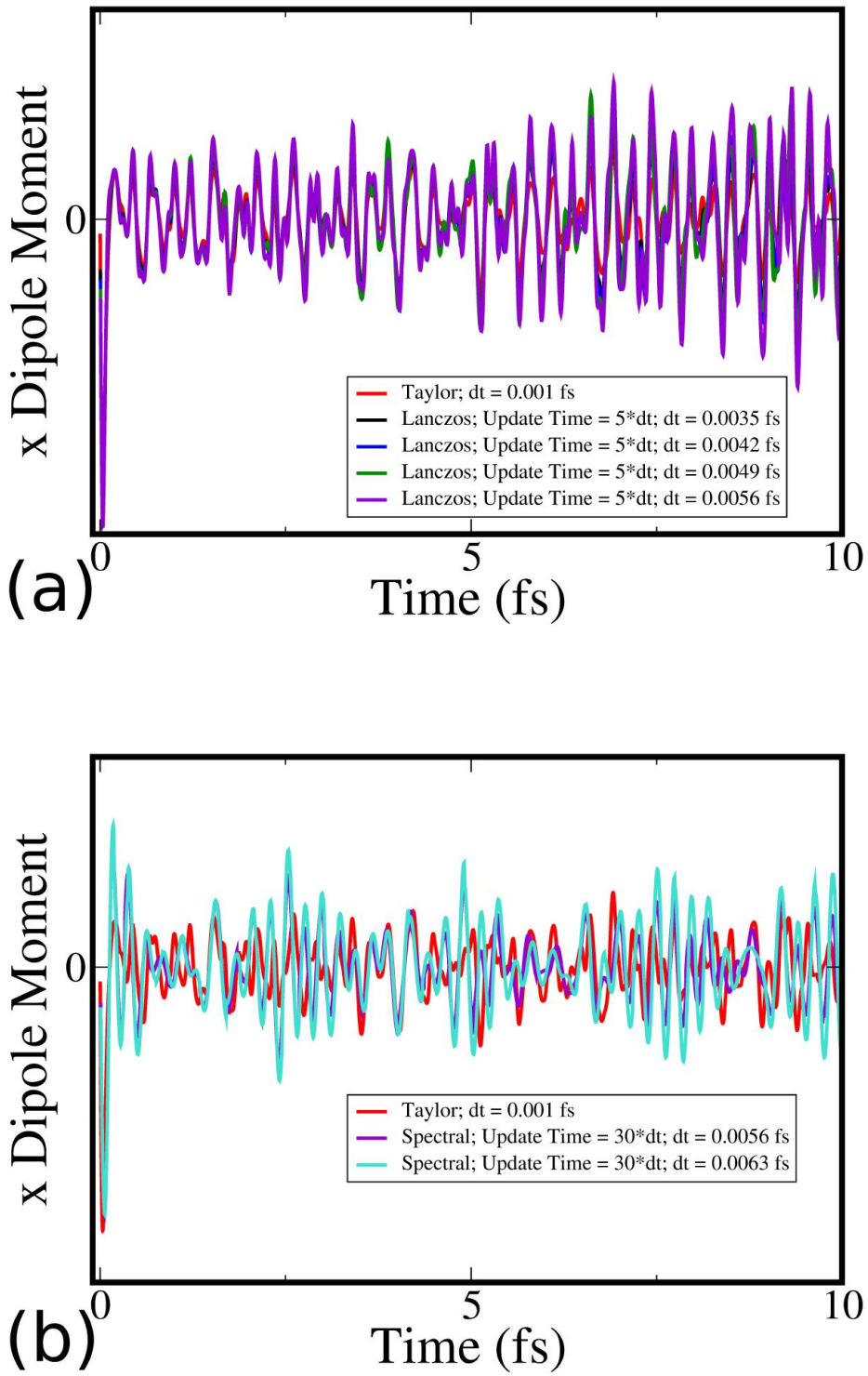

Figure 3.2: Dipole moment, along the x direction which is perpendicular to the plane of the molecule, after a first order perturbation has been applied also along the x direction. The dipole moment is obtained through time-propagation of the Kohn-Sham orbitals using the (a) Lanczos and (b) spectral propagation schemes.

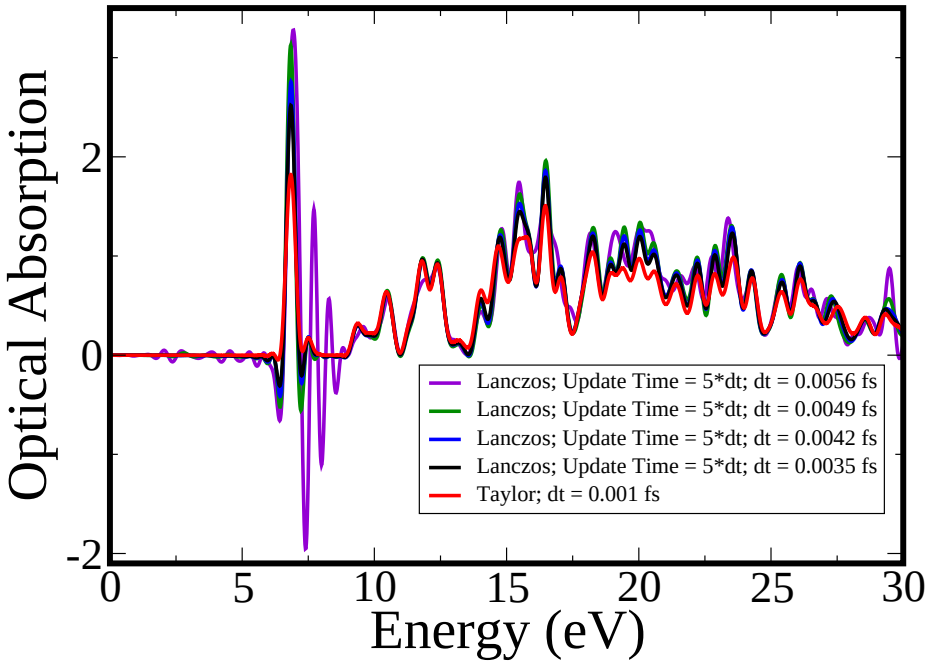

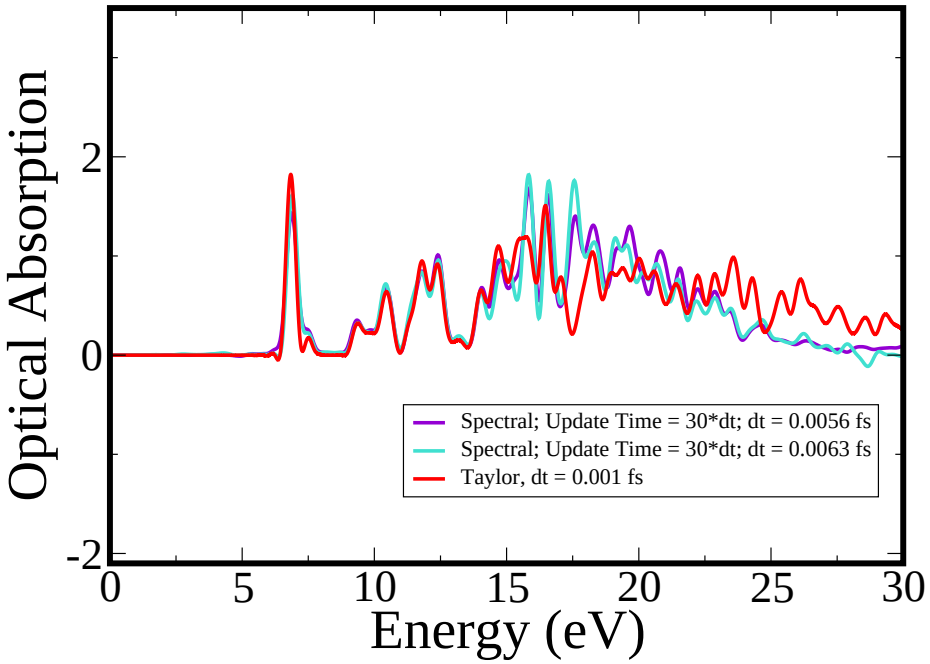

Figure 3.3: Optical absorption spectrum of benzene. The spectrum shown is the average of the optical absorption spectra obtained by Fourier transforming the time-dependent dipole moment in each spatial dimension as generated by a first order perturbation in that direction. The spectrum is obtained through time-propagation of the Kohn-Sham orbitals using the (a) Lanczos and (b) spectral propagation schemes.

In Fig. 3.2 we plot the dipole moment of benzene along the x axis for the Lanczos and spectral propagation schemes. In both plots the result of the Taylor benchmark is shown for comparison. In Fig. 3.3 we plot the total optical absorption of Eq. (3.21).

For the Lanczos scheme, we have found that a reasonable trade off between physical accuracy and computational efficiency by updating the Lanczos basis once every 5 time steps. The number of Lanczos basis vectors is 30. In Figs. 3.2.a and 3.3.a, we have shown four time steps, 0.0035, 0.0042, 0.0049 and 0.0056 fs. We also show the benchmark Taylor propagation with a time step of 0.001 fs. The frequency of the oscillations in the dipole moment tend to follow the Taylor benchmarks for all four time steps. However, the amplitude diverges sharply as the time step increases. The physical quantity which is accessible by experiment is the optical absorption. Up to a time step of 0.0049 fs, the optical absorption is well produced by the Lanczos scheme. Using equations (3.8), (3.14), and (3.18) we have calculated the theoretical computational cost of the various schemes for various time steps and presented them in Table 3.1. The time step of 0.0049 fs gives a theoretical speedup of 3.27 relative to the Taylor propagation benchmark.

We now consider the spectral basis. We have found the calculation of the optical absorption spectrum required that the basis be updated very infrequently compared to the Lanczos basis. We have therefore updated the spectral basis every 30 time steps. The number of basis vectors is 75. In Figs. 3.2.b and 3.3.b we have shown the dipole moment and optical absorption spectrum for time steps of 0.0056 and 0.0063 fs. The optical absorption spectrum is well reproduced for energies below ≈ 15 eV. Accuracy for higher energies may be found by increasing the size of the basis. A time step of 0.0063 fs gives a speedup over the Taylor benchmark of 3.04.

3.4.2 200 eV Proton Collisions with Benzene

We now consider a 200 eV proton fired through the center of a benzene ring. This case allows the testing of the accuracy these propagation schemes when the TDDFT is

Propagator	Basis Update Freq.	Time Step (fs)	Num. Steps	Critical Operations	Speedup
Taylor	X	0.001	10000	40000	1
Lanczos	5	0.0035	2856	17136	2.33
Lanczos	5	0.0042	2380	14280	2.80
Lanczos	5	0.0049	2041	12246	3.27
Lanczos	5	0.0056	1786	10716	3.73
spectral	30	0.0056	2041	14557	2.75
spectral	30	0.0063	1786	13171	3.04

Table 3.1: Number of critical operations required to propagate the Kohn-Sham orbitals of benzene (C_6H_6) after a first order perturbation is applied. The propagation time is 10 fs. The Taylor, Lanczos, and spectral propagation schemes for various time steps and basis update frequencies are shown. The basis update frequency is the number of time steps which are propagated before the basis is updated. An X is placed when there is no basis updating, as is the case with the Taylor propagation. The final column shows the ratio of the critical operations to that of the Taylor propagation benchmark.

coupled with the Ehrenfest dynamics. The real-space grid has dimensions $L_x = 20$ Å, and $L_y = L_z = 16.4$ Å, with a grid spacing of $dx = dy = dz = 0.2$ Å. This is represented with $101 \times 83 \times 83$ grid points, for a total of 695789 grid points. We propagate the system for 40 fs. Benzene has 30 valence electrons which are represented by 15 Kohn-Sham orbitals. The plane of the molecule lies along the y-z plane. The projectile proton begins at a distance 11 Å from the benzene molecule, and is shot through the center ring of the molecule.

The proton is represented as a Coulomb potential which is moving with constant velocity. The Coulomb potential is given by,

$$V_{proj}(\mathbf{r},t) = -\frac{q}{\sqrt{|\mathbf{r}-\mathbf{R}_{\text{proton}}(t)|^2+\varepsilon^2}}, \tag{3.22}$$

where $\mathbf{R}_{\text{proton}}(t)$ is the position of the proton, q is the charge of the proton, and $\varepsilon = 0.01$ Å is a softening parameter used to avoid the numerical instabilities which would be caused by situations where $|\mathbf{r}-\mathbf{R}_{\text{proton}}(t)|$ is very small. The kinetic energy of the proton is 200 eV.

We use the Ehrenfest dynamics to represent the dynamics of the benzene molecule's ions. In the Ehrenfest dynamics, the forces on the ions are given by derivatives of the total electronic energy of the electrons with respect to the ion positions. We compare the

ion positions obtained by solving the TDDFT equations using the Taylor, Lanczos, and spectral propagation schemes.

The proton collision induces an oscillation in the benzene ions. In Fig. 3.4 the position along the z axis of a hydrogen ion and a carbon ion are shown for the Lanczos propagation scheme. The time steps are 0.003, 0.004, and 0.005 fs. The Lanczos basis is once again updated every 5 time steps, and the number of Lanczos basis vectors is again 30. Over the course of 40 fs, the Taylor propagation gives that the ions move away from and eventually return to their equilibrium position. The motion of the ions given by the Lanczos propagation follows the Taylor benchmark fairly closely until ≈ 25 fs for each of the time steps considered. With each time step error accrues in the electron density given by the approximate Lanczos propagator. Eventually the error becomes sufficiently large that the Ehrenfest dynamics diverge from that given by the Taylor propagation. The motion of the ions not shown have similar features. A time step of 0.005 fs gives a speed up factor of 3.33 over the Taylor benchmark (Table 3.2).

Fig. 3.5 shows the position along the z axis of the hydrogen ion and the carbon ion for the spectral propagation scheme. The time steps are 0.005 and 0.006 fs. The spectral basis is updated every 20 time steps. The number of basis vectors is again 75. Just as for the Lanczos propagator, the motion of the ions given by the spectral propagation follows the Taylor benchmark fairly closely until ≈ 25 fs for each of the time steps considered. A time step of 0.006 fs gives a speed up factor of 2.22 over the Taylor benchmark (see Table 3.2).

3.5 Conclusion

We have compared two propagation schemes, Lanczos and spectral, to the Taylor propagation. We have tested these propagators for two physically relevant systems, the optical absorption and the ion collision. It has been found that a computational speed up may be obtained with only small losses in accuracy in certain energy and time regimes.

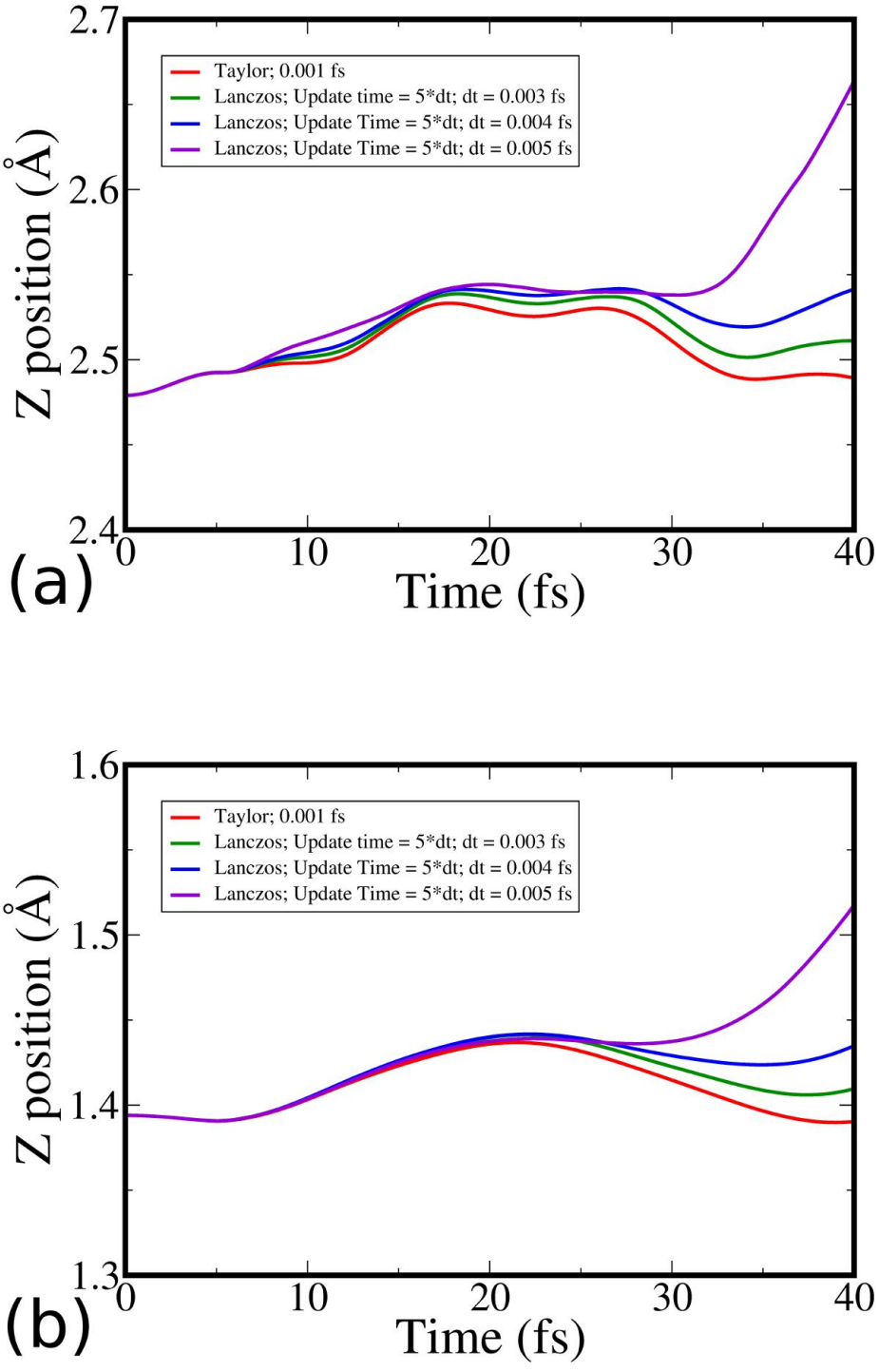

Figure 3.4: Time-dependent positions of a (a) hydrogen and a (b) carbon ion during the collision of a 200 eV proton with a benzene molecule. The calculation is performed by solving the Ehrenfest dynamics equations coupled with TDDFT. Time propagation in the TDDFT accomplished through the Lanczos propagator.

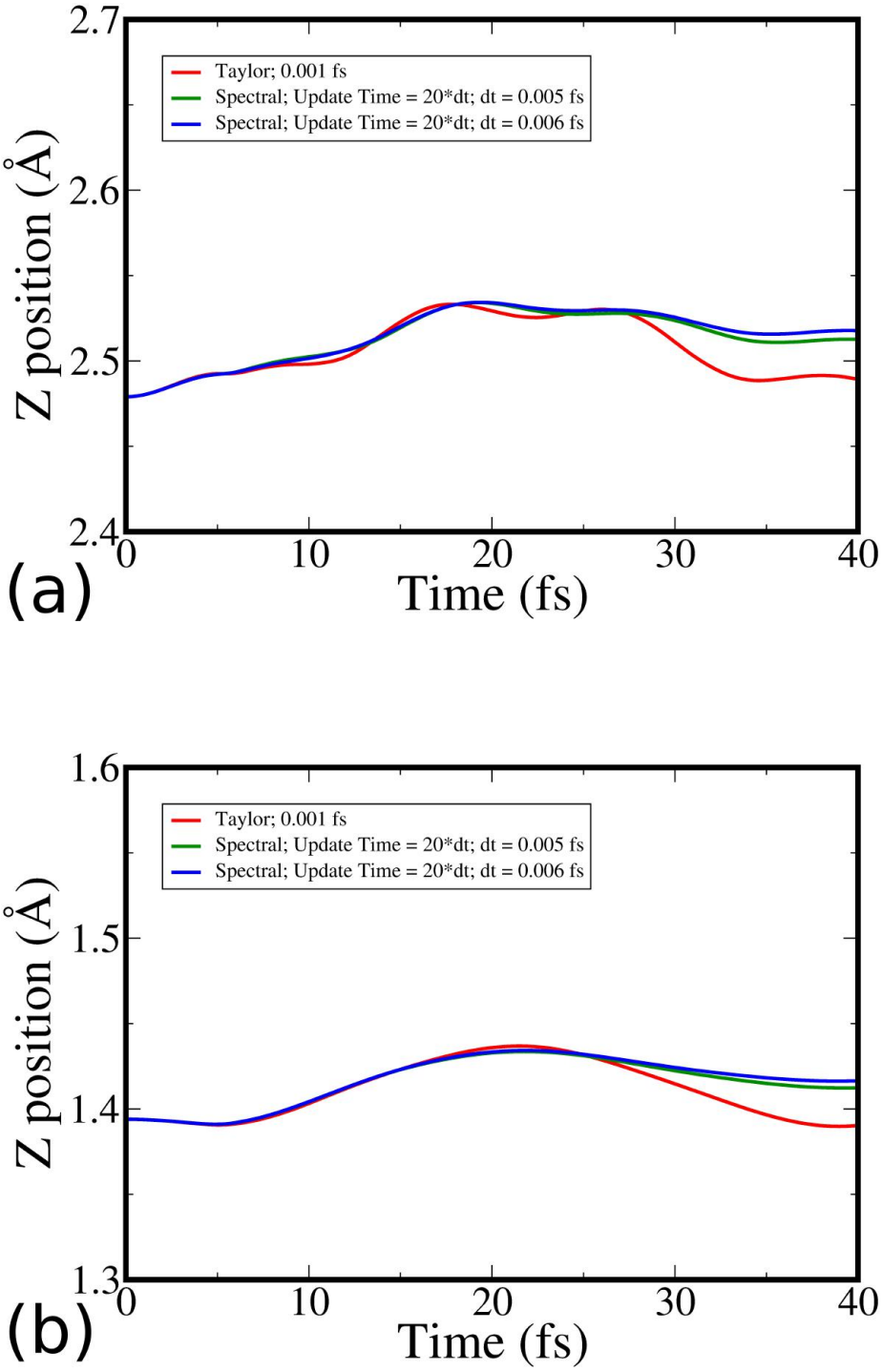

Figure 3.5: Time-dependent positions of a (a) hydrogen and a (b) carbon ion during the collision of a 200 eV proton with a benzene molecule. The calculation is performed by solving Ehrenfest dynamics equations coupled with TDDFT. Time propagation in the TDDFT accomplished through the spectral propagator.

Propagator	Basis Update Freq.	Time Step (fs)	Num. Steps	Critical Operations	Speedup
Taylor	X	0.001	40000	160000	1
Lanczos	5	0.003	13334	80004	2.00
Lanczos	5	0.004	10000	60000	2.67
Lanczos	5	0.005	8000	48000	3.33
spectral	20	0.005	8000	86055	1.86
spectral	20	0.006	6667	72059	2.22

Table 3.2: Number of critical operations required to propagate the Kohn-Sham orbitals of benzene (C_6H_6) during a collision with a 200 eV proton. The propagation time is 40 fs. The results using the Taylor, Lanczos, and spectral propagation schemes for the TDDFT with various time steps and basis update frequencies are shown. The basis update frequency is the number of time steps which are propagated before the basis is updated. An X is placed when there is no basis updating, as is the case with the Taylor propagation. The final column shows the ratio of the critical operations to that of the Taylor propagation benchmark.

Chapter 4

Fragmentation and Ionization of Acetylene and Ethylene Induced by Strong Short Linearly Polarized Laser Fields

4.1 Introduction

The ionization of molecules with intense laser pulses is a complex process due to the interplay of the time varying external potential introduced by the strong laser electric field and the Coulomb interaction between the electrons [4, 107–111]. The final and seemingly close aim is not only understanding but also controlling the ionization dynamics to influence chemical reactions at the femtosecond time scale [44–46, 112]. The interaction of molecules with laser fields obviously depends on the laser parameters such as field strength, frequency, pulse shape and carrier envelope phase. It also depends on the directionality of the molecular frame relative to the laser field's polarization axis, which will hereafter be referred to simply as the alignment. Over the last decade experimental investigation of photoelectron angular distributions from aligned molecules has become possible [30–34]. This allows a clear comparison between experiment and theory without the obscuring effect of averaging over alignments [72]. Experiments also reveal a difference in the ionization from different molecular orbitals reflecting the nodal symmetry of the molecular wave functions [19–28]. Beyond mere structural effects it is also found that the total ionization yield can be increased by a coherent amplification of lower orbitals [21]. Finally, one of the most important mechanisms in molecular ionization is enhanced ionization [113–115], where highly efficient ionization occurs at critical nuclear separations. Recently, experimental evidence has been found that this process may also take place at many bonds in parallel in a polyatomic molecule [116, 117].

In this chapter the TDDFT [82] coupled with the Ehrenfest dynamics [94] will be used to study the alignment dependence of ionization in short laser pulses. Two small molecules,

acetylene and ethylene, exposed to laser pulses of various intensity and durations will be used to analyze how the time-dependent Kohn-Sham orbitals' ionization dynamics couple with the ions' dynamics. We will study (i) the enhanced ionization in a restricted fixed ion model as well as in a fully dynamical simulation (ii) the alignment dependence of the ionization, and (iii) the role of the molecular orbitals and their different symmetries in the ionization and fragmentation dynamics.

From a numerical point of view these are difficult problems because the solution of the time-dependent Schrödinger equation is very complicated beyond simple one- or two-electron systems. Pioneering works aiming to set up a simple framework to understand ionization include the model where the electrons and nuclei are treated classically [115], and the single active electron model [18], originally formulated for atoms, which assumes that the ionization of atoms can be described by an appropriately modified hydrogen-like model. This model was later extended for molecules [17] and has been used to study the ionization of diatomic molecules [118, 119]. Another theoretical approach, the Time-Dependent Hartree Fock (TDHF) [58–60] method, was also used to study the physical mechanisms behind the fragmentation of molecules in intense laser fields. These works have focused on the total and orbital ionization efficiencies and the enhanced ionization mechanism of acetylene (C_2H_2) by exploring the electron dynamics.

Enhanced ionization is described as a three step process [115]. First the C-H bonds expand to a critical separation, R_c. Then, the increased C-H bond length leads to highly efficient ionization of the molecule [116, 117]. After the enhanced ionization, the molecule often undergoes fragmentation ejecting the hydrogen ions. Using the TDHF approach it was shown that as the C-H bond lengths are symmetrically increased, the ionization efficiency of each orbital also increases until the bond lengths reach a critical separation after which the ionization efficiency plateaus, thus demonstrating the enhanced ionization mechanism. The TDHF approach is expected to capture the essence of the laser induced electron dynamics. However, in these simulations the ion positions were fixed for the duration of

the laser pulse.

A dynamically more complete picture of the electron-nuclear dynamics and ionization can be given in the framework of TDDFT. TDDFT has been used to study the Coulomb explosion of deuterium [70, 71], biomolecules immersed in liquid water [120], water clusters [121], and small hydrocarbon molecules [72]. TDDFT simulations have also been used to describe the electron-ion dynamics of H_2S [74] and to simulate the Coulomb imaging of biphenyl [73].

4.2 Computational Method

We shall calculate the ionization of the molecule using Eq. 2.30, defined in chapter II. Strictly speaking, the fractional electron number is related to the probability of ionization. We shall simply refer to the quanity $N(0) - N(t)$ as the ionization of the molecule.

The computational results presented in the next section have been calculated by using the following parameters. The $L_x \times L_y \times L_z$ box size is $L_x =$ 40 Å, $L_y = L_z$= 34 Å, for C_2H_4 and $L_x = L_y = L_z = 34$ Å for C_2H_2. The C-C bond lies in the x direction. The grid spacing is 0.25 Å in each direction. The CAP starts 5 Å from the boundary. The time step for the propagation of the wave function is $\delta t = 0.0007$ fs. The equation of the ionic motion [Eq. (2.40)] is solved with the Verlet algorithm with time step 0.0028 fs. These parameters lead to very well converged results. The calculated ionization potential is 11.0 eV for C_2H_4 and 11.8 eV for C_2H_2 (the experimental values are 10.5 eV for the C_2H_4 and and 11.4 eV for C_2H_2 [122]).

4.3 Results and Analysis

Using the TDDFT [82] and Ehrenfest dynamics [94] as introduced in chapter II, we have studied the ionization mechanism of acetylene and ethylene exposed to laser pulses carried at a wavelength of 800 nm with a various peak intensities and durations. Our choice of the two molecules is on the one hand motivated by previous experimental [116, 117]

	KE (eV)	HOMO	HOMO-1	HOMO-2	HOMO-3	HOMO-4	HOMO-5	Num. Electrons
C_2H_2, parallel								
4×10^{14} W/cm^2, 4.5 fs	0	1.7	1.7	1.9	1.9	2.0	X	9.1
7×10^{14} W/cm^2, 4.5 fs	0	1.5	1.5	1.7	1.7	2.0	X	8.3
14×10^{14} W/cm^2, 4.5 fs	11.7	1.2	1.2	1.1	1.2	1.9	X	6.6
4×10^{14} W/cm^2, 15 fs	0	1.5	1.5	1.8	1.6	2.0	X	8.5
7×10^{14} W/cm^2, 15 fs	14.9	1.3	1.3	0.3	0.5	1.9	X	5.3
14×10^{14} W/cm^2, 15 fs	22.8	1.1	1.1	0.6	0.2	1.6	X	4.6
4×10^{14} W/cm^2, 25 fs	0	1.5	1.5	1.7	1.5	2.0	X	8.1
7×10^{14} W/cm^2, 25 fs	16.5	1.3	1.3	0.7	0.2	1.9	X	5.4
14×10^{14} W/cm^2, 25 fs	22.5	0.9	0.9	0.5	0.1	1.4	X	3.6
C_2H_2, 22.5°								
4×10^{14} W/cm^2, 4.5 fs	0	1.7	1.5	1.9	1.9	2.0	X	9.0
7×10^{14} W/cm^2, 4.5 fs	0	1.6	1.3	1.8	1.8	2.0	X	8.4
14×10^{14} W/cm^2, 4.5 fs	8.5	1.3	1.0	1.4	1.4	1.9	X	7.0
C_2H_2, 45°								
4×10^{14} W/cm^2, 4.5 fs	0	1.8	1.3	2.0	2.0	2.0	X	9.0
7×10^{14} W/cm^2, 4.5 fs	0	1.7	1.0	1.9	1.9	2.0	X	8.4
14×10^{14} W/cm^2, 4.5 fs	4.9	1.5	0.7	1.7	1.5	2.0	X	7.3
C_2H_2, perpendicular								
4×10^{14} W/cm^2, 4.5 fs	0	1.9	1.1	2.0	2.0	2.0	X	9.0
7×10^{14} W/cm^2, 4.5 fs	0	1.8	0.8	1.9	2.0	2.0	X	8.5
14×10^{14} W/cm^2, 4.5 fs	0	1.6	0.4	1.7	1.9	2.0	X	7.6
4×10^{14} W/cm^2, 15 fs	0	1.9	0.7	2.0	2.0	2.0	X	8.6
7×10^{14} W/cm^2, 15 fs	0	1.7	0.3	1.9	2.0	2.0	X	8.0
14×10^{14} W/cm^2, 15 fs	10.0	1.4	0.0	0.9	1.9	2.0	X	6.3
4×10^{14} W/cm^2, 25 fs	0	1.9	0.6	2.0	2.0	2.0	X	8.4
7×10^{14} W/cm^2, 25 fs	0	1.7	0.2	1.9	2.0	2.0	X	7.8
14×10^{14} W/cm^2, 25 fs	13.7	1.4	0.0	0.4	1.9	2.0	X	5.7
C_2H_4, C-C parallel								
8×10^{14} W/cm^2, 9 fs	5.9	1.3	1.0	1.3	1.3	1.6	2.0	8.5
8×10^{14} W/cm^2, 17 fs	18.8	1.2	0.4	0.4	0.3	1.1	1.8	5.1
C_2H_4, C-C perpendicular								
8×10^{14} W/cm^2, 9 fs	0.2	1.6	0.6	1.5	1.6	1.9	2.0	9.2
8×10^{14} W/cm^2, 17 fs	9.6	1.5	0.1	0.6	1.0	1.5	2.0	6.8
C_2H_4, perpendicular								
8×10^{14} W/cm^2, 9 fs	0	0.2	2.0	1.7	2.0	2.0	2.0	9.8
8×10^{14} W/cm^2, 17 fs	0	0.0	2.0	1.7	2.0	2.0	2.0	9.6

Table 4.1: Orbital ionization dynamics of C_2H_2 and C_2H_4 for various laser pulses and molecular alignments. The first column gives the kinetic energy of the hydrogen ions (per ion). The subsequent columns show the occupation number of each Kohn–Sham orbital and the total electron number at the end of the simulation. C_2H_2 has only five occupied orbitals (HOMO, HOMO-1, HOMO-2, HOMO-3, HOMO-4), and hence the column for the occupation of the HOMO-5 has been marked with an X to indicate that it is not applicable in this case.

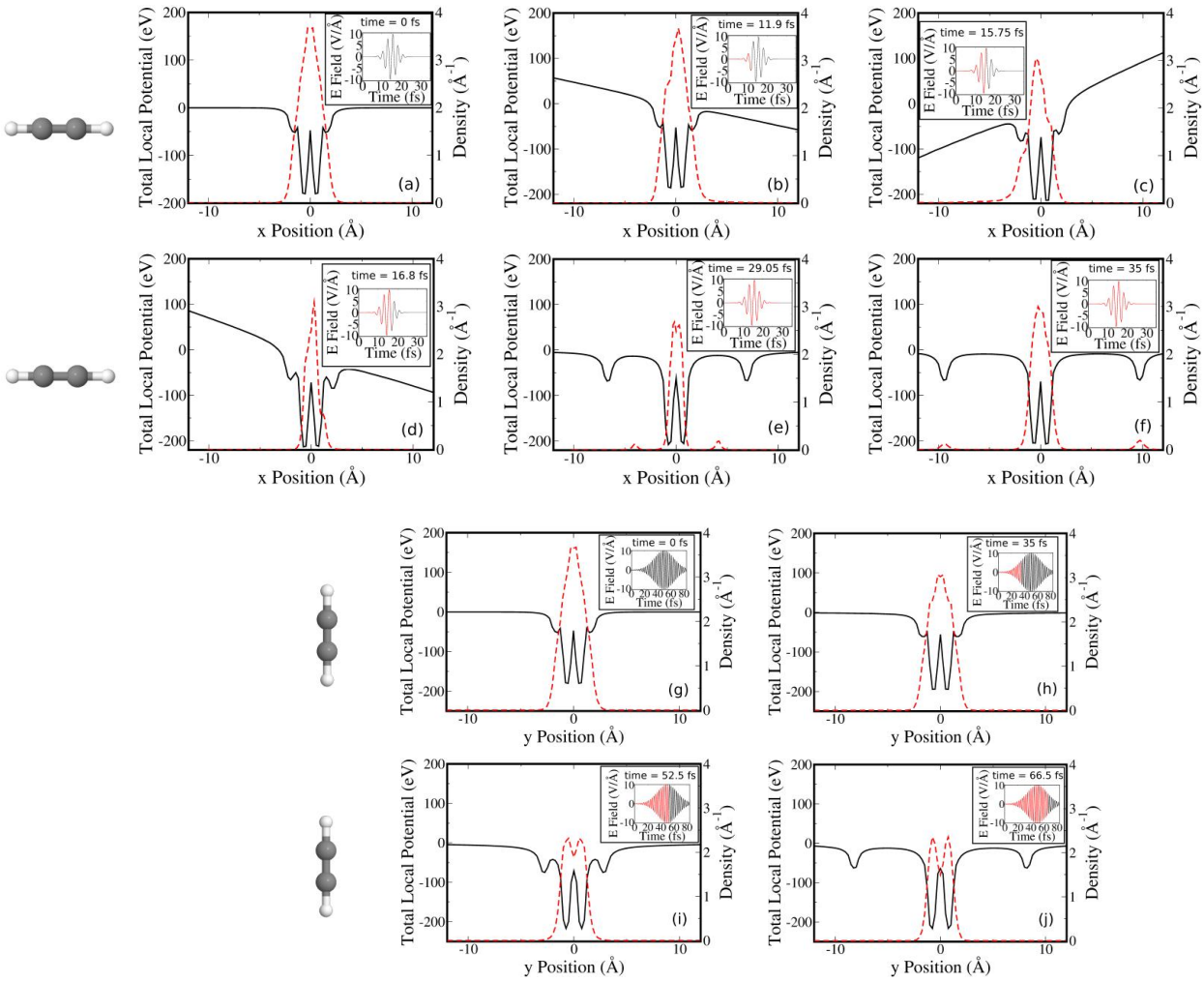

Figure 4.1: (Color online) (a)-(f) Selected snapshots of the total local potential (solid black line) and the density (dashed red line) for C_2H_2 along the alignment axis of the molecule (x axis), integrated out to 2 Å perpendicular to the x axis. The laser peak intensity is 14×10^{14} W/cm^2 and the pulse duration 4.5 fs. The total local potential consists of the Hartree potential, the local part of the exchange correlation potential, the ionic pseudo-potential, and the external potential of the laser field. The insets show the simulation time and the laser pulse highlighted up to the current simulation time. Panel (a) shows the unperturbed initial state. In (b) the density spreads towards one end of the simulation box due to the external potential. In (c) the electric field has switched direction and the density spreads towards the opposite end of the simulation box. In (d), the electric field has switched direction again. In panels (e) and (f) the hydrogen atoms have been split off and are ejected towards the ends of the simulation box. (g)-(j) Selected snapshots of the total local potential (solid black line) and the density (dashed red line) along the alignment axis of C_2H_2 (y), integrated out to 2 Å perpendicular to the y axis. The laser polarization direction is x, the peak intensity is 14×10^{14} W/cm^2 and the pulse duration is 25 fs. Panel (g) shows the unperturbed initial state at. In panel (h) the density has decreased as the laser ionizes the molecule. In panel (i) the density has further decreased and the hydrogen ions have begun to dissociate from the molecule. In panel (j) the hydrogen ions have dissociated and are ejected towards the ends of the simulation box.

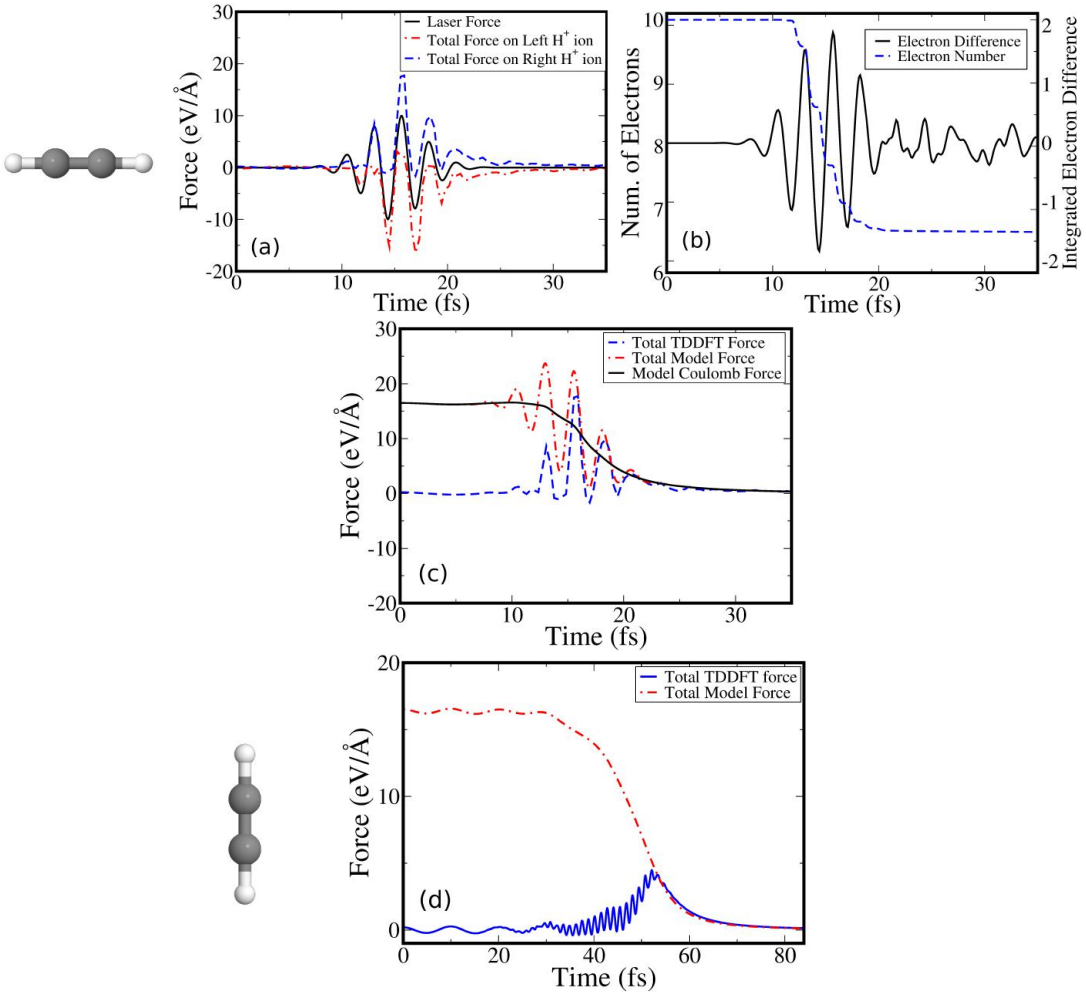

Figure 4.2: (Color online) (a)-(c) Acetylene in a laser field with a polarization direction parallel to the molecular axis, an intensity of 14×10^{14} W/cm^2 and a pulse duration of 4.5 fs. (a) The total force on the two hydrogen ions, which is the sum of the laser force, the ion-ion forces, and the electron-ion force. The laser force (black line) is equal for both hydrogen ions. (b) Fractional electron number, $\int \rho d^3x$, and the difference between the fractional electron number in the left side of the box and the right side of the box, $\int_{x<0} \rho \; d^3x - \int_{x>0} \rho \; d^3x$. (c) The Coulomb force and total force on the right hydrogen ion calculated assuming a simple model where each atom loses one electron instantaneously. The ion-ion distances used in this simple force calculation are taken from the TDDFT simulation. The total force from the TDDFT simulation is shown for comparison. (d) The total force along the y (molecular) axis on a hydrogen ion calculated by TDDFT for a laser field polarized along x (perpendicular alignment) and a pulse peak intensity of 14×10^{14} W/cm^2 and pulse duration of 25 fs. A simple model calculation for the Coulomb force on a hydrogen ion is also shown, with the same details as in plot (c). The ion moves essentially along the y (molecular) axis for the duration of the simulation with only a small oscillation (< 0.02 Å) along the x (polarization) axis.

and theoretical [58–60] studies on these molecules and on the other hand by the different complexity and structure of them. The acetylene molecule is one step from the diatomic molecules towards more complicated structures. It is still a linear molecule, so the relative direction of the laser field and the molecular frame is given by a single angle, but it has two nonequivalent bonds: the strong threefold C-C bond in the middle and the two C-H bonds at the ends. Ethylene is one step further toward the larger hydrocarbon molecules. It has a coplanar geometry with a H-C-H angle close to the ideal 120° for sp^2 hybridized carbon. We will study the ionization from different orbitals, the dependence of ionization on the alignment of the molecule, and the ionization from bond-stretched configurations. The goal of this study is to understand the enhanced ionization mechanism beyond the static TDHF picture and to investigate the role of the molecular alignment in the ionization process.

4.3.1 Acetylene (C_2H_2)

The ionization and molecular dynamics of acetylene, C_2H_2, has been studied by varying the intensity and duration of the laser field for parallel and perpendicular alignments of the molecule relative to the laser polarization direction. We have studied the response to nine different laser fields (see Table 4.1) with intensities and pulse durations typical in experiments [117].

4.3.1.1 Acetylene in a laser field polarized parallel to the molecular axis

Before turning to the detailed results of the TDDFT simulations we show a simple picture that captures the essence of the electron-nuclear dynamics in acetylene aligned parallel to the laser field polarization direction. In this picture we investigate the separate actions of the different potentials, i.e. the Hartree potential [Eq. (2.6)], the local part of the exchange correlation potential, the ionic potential, and the external potential of the laser field. Fig. 4.1 shows snapshots at different times during and after the laser pulse of the total

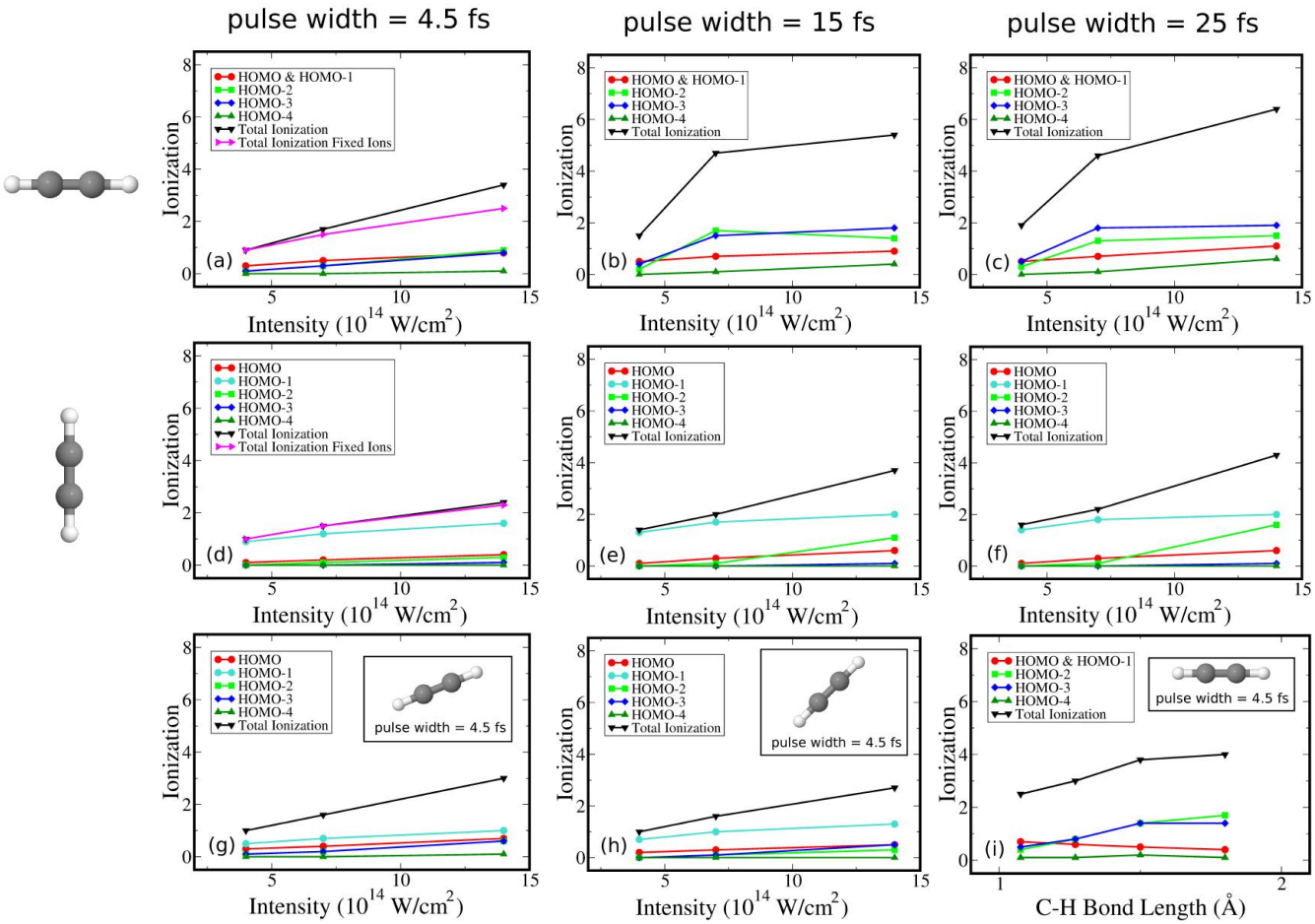

Figure 4.3: (Color online) (a)-(f) Total and orbital ionization as a function of laser intensity for C_2H_2 for a pulse duration of 4.5 fs (a, d), 15 fs (b, e) and 25 fs (c, f) for alignments of the molecule parallel (a)-(c) and perpendicular (d)-(f) to the laser polarization direction. Additionally, in panels (a) and (d) the total ionization for fixed ions is shown. Panels (g) and (h) show the total and orbital ionization as a function of laser intensity for angles of 22.5° and 45° between the molecular axis and laser polarization direction, respectively. The laser pulse duration is 4.5 fs. Panel (i) shows the ionization as a function of C-H bond length for a laser peak intensity of 14×10^{14} W/cm^2 and a pulse duration of 4.5 fs.

potential, i.e. the sum of all the potentials, and the electron density along the x axis , to which both the molecule and laser field polarization are parallel.

The total potential shows two shallow and two deep wells corresponding to the positions of the hydrogen and carbon nuclei. The acetylene molecule is subject to a few-cycle laser pulse with a duration of 4.5 fs and a laser peak of 14×10^{14} W/cm^2. Here and throughout the manuscript the pulse duration is defined as full width at half maximum (FWHM) of intensity. In the second snapshot, Fig. 4.1(b), the potential declines and the tail of the density spreads out to the right. Next, Fig. 4.1(c), the laser field changes direction, the potential inclines and the density tail spreads out more towards the left side. At this time (15.75 fs) the laser has reached its peak amplitude and the hydrogen nuclei are already moving outward, although the distance from the original position is only 0.3 Å. The next snapshot, Fig. 4.1(d), illustrates the situation at the next peak of the laser. In these snapshots one can also compare the laser potential to the potential of the atomic cores and one sees that the ionization is more probable from and around the shallow hydrogen nuclei. The snapshots also show the ionization by the visible decrease of the total density. The number of valence electrons drops from 10 to 6 by the end of the laser pulse, see Fig. 4.3(a). The last two snapshots depict the potential and the density after the laser pulse, showing the motion of the emitted protons.

The motion of the nuclei and the eventual fragmentation is caused by the interplay of the forces arising from the electron localization caused by the laser and the direct force that the laser imposes on the charged nuclei. The latter force is given by the first term on the right-hand side of Eq. (2.40). The resulting forces on the H^+ ions are illustrated in Fig. 4.2(a). Consider the peak of the laser field at 15.75 fs. The laser field's polarization points to the right and it applies a rightward force on the two hydrogen ions. However, the laser also causes the fast moving electrons to move to the left, as shown in Fig. 4.2(b). For the left hydrogen ion, the excess of electrons will induce additional Coulomb shielding between the H^+ and the other ions, which manifests as a leftward force. This force cancels with the

laser force, and the total force is nearly zero. For the right hydrogen atom, the reduction of electrons reduces the Coulomb shielding, which manifests itself as a rightward force. This force will be additive with the laser force. Hence, the total force is much greater than the laser force alone. This picture is reversed when the electric field's polarization is reversed.

We have also compared the force acting on the protons to a model force [115], which is calculated as the sum of the direct laser force and the Coulomb force between a proton and a triply charged C_2H^{3+} fragment. This quantity over time is depicted in Fig. 4.2(c). In the model force calculation the trajectory of the TDDFT simulation is used for the position of the particles and one electron is removed from each atom corresponding to the ionization of roughly four electrons shown in Fig. 4.2(b). As shown in Fig. 4.2(c), the sudden ionization leads to the removal of four electrons right after the peak of the laser field (around 17 fs) and after that time the model and TDDFT force are similar. The Coulomb dissociation starts at around the peak of the laser field and at 17 fs the protons have moved about 2 Å. Hence, the bond is definitely broken and the simple Coulomb model captures the dynamics.

Now we turn to a more detailed analysis of the ionization mechanism using the full TDDFT model and allowing the ions to move according to the Ehrenfest dynamics. Before we begin this discussion we note that due to the Ehrenfest scheme each simulation represents only an averaging over all possible nuclear fragmentation channels. This is due to the fact that the Ehrenfest dynamics give only a single classical trajectory for the ions, whereas a fully quantum description would yield the nuclear wave function from which the probability of each fragmentation channel may be obtained. At low intensity and pulse width the probability of fragmentation is small and the dissociation of the C-H bonds does not occur in our simulations. Coulomb explosion is observed for higher intensities and longer pulses (see Table 4.1).

We first consider the case of 4.5 fs laser pulses with three different peak intensities. The total ionization is plotted in Fig. 4.3. As expected, the number of electrons removed increases with the intensity of the laser. After the ionization exceeds a critical electron

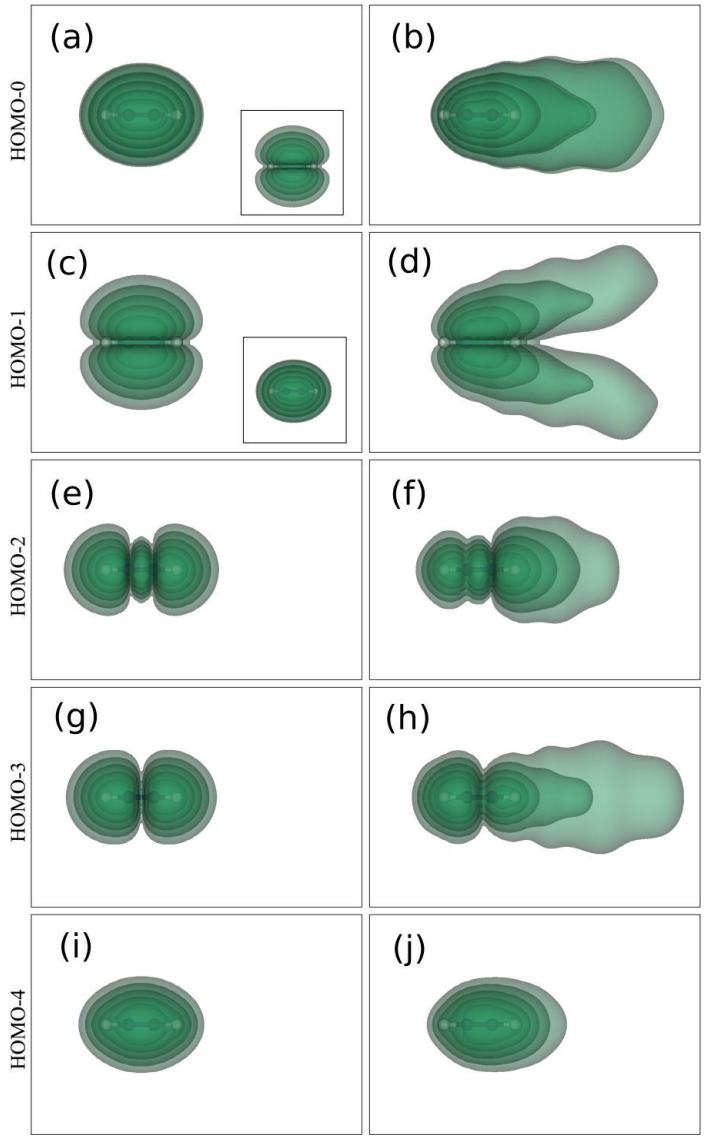

Figure 4.4: (Color online) Time evolution of the Kohn-Sham orbitals in acetylene subjected to a 4.5 fs pulse with a peak intensity of 4×10^{14} W/cm^2 and field polarization parallel to the molecular axis. Here we show the absolute squares of the orbitals at $t = 0$ fs (left column) and at an instant when the laser field magnitude is near its peak at $t = 11.9$ fs (right column). The insets show the HOMO and HOMO-1 rotated by 90° about the molecular axis.

number the molecule undergoes Coulomb explosion.

Fig. 4.4 shows the ground state Kohn–Sham orbitals of acetylene and snapshots of the orbitals at the peak of the laser field. The HOMO and HOMO-1 are energy degenerate and their shapes are exactly 90° rotations of one another. The HOMO-2, HOMO-3, and HOMO-4 are all cylindrically symmetric, but each has its own nodal symmetry. Due to their different symmetries, the orbitals each ionize with a different angular distribution (right column of Fig. 4.4). Despite the orbitals' different nodal symmetries, single particle energies, and angular distributions, the total ionization is very similar for the HOMO, HOMO-1, HOMO-2, and HOMO-3, see Fig. 4.3(a). The HOMO-4 orbital is significantly more deeply bound and the ionization is small. The ionization from the HOMO and the HOMO-1 orbitals is nearly identical due to their energy degeneracy and similar symmetry. At low intensity, the HOMO and HOMO-1 are the most ionized. As the intensity of the laser is increased, the inner orbitals, HOMO-2 and HOMO-3, are increasingly ionized. The most significant change is that in the strongest field the HOMO-2 orbital has the largest ionization. This is partly due to its complicated nodal structure and to the fact that the time–dependent Kohn–Sham binding energy (not shown) of this orbital decreases the most in the laser field.

According to the enhanced ionization model, as the C-H bond length of the molecule increases there is a corresponding increase in the ionization rate. To check this Ref. [60] studied the ionization from bond stretched molecular states using the TDHF approach. This model is an approximation since the laser pulse increases the bond length and ionizes the molecule simultaneously. Hence in the stretched configurations the electron number is decreased and these configurations are positively charged. For simplicity this effect was neglected. While our TDDFT simulations with the Ehrenfest dynamics do not suffer from this drawback, it is unclear how important the enhanced ionization effect is to the total ionization. We have therefore repeated the TDDFT calculations without Ehrenfest dynamics, i.e. with ions held fixed in the ground state geometry or in bond stretched geometries.

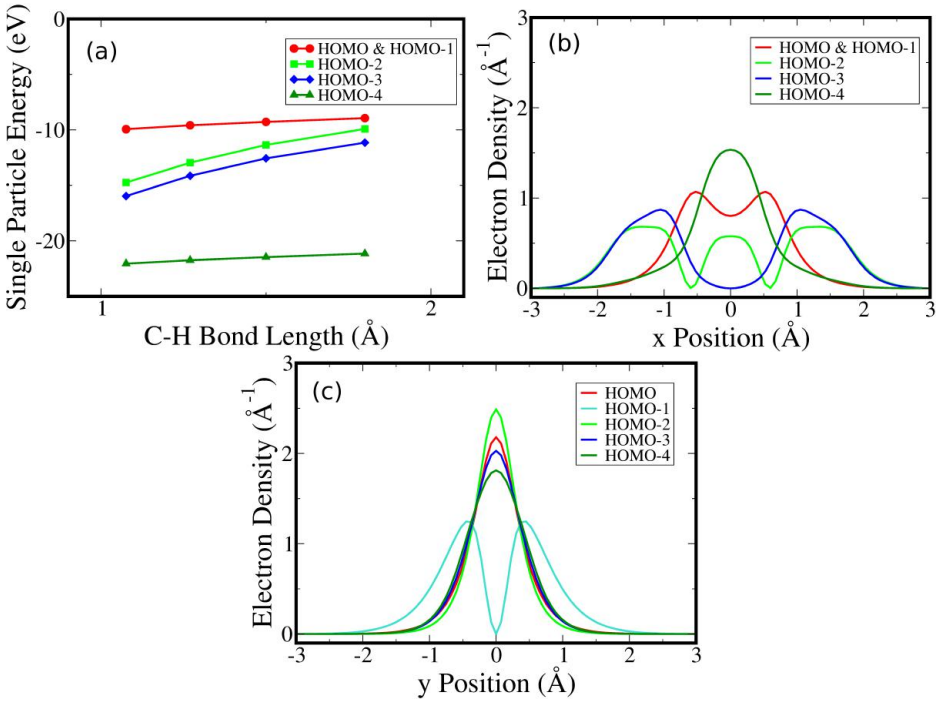

Figure 4.5: (Color online) Panel (a) shows the ground state Kohn–Sham single particle energies as a function of C-H bond length. Panel (b) shows the average density of the ground state Kohn–Sham orbitals along the alignment axis of the molecule (x axis). Panel (c) shows the average density of the ground state Kohn–Sham orbitals along an axis perpendicular to the alignment axis of the molecule (y axis). Panels (b) and (c) refer to C_2H_2 in its equilibrium geometry.

Fig. 4.3(a) shows that for low fields the ionization from moving or fixed nuclei are nearly the same. This is not surprising as the ions barely move in the low fields. At 14×10^{14} W/cm^2, the two C-H bond lengths increase (asymmetrically) from 1.076 Å to 3.744 Å and to 3.909 Å by the time the ionization completes. The bond stretching causes an additional ionization of 0.9 electrons relative to the fixed ions case. This additional ionization comes primarily from the increased ionization of the inner orbitals, HOMO-2 and HOMO-3. When the ion positions are fixed in the ground state geometry ($R_{C-H} = 1.076$ Å), the ionization of the inner orbitals is suppressed, see Fig. 4.3(i).

To further investigate the effect of bond stretching on the ionization, we have repeated the fixed ion calculations for several extended geometries. Fig. 4.3(i) shows that the total ionization increases with the C-H bond lengths in qualitative agreement with Lötstedt et al. [60]. If the ions are fixed in the ground state geometry, the HOMO and HOMO-1 are ionized the most. As the C-H bond length is increased, the HOMO-2 and HOMO-3 become more ionized. At a C-H bond length of $R = 1.8$ Å the ionization is dominated by the inner orbitals, HOMO-2 and HOMO-3. At the same time the ionization of the HOMO and HOMO-1 is slightly suppressed. The increased ionization of the HOMO-2 and HOMO-3 is partially because they are less tightly bound in the stretched configurations, see Fig. 4.5(a). The fixed ion model qualitatively matches the orbital dynamics seen with the Ehrenfest dynamics, Fig. 4.3(a), where the ionization of the HOMO-2 and HOMO-3 overtakes the HOMO and HOMO-1 at intensities high enough to cause bond stretching. Hence, the enhanced ionization mechanism works primarily by ionizing the inner orbitals.

Finally, we have run calculations with longer pulses to see if Coulomb explosion appears within the Ehrenfest scheme at lower intensities. Table 4.1 shows the summary of results for 15 fs and 25 fs pulses over three intensities. The longer pulses increase the ionization, and Coulomb explosion appears at an intensity of 7×10^{14} W/cm^2. At 4×10^{14} W/cm^2 the probability of bond breaking remains too low for Coulomb explosion to appear in the simulations. At 14×10^{14} W/cm^2 the carbon ions also dissociate and mutually repel

from one another. The kinetic energy of the emitted protons is two times larger for the 15 fs pulse than for the 4.5 fs pulse (see Table 4.1), but further increase of the pulse duration does not increase the kinetic energy in this case.

Figs. 4.3(b) and (c) show the orbital and total ionization versus intensity for pulse durations 15 and 25 fs. At 4×10^{14} W/cm^2, where bond stretching does not occur, the HOMO and HOMO-1 remain the most ionized orbitals. At the higher intensities the enhanced ionization due to bond stretching greatly increases the ionization of the HOMO-2 and HOMO-3. Once again the ionization of the inner orbitals surpasses that of the HOMO and HOMO-1 and now the effect is much more pronounced.

Fig. 4.3(a)-(c) show that in our simulations the HOMO-2 and HOMO-3 dominate the ionization in high intensity laser fields with long pulse widths. As we have noted previously, the HOMO-2 and HOMO-3 are less deeply bound in stretched configurations, see Fig. 4.5(a), and this explains why the HOMO-2 and HOMO-3's ionization increases dramatically with stronger pulses. However, the HOMO-2 and HOMO-3 remain more deeply bound than the HOMO and HOMO-1 even in the stretched configurations. One wishes to further explain why the ionization of the HOMO-2 and HOMO-3 exceeds the ionization of the HOMO and HOMO-1. Several recent experiments [20, 21, 123–129] have also observed greater ionization from the inner orbitals. The experiments attribute this finding to (i) the different geometries of the corresponding orbitals with respect to the direction of the laser field and (ii) an increased ionization coming from the tail of the wave function in the direction of the ionization [129].

The energy ordering HOMO, HOMO-1, etc. refer to "global" properties of the orbitals averaged over space. The above arguments suggest that local properties, i.e. how much binding a certain part of the wave function feels, may play an important role. To illustrate this, Fig. 4.5(b) shows the average density of the ground state orbitals along the alignment axis of the molecule. Although the inner orbitals are more deeply bound, they have an extended weakly bound tail which strongly contributes to the ionization.

This picture is only valid for the ground state–once the laser is turned on ionization starts and the potential and densities change. Nevertheless this picture illustrates the origin of the larger contribution of the inner orbitals.

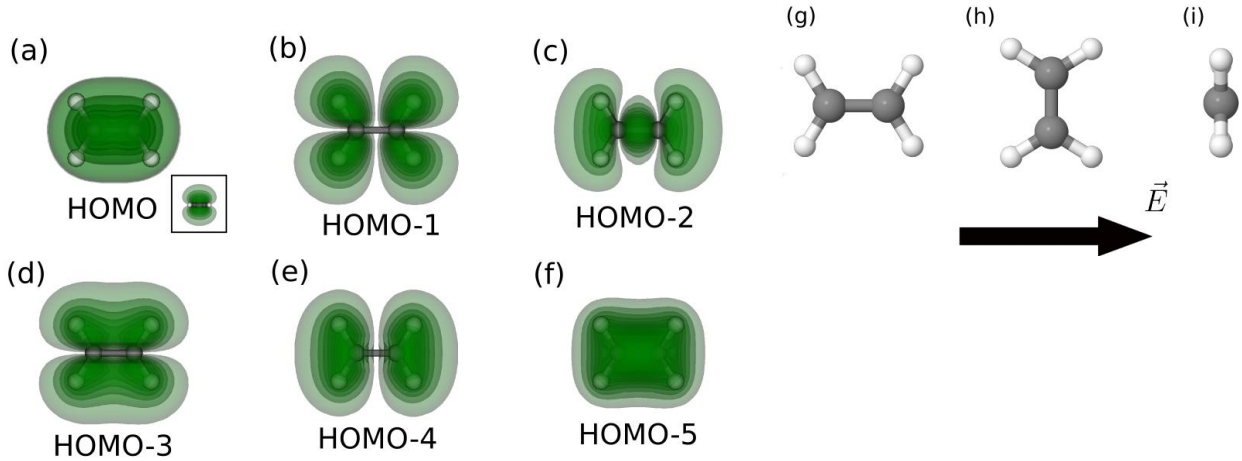

Figure 4.6: (Color online) Ground state Kohn–Sham orbitals of ethylene, C_2H_4. (a) The HOMO with an inset showing a top down view of the HOMO, (b) the HOMO-1, (c) the HOMO-2, (d) the HOMO-3, (e) the HOMO-4, (f) the HOMO-5. Panels (g)-(i) show the three molecular alignments relative to the electric field of the laser that are considered: (g) C-C parallel, (h) C-C bond perpendicular, and (i) all bonds perpendicular to the laser polarization.

4.3.1.2 Acetylene in a laser field polarized perpendicularly to the molecular axis

As the angle between the molecule and the laser field is increased to 22.5° and 45°, the kinetic energy of the protons and the total ionization decreases (see Table 4.1). Eventually, the protons only oscillate in the perpendicular direction. With the molecular alignment axis perpendicular to the laser polarization, 4.5 fs pulses did not produce Coulomb explosion in our simulations. Stronger pulses with a duration of 15 fs and 25 fs proved sufficient, though.

A one dimensional projection of the Coulomb explosion in the perpendicular case is shown in Fig. 4.1(g)-(j). The pulse width is 25 fs and the intensity is 14×10^{14} W/cm^2. Unlike the parallel case, where the Coulomb explosion was due to the interplay of the laser

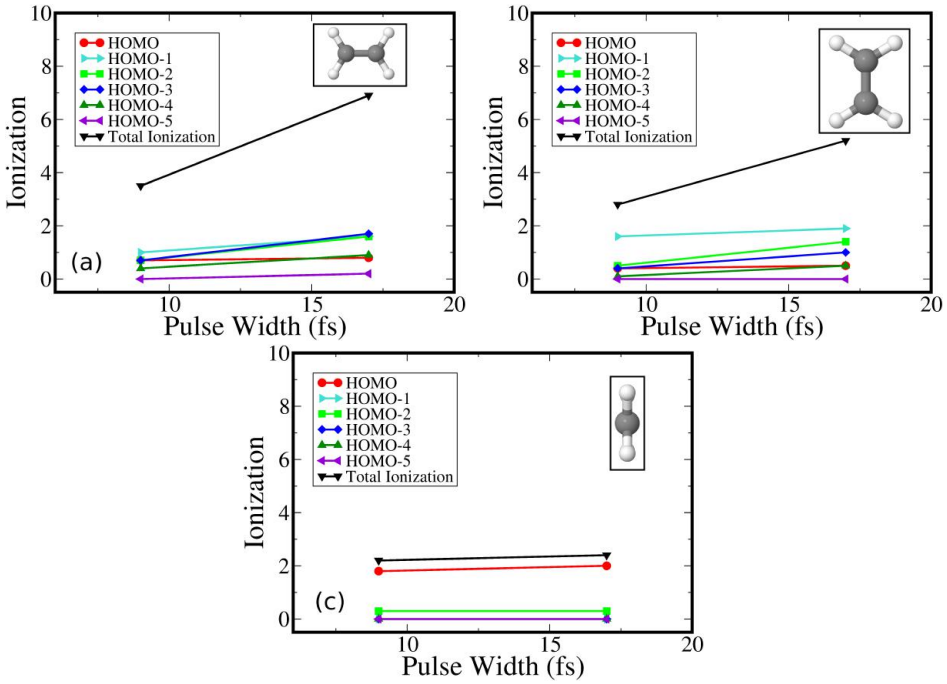

Figure 4.7: (Color online) Total and orbital ionization as a function of laser pulse duration for three alignments of C_2H_4. The laser intensity is fixed at 8×10^{14} W/cm^2. C-C bond (a) parallel, (b) perpendicular to the laser polarization direction with the C-H bonds neither parallel nor perpendicular to it. (c) all bonds are perpendicular to the laser polarization direction.

force on the nuclei, the laser induced oscillation of the electrons, and the ionization, here the fragmentation is only the result of bonds weakened by the ionization. The force exerted on the protons by the perpendicular laser field causes only a slight oscillation in the motion of the protons perpendicular to the molecular axis. However, the main component of the total force is due to the bond breaking and the protons leave in the up and down directions symmetrically. Fig. 4.2(d) shows the force on the protons. For Coulomb explosion to occur a stronger and longer pulse is required than in the parallel case, see Figs. 4.2(a)-(c). However, as seen in the parallel case, the model and Ehrenfest forces are very similar after the peak of the laser field.

We now turn to a more detailed analysis of the ionization dynamics using the the full TDDFT model with Ehrenfest dynamics. Figs. 4.3(d)-(e) show the total and orbital ionization dynamics. Due to the different symmetry, the ionization of the Kohn–Sham orbitals is quite different in the perpendicular case compared to the parallel one. Consider the short 4.5 fs pulse, Fig. 4.3(d). The ionization hierarchy of the orbitals from least to greatest is HOMO-4, HOMO-3, HOMO-2, HOMO, and HOMO-1. The two highest levels are no longer degenerate since the symmetry of the orbitals about the polarization axis has been broken. The tail of the HOMO-1 orbital in the direction of the laser polarization extends much further than any of the other orbitals, see Fig. 4.5(b). Hence, the ionization overwhelmingly comes from the HOMO-1 orbital and it loses more electrons than any of the orbitals in the parallel case.

Even at 14×10^{14} W/cm^2 the 4.5 fs pulse does not induce Coulomb explosion. The two C-H bonds stretch symmetrically from 1.076 Å to 1.553 Å by the time that ionization completes. This moderate increase in the bond length leads to a moderate enhanced ionization of 0.1 electrons relative to the case where the ions are fixed in the ground state, see Fig. 4.3(d). Furthermore, the ionization from the HOMO-2 and HOMO-3 remains small since there is no enhanced ionization.

Pulses with a duration of 15 and 25 fs and a peak intensity of 14×10^{14} W/cm^2 are

now sufficient to cause Coulomb explosion in the simulations. However, the kinetic energy of the emitted protons is about half that of the parallel case (see Table 4.1). The bond stretching leads to an enhanced ionization effect not seen for the 4.5 fs pulses, and there is a substantial increase in the ionization from the HOMO-2, see Figs. 4.3(e)-(f). While the HOMO-2 surpasses the HOMO, the HOMO-1 remains the dominant source of ionization. Unlike the parallel case, the HOMO-3 plays very little role in the total ionization.

4.3.2 Ethylene (C_2H_4)

The ionization and molecular dynamics of ethylene, C_2H_4, has been studied by varying the duration of the laser pulses, see Table 4.1. The two laser pulses that we used exhibit an intensity and duration typical in experiments [117]. Three simple geometric alignments were considered, see Fig. 4.6(g)-(i).

We briefly describe the ions' dynamics observed in our simulations, see Table 4.1. For the geometry with all bonds perpendicular to the laser polarization [Fig. 4.6(i)], the C-H bonds remain essentially unchanged and the C-C bond stretches but dissociation does not occur. For the geometry with only the C-C bond perpendicular to the laser polarization [Fig. 4.6(h)], the C-H bonds break slowly for the 9 fs pulse. At 17 fs the C-H bonds dissociate much more quickly due to the increased ionization. The C-C bond remains nearly unchanged for both pulses. For the geometry with the C-C bond parallel to the laser polarization [Fig. 4.6(g)], all of the C-H bonds fragment via a Coulomb explosion for both pulse durations. At the longer pulse duration of 17 fs the C-C bond also fragments.

We now turn to the orbital ionization dynamics. Fig. 4.7 shows the occupation number of the time–dependent Kohn–Sham orbitals for the three geometries and the two laser pulses. When all bonds are oriented perpendicularly to the laser field [Fig. 4.6(i)], the HOMO nearly completely ionizes. The HOMO-2 is the next most ionized, losing nearly 0.5 electrons. The other orbitals stay unionized. Increasing the duration of the laser pulse has little effect on the orbital and total ionization.

We next consider the geometry where only the C-C bond is oriented perpendicular to the laser field [Fig. 4.6(h)]. The orbital ionization dynamics are dramatically different from the previous case. The HOMO-1 is now the dominant source of ionization. At 9 fs the HOMO, HOMO-2, and HOMO-3 each lose nearly 0.5 electrons while the HOMO-4 and HOMO-5 are barely ionized. At 17 fs the C-H bonds stretch more quickly causing a more pronounced enhanced ionization effect. Owing to both the direct effect of the increased pulse width and the enhanced ionization effect, the total ionization in the 17 fs pulse is increased by about 2 electrons. Furthermore, the inner orbitals HOMO-2, HOMO-3, and HOMO-4 are much more ionized, losing about 1.5, 1, and 0.5 electrons, respectively. The ionization dynamics from the HOMO and HOMO-1 remain essentially unchanged by the increased pulse duration. The HOMO-5 is unionized in either pulse.

Finally, we consider the geometry in Fig. 4.6(g). At a pulse duration of 9 fs the HOMO-1 is again the most ionized orbital, losing nearly one electron. The HOMO, HOMO-2, and HOMO-4 lose nearly 0.75 electrons each. The HOMO-4 loses somewhat less than 0.5 electrons, and the HOMO-5 stays unionized. For the 17 fs pulse, the total ionization is increased by both the direct effect of the longer pulse duration and a more prominent enhanced ionization effect. The enhanced ionization effect is increased since the bonds stretch at a much faster rate in the longer pulse. Hence, the molecule reaches a stretched configuration ($R \geq R_c$) earlier in the ionization process. Furthermore, the ionization of all orbitals except for the HOMO has increased. The HOMO-1, HOMO-2, and HOMO-3 are now nearly completely emptied. The ionization of the HOMO-4 has overtaken the ionization from the HOMO. The ionization from the HOMO-5 increases to nearly 0.25 electrons.

4.4 Summary

In summary, we have studied the ionization dynamics of acetylene, C_2H_2, and ethylene, C_2H_4, in strong laser pulses with various durations and peak intensities for different molec-

ular alignments relative to the linear laser polarization direction using the TDDFT method. It is found that the molecular alignment has a dramatic effect on the total ionization. We have observed that bond stretching and bond breaking leads to an increase of the ionization efficiency, i.e. enhanced ionization, in qualitative agreement with previous theoretical investigations [58–60]. We have also calculated the ionization from individual Kohn-Sham orbitals. It was shown that the enhanced ionization mechanism primarily affects the inner valence orbitals. That is, the inner orbitals are more ionized when bond stretching occurs since they are more weakly bound in the stretched configurations. For some alignments and laser pulse parameters the ionization of the inner orbitals is greater than the highest occupied molecular orbital, owing to ionization from their extended weakly bound tails. Topics for future work include an investigation of larger polyatomic molecules and the effects of circular polarization. Future experiments planned on aligned molecules with short strong laser pulses will be able to test the predictions of this chapter and will stimulate further analysis.

Chapter 5

The Enhanced Ionization Mechanism in Acetylene

5.1 Background

In the previous chapter it was shown that an enhanced ionization mechanism is fundamental to an understanding of the coupled electron and ion dynamics of acetylene and ethylene. Recall that the enhanced ionization (EI) has traditionally been described as a three step process where the C-H bonds first expand to a critical separation, R_c, then ionization proceeds with increased efficiency, and finally H^+ ions are ejected in a highly energetic Coulomb explosion.

In Chapter IV we observed that the ionization efficiency of acetylene (C_2H_2) increases as the C-H bond length is increased. We noted EI's existence but provided no physical explanation or model. We also did not investigate the possible role of a critical separation, R_c, where the enhanced ionization is maximized. In this chapter we shall propose a physical model in which an increasing C-H bond length makes excited states more readily accessible and population is driven efficiently into these excited states. Ionization then proceeds much more efficiently from these excited states leading to the phenomenological enhanced ionization. Most of the computational details are identical to that of Chapter IV, with two exceptions. The first exception is that the molecular dynamics are turned off, i.e. the ions are frozen. The other exception is that the linearly polarized laser pulse shall have an intensity of 8×10^{14} W/cm^2 and a FWHM pulse duration of 4.5 fs.

Our analysis in this chapter will involve the ground state properties of nonequilibrium geometries. The energy ordering of the five Kohn-Sham orbitals changes as the geometry is distorted from equilibrium. We shall therefore now label the Kohn-Sham orbitals by their respective symmetries. In the equilibrium geometry the HOMO, HOMO-1, HOMO-2, HOMO-3, and HOMO-4 orbitals have $1\pi_u$, $1\pi_u$, $3\sigma_g$, $2\sigma_u$, and $2\sigma_g$ symmetries, respec-

tively.

5.2 Results

Fig. 5.1 shows the total ionization and the ionization of the Kohn-Sham orbitals as a function of bond length. Fig. 5.1.a and 5.1.b refer to parallel and perpendicular alignment, respectively. Each point in the plot represents a separate TDDFT simulation with an extended geometry created by symmetrically increasing the C-H bond length. These simulations do not include the Ehrenfest dynamics and hence the ions are frozen in the extended geometry. This gives a measure of the enhanced ionization effect without the complicating effects of the specific trajectory that the H^+ ions may follow. Note that at very high C-H distances, the bond is completely broken and the approximation where the wavefunction may be considered the direct product of molecular orbitals breaks down. The physical interpretation of the Kohn-Sham orbitals as approximations for these molecular orbitals must also break down. The adiabatic local density approximation to the exchange-correlation potential is also known to give inaccurate binding energies at large ion-ion separations. Having noted these caveats, our goal in this analysis is to observe only the qualitative behavior of the orbital ionization as we vary the bond length. In Chapter VI, we shall find that the analysis of static ions given here will provide useful framework for the interpretation of simulations of acetylene driven by circularly polarized pulses which employ the full Ehrenfest dynamics.

Consider first the parallel alignment, as shown in Fig. 5.1.a. Broadly, the total ionization increases until the C-H bond length reaches approximately 2.5 Å, after which there is a slight decrease and eventual plateau. The ionization of the $1\pi_u$ orbitals, which in the equilibrium geometry are the highest occupied molecular orbitals, decreases slightly with C-H bond length. The ionization of the $2\sigma_u$ and $3\sigma_g$ orbitals increase in tandem until R_{CH} reaches approximately 2.5 Å. Subsequently the ionization of the $3\sigma_g$ orbital increases while the ionization of the $2\sigma_u$ orbital decreases after a large spike. The $2\sigma_g$ orbital, which

is much more deeply bound, remains essentially unionized for all bond lengths.

For the perpendicular alignment, shown in Fig. 5.1.a, the total ionization increases and then plateaus. In the equilibrium geometry the $1\pi_{uy}$ orbital dominates the ionization but subsequently drops as the C-H bond is stretched. The ionization of the $4\sigma_g$ orbital rises rapidly and then plateaus. It is the most ionized orbital at high bond lengths. The $2\sigma_u$ orbital's ionization increases moderately and then plateaus. The ionization of the $1\pi_{uz}$ orbital remains essentially flat at moderate ionization, and the $2\sigma_g$ orbital is essentially unionized.

In each of the alignments the total ionization rises and then plateaus. This challenges the notion of a critical separation, R_c, where the ionization is maximized and beyond which the ionization rate should fall. The rise and plateau is consistent with the 3D Hartree Fock calculations of Lötstedt et al. [60] However, it is also well known that the adiabatic local density approximation to the exchange-correlation potential used in our simulations breaks down for large separations between ions. The plateau found both in our calculations and in the Hartree Fock may be an artifact of the lack of an accurate correlation. This remains an open question, which may be investigated either in experiment or in simulations with more accurate exchange-correlation functionals.

To delve more deeply into the dynamics, for the remainder of the chapter we narrow our focus to three particular C-H bond lengths: 1.08 Å, 2.86 Å, and 5.09 Å. The equilibrium bond length is 1.08 Å. Each of these bond lengths provide prototypical examples of three regimes: the equilibrium geometry, intermediate bond length, and large bond length. Fig. 5.2 shows the average position of the total electron density and the individual Kohn-Sham orbitals for the three bond lengths and two alignments. In most cases the electron localization follows the laser pulse adiabatically. The phase of 180° is due to the negative charge of the electron, so that the electron density moves in a direction antiparallel to the electric field. When R_{C-H}=2.86 Å and the alignment is parallel to the laser polarization the dynamics do not proceed adiabatically (Fig. 5.2.b). In particular the $2\sigma_u$ orbital becomes

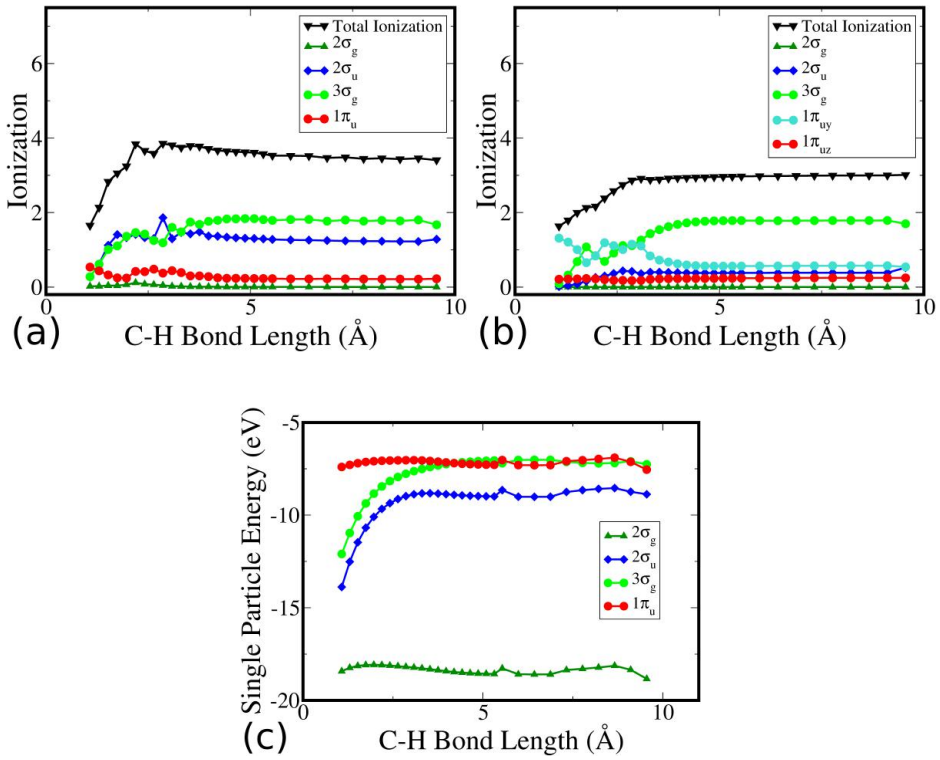

Figure 5.1: (Color online) Panels (a) and (b) show the total ionization and orbital ionization of Acetylene (C_2H_2) as a function bond length for (a) parallel and (b) perpendicular alignment of the molecular axis relative to the laser axis. The laser intensity is 8×10^{14} W/cm^2, the FWHM pulse duration is 4.5 fs, and linear polarization. Each point represents a separate TDDFT calculation with fixed ions. The ionization increases with the bond length and then plateaus after the bond length has reached a critical separation. This result is consistent with previous theoretical results using three-dimensional Time-Dependent Hartree Fock [60]. A sharp decrease in the ionization after a critical separation, R_c, does not appear. Panel (c) shows the ground state single particle energies of the individual Kohn-Sham orbitals as the bond length increases.

localized to one side of the molecule and the ionization from this orbital is extremely efficient. This accounts for the spike in the ionization of this orbital observed in Fig. 5.1.a.

We now consider an analysis of electronic population transfer into excited states. In the TDDFT the time-dependent Kohn-Sham orbitals are, in principle, a superposition of the ground state, excited states, and continuum states. However, the TDDFT does not provide these excited states directly. In order to analyze the population transfer between the electronic ground and excited states we diagonalize the ground state Kohn-Sham Hamiltonian from the DFT theory for each of the three geometries. We find that the nine eigenvectors with lowest eigenvalue are well converged. The lowest five eigenvectors are simply the usual Kohn-Sham orbitals whose sum squared give the ground state electron density. We label the next four eigenvectors by their symmetry, the $1\pi_{gy}$, $1\pi_{gz}$, $3\sigma_u$, and $4\sigma_g$ orbitals. We shall henceforth refer to them as the excited states of the acetylene molecule.

In Fig. 5.3 we show the inner products between the time-dependent Kohn-Sham orbitals from TDDFT and the four excited states derived from DFT. In Fig. 5.3 (a), (b), and (c) we show the results for parallel alignment. The salient feature of these plots is that as the bond length is increased electron population is ever more readily transferred into the excited states. This population transfer may occur prior to or in tandem with the ionization.

This leads us to the following model of the enhanced ionization. The electron and ion motions are highly coupled. As the ionization begins the C-H bond lengths begin to increase. The increased bond lengths distort energy levels and nodal geometries of the excited states which allows an efficient population transfer of the remaining unionized electrons from their ground state orbitals into the excited states. Ionization from these now populated excited states is highly efficient, leading to an enhancement in the ionization.

In Fig. 5.3 (d), (e), and (f) we show the excitations for the perpendicular alignment. In this case, the excitement of inner valence orbitals into excited states seems to peak at intermediate bond lengths and decrease at large bond lengths. At large bond lengths, the ionization of the $3\sigma_g$ orbital appears to undergo a vertical ionization from the orbital without an intermediary excitation step. Despite the lack of excitation prior to ionization,

the ionization efficiency of this orbital is larger than at the intermediate bond lengths (see Fig. 5.1.b). Nevertheless at intermediate bond lengths, the excitation-ionization model proposed above for the parallel alignment remains relevant.

5.3 Conclusions

We have investigated the enhanced ionization of acetylene using fixed ion calculations with several extended geometries with increased C-H bond lengths. We observed that the ionization efficiency increases and then plateaus. The core results found here is that the population transfer into excited states becomes more efficient with increasing bond length. We propose that at large bond lengths the electrons are first efficiently transferred into the excited states, and then the ionization proceeds very efficiently from the excited states. This model explains the enhanced ionization effects observed in both theory and experiment. These calculations may be used to motivate future experimental work and simulations with highly accurate exchange-correlation functionals.

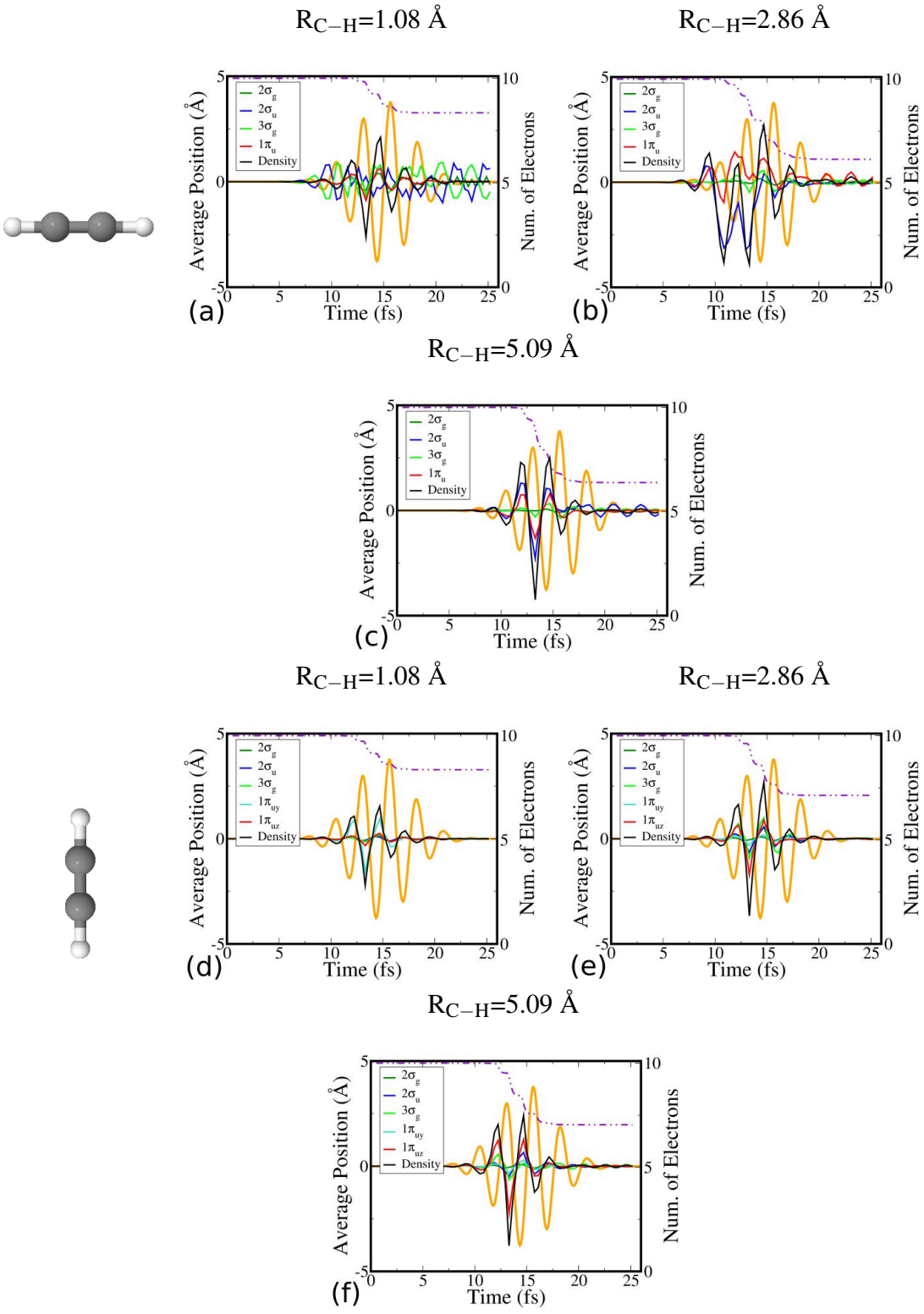

Figure 5.2: (Color online) The average position of the density, $\langle x \rangle(t) = \int x \rho(r,t)\, d^3r$, and individual time-dependent Kohn-Sham orbitals $\langle x \rangle(t) = \int x\, \phi(r,t)\, d^3r$ where x is the laser polarization axis. The laser intensity is 8×10^{14} W/cm^2, the FWHM pulse duration is 4.5 fs, and linear polarization. Three bond lengths are shown: (a, d) 1.08 Å, (b, e) 2.86 Å, and (c, f) 5.09 Å. Additionally, two alignments of the molecular axis relative to the laser axis are shown: (a)-(c) parallel, and (d-f) perpendicular.

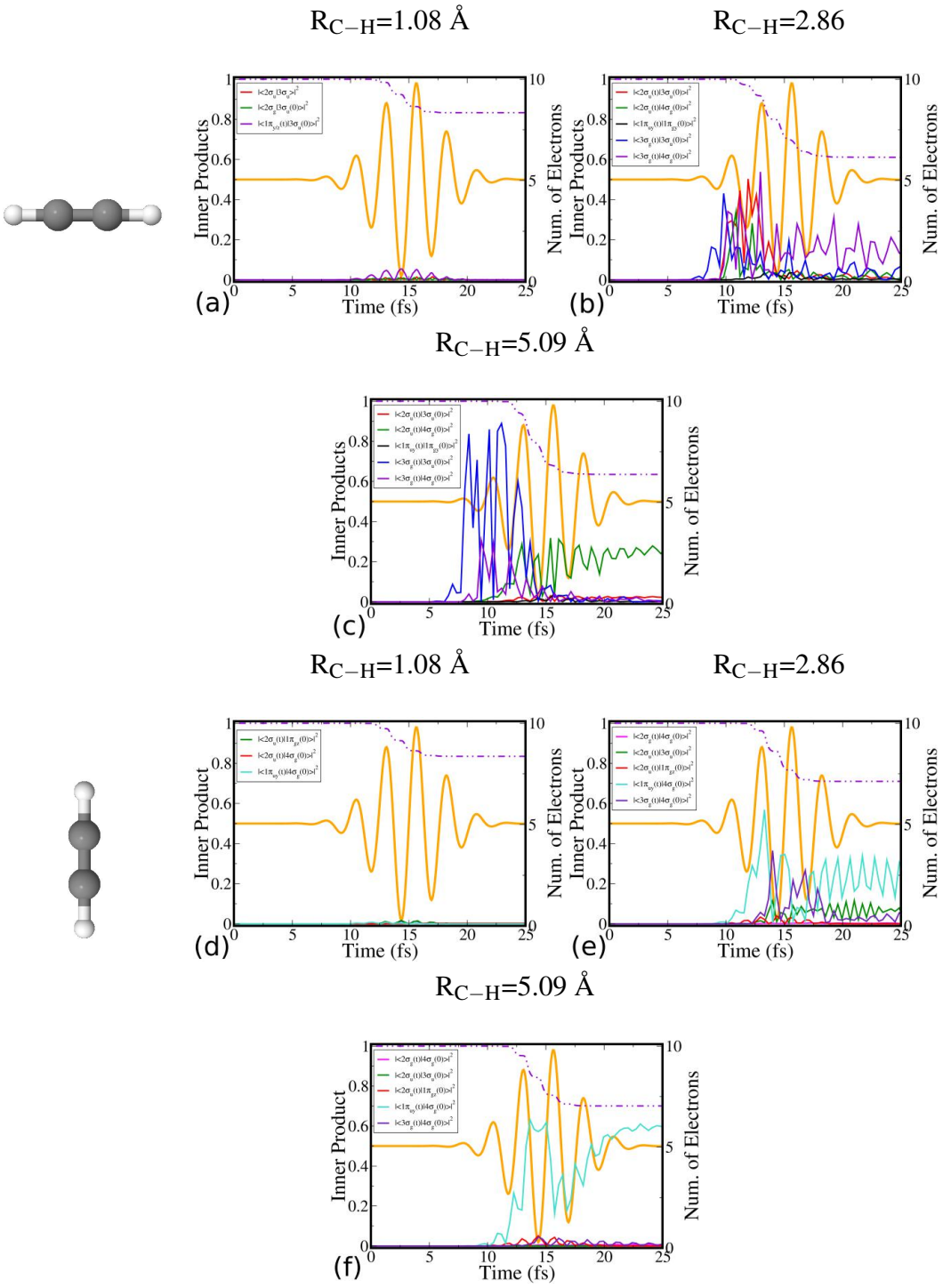

Figure 5.3: (Color online) Inner products between the time-dependent Kohn-Sham orbitals, calculated with TDDFT, and four LUMO states, calculated in ground-state DFT, during ionization induced by a laser field. Only non-zero projections are shown. The laser intensity is 8×10^{14} W/cm^2, the FWHM pulse duration is 4.5 fs, and linear polarization. Three bond lengths are shown: (a, d) 1.08 Å, (b, e) 2.86 Å, and (c, f) 5.09 Å. Additionally, two alignments of the molecular axis relative to the laser axis are shown: (a)-(c) parallel, and (d-f) perpendicular.

Chapter 6

Fragmentation and Ionization of Acetylene and the Hydrogen Molecule induced by Strong Short Circularly Polarized Laser Fields

6.1 Introduction

In this chapter we shall investigate the multi-electron ionization and fragmentation of small molecules driven by circularly polarized pulses. Recall from chapter I that multi-electron ionization may be broadly divided into two categories: sequential [130, 131] and nonsequential [10, 12, 132–134]. The double ionization of molecules has been an active topic of recent research. For sequential double ionization (SDI) each electron is ejected one at a time, a process well described by the single-active-electron model [17, 18, 118, 119]. In nonsequential double ionization both electrons are ejected simultaneously, and the electron dynamics are therefore highly correlated [9].

In chapter I the electron recollision model was introduced. This is typically considered to be the dominant mechanism by which Non-Sequential Double Ionization (NSDI) occurs for molecules driven by linearly polarized pulses. In the NSDI, first an electron is ionized and then upon reversal of the field the electron is driven back to the parent molecule where the recollision leads to excitation or ionization of a second electron [15, 135].

Previously it was expected that in a circularly polarized laser field the recollision processes would be suppressed since there is no reversal of the laser field. Xie et al. [46] experimentally observed the CH_2^+/H^+ fragmentation channel of acetylene (C_2H_2) induced by either a linearly or circularly polarized laser pulse pulses. It was found that H^+ ion kinetic energies greater than 4.5 eV were suppressed for the circularly polarized pulse, despite its similar intensity and duration to the linearly polarized pulse. This was attributed to the suppression of nonsequential double ionization events such as recollision.

On the other hand, NSDI events have been experimentally observed for the molecules

NO and O_2 subjected to circularly polarized pulses [136]. Theoretically, Tong et al. [137] used a classical ensemble approach to show that NSDI occurs for H_2 driven by a circularly polarized pulse. Furthermore, they showed that the NSDI is due to a recollision process where an electron localized at one ion site is driven along an elliptical path to the other ion site. The first electron then collides with and ionizes the second electron. This recollision process becomes more probable for extended molecular geometries. Yuan et al. [138] solved the two-dimensional time-dependent Schrödinger equation for H_2^+ and showed that recollision electron dynamics with extended molecular geometries may also be used in the generation of high-order elliptically polarized harmonics of the fundamental laser frequency.

In addition to the dependence on bond length, the ionization of molecules is also dependent on the alignment of the molecule relative to the polarization vector. For a linear molecule, the alignment is uniquely determined by the angle between the molecular axis and the laser's polarization vector. Ionization is maximized when this angle is zero [104, 139]. In a circularly polarized laser field, angular streaking deflects the ionized electron. This angular streaking occurs since the Coulomb potential produced by the nuclei of the molecule is not spherically symmetric [140]. If the tunneling ionization time is instantaneous and the initial electron momentum is zero, then the circularly polarized field deflects the ionized electron by 90°. Hence for linear molecules, the peak of a measured photoelectron spectrum is typically perpendicular to the molecular axis [141, 142]. However, measurements of the ionization H_2^+ give peak ionization angles between 15° and 45° [143, 144], implying a more complex electron dynamics.

Bandrauk et al. [145] considered the effects of the enhanced ionization of H_2^+ driven by a circularly polarized pulse with polarization vector always perpendicular to the molecular axis. By solving the 3D Schrödinger equation for various extended bond lengths, they obtained ionization rates as a function of bond length. They found that the ionization rate increases and then plateaus as the bond length is increased.

In this manuscript we present an in depth investigation of the coupled ionization and fragmentation dynamics of H_2 and C_2H_2 driven by circularly polarized strong laser fields by performing TDDFT calculations coupled with the Ehrenfest dynamics. We consider various intensities and pulse durations typical in experiment [46, 111], two different alignments, and compare the dynamics driven by a circularly polarized pulse to linearly polarized pulses of similar strength.

In section II we shall discuss the computational details of the TDDFT simulations, and in section III we describe the results of the simulations, and in section IV we give a short discussion comparing our results with previous theoretical and experimental investigations.

6.2 Computational Details

The computational results presented in the next section use the following parameters. The rectangular box is given by $L_x = L_y = L_z = 34$ Å. The molecular axis lies in the x direction. The grid spacing is 0.25 Å in each direction. The CAP is nonzero in a region 5 Å from the walls of the simulation cell. The time step for the propagation of the wave function is $\delta t = 0.0007$ fs. The equation of the ionic motion [Eq. (2.40)] is solved with the Verlet algorithm with time step 0.0028 fs. These parameters lead to very well converged results. The calculated ionization potential is 11.8 eV for C_2H_2, comparable with the experimental value 11.4 eV [122].

As in chapter IV, we shall calculate the ionization of the molecule using Eq. 2.30, and refer to the quanity $N(0) - N(t)$ as the ionization of the molecule.

6.3 Results

6.3.1 Hydrogen Molecule (H_2)

In this section we present the simulation results for the H_2 molecule. In the first subsection the molecular axis is aligned parallel to one of the circularly polarized pulse's polar-

ization vectors, and in the following subsection the molecular axis is perpendicular to both of the circularly polarized pulse's polarization vectors.

6.3.1.1 Polarization vectors along the x and y axes

Columns (1-2) of Fig. 6.1 show the ionization and fragmentation of an H_2 molecule driven by circularly polarized laser pulse whose polarization vectors, $\hat{\mathbf{k_1}}$ and $\hat{\mathbf{k_2}}$, lie along the x and y axes respectively [see Eq. (2.36)]. The linear molecule initially lies along the x axis. Two laser intensities, and $4 \cdot 10^{14}$ and $14 \cdot 10^{14} \frac{\mathrm{W}}{\mathrm{cm}^2}$, and two full width half maximum (FWHM) pulse widths, 4.5 and 25 fs, were considered for a total of four laser pulses. The wavelength of all considered pulses is 790 nm. We also compare these results to two separate simulations where the dynamics are driven by linearly polarized pulses of the same intensity and pulse width. We consider linear polarizations aligned along either the x or y axis.

As shown in Fig. 6.1.a, a circularly polarized laser pulse of intensity $4 \cdot 10^{14} \frac{\mathrm{W}}{\mathrm{cm}^2}$ and pulse width 4.5 fs, ionizes the molecule by 0.63 electron. The pulse is too weak to break the H-H bond, and only a small oscillation is observed (see Fig. 6.1.b). The Ehrenfest dynamics represent an averaging of the possible fragmentation channels, and the lack of bond breaking implies that the probability of fragmentation is small. A linearly polarized pulse with polarization vector aligned along the x axis ionizes 0.38 electrons, and one aligned along the y axis ionizes 0.32 electron. Since the circularly polarized pulse is simply the sum of two orthogonal linearly polarized pulses with phase shift $\frac{\pi}{2}$, one asks if the ionization is simply the sum of ionization from the two separate linearly polarized pulses. In this case, the ionization driven by the circularly polarized pulse is somewhat smaller than the sum of the individual linear components.

At first glance, the simulations with linearly polarized pulses seem to imply that the ionization rate induced by the circularly polarized pulse will be greater along the x axis than along the y axis. While the strongest ionization does occur when the polarization

vector of the pulse is aligned with the x axis, angular streaking will occur and the peak in the photoelectron spectrum will be at some angle relative to the x axis [140–144].

In Fig. 6.1.e, the intensity is $4 \cdot 10^{14} \frac{\mathrm{W}}{\mathrm{cm}^2}$ and pulse width is 25 fs. The circularly polarized pulse induces an ionization of 1.90 electrons. This large ionization causes a Coulomb explosion and the two H^+ ions move apart with trajectories that lie essentially along the x axis (see Fig. 6.1.f). The corresponding parallel and perpendicular linearly polarized pulses induce an ionization of 0.90 and 0.68 electron, respectively. Unlike the previous laser parameters, the sum of the ionization induced by the two separate linear pulses, 1.58 electrons, is smaller than the ionization induced by the circularly polarized pulse. The key difference between the linearly and circularly polarized pulses here is that the linearly polarized pulses do not induce a Coulomb explosion. As the H-H bond length increases the ionization efficiency also increases, a mechanism known as enhanced ionization. Since the enhanced ionization mechanism occurs for the circularly polarized pulse, its ionization is much more efficient than either of its linear components alone.

At an intensity of $14 \cdot 10^{14} \frac{\mathrm{W}}{\mathrm{cm}^2}$ and a pulse width of 4.5 fs, the circularly polarized pulse and two linearly polarized pulses all induce Coulomb explosion (see Fig. 6.1.j). Enhanced ionization occurs for all three pulses and the ionization induced by each of the two linearly polarized pulses, 1.58 and 1.28 electrons for the x and y alignments respectively, sum to greatly exceed the ionization of the circularly polarized pulse, which is 1.97 electrons (see Fig. 6.1.i).

At an intensity of $14 \cdot 10^{14} \frac{\mathrm{W}}{\mathrm{cm}^2}$ and pulse width of 25 fs, the linearly and the circularly polarized pulses all have sufficient strength to ionize the molecule completely (Fig. 6.1.m). The rate of ionization for the circularly polarized pulse is somewhat higher. All three pulses induce Coulomb explosion (see Fig. 6.1.n). Typically, the fragmentation dynamics drive H^+ ions along the x axis. However, at this particular intensity and duration the circularly polarized pulse induces a small but non-negligible motion in the y axis. This y axis motion is not observed for the linearly polarized pulses even when the polarization vector lies along

the y axis.

6.3.1.2 Polarization vectors along the y and z axes

Columns 3 and 4 of Fig. 6.1 show the ionization and fragmentation dynamics when the laser pulse's polarization vectors, $\hat{\mathbf{k_1}}$ and $\hat{\mathbf{k_2}}$, lie along the z and y axes respectively [see Eq. (2.36)]. We only consider linear polarization aligned along the y axis since, by symmetry, a linearly polarized pulse aligned along the z axis would produce the same ionization and fragmentation as one along the y axis.

As shown in Fig. 6.1.c, a circularly polarized laser pulse of intensity $4 \cdot 10^{14} \frac{\mathrm{W}}{\mathrm{cm}^2}$ and pulse width 4.5 fs ionizes the molecule by 0.54 electron, which is smaller than the corresponding ionization induced when the alignment of the polarization vectors lie along the x and y axes. Since the ionization is even smaller at this alignment it is unsurprising that the H-H bond remains unbroken and only a small oscillation is observed (see Fig. 6.1.d). The corresponding linearly polarized pulse aligned along the y axis ionizes 0.32 electron, and the ionization due to the circularly polarized pulse is smaller than the sum from two corresponding linearly polarized pulses.

At an intensity of $4 \cdot 10^{14} \frac{\mathrm{W}}{\mathrm{cm}^2}$ and a pulse width of 25 fs, the circularly polarized pulse ionizes the molecule by 1.13 electrons (see Fig. 6.1.g). The linearly polarized pulse ionizes 0.68 electron. No bond breaking is observed for any of the pulses (see Fig. 6.1.h). Hence, unlike the previous alignment, there is no enhanced ionization and the circularly polarized pulse induces less ionization than the sum from two corresponding linear pulses.

The dynamics of the remaining two pulses (Fig. 6.1.k and 6.1.o) are qualitatively quite similar for either alignment and we do not remark on them any further.

6.3.2 Acetylene (C_2H_2)

In this section we present the simulation results for the C_2H_2 molecule. We again break down the results into two subsections according to alignment.

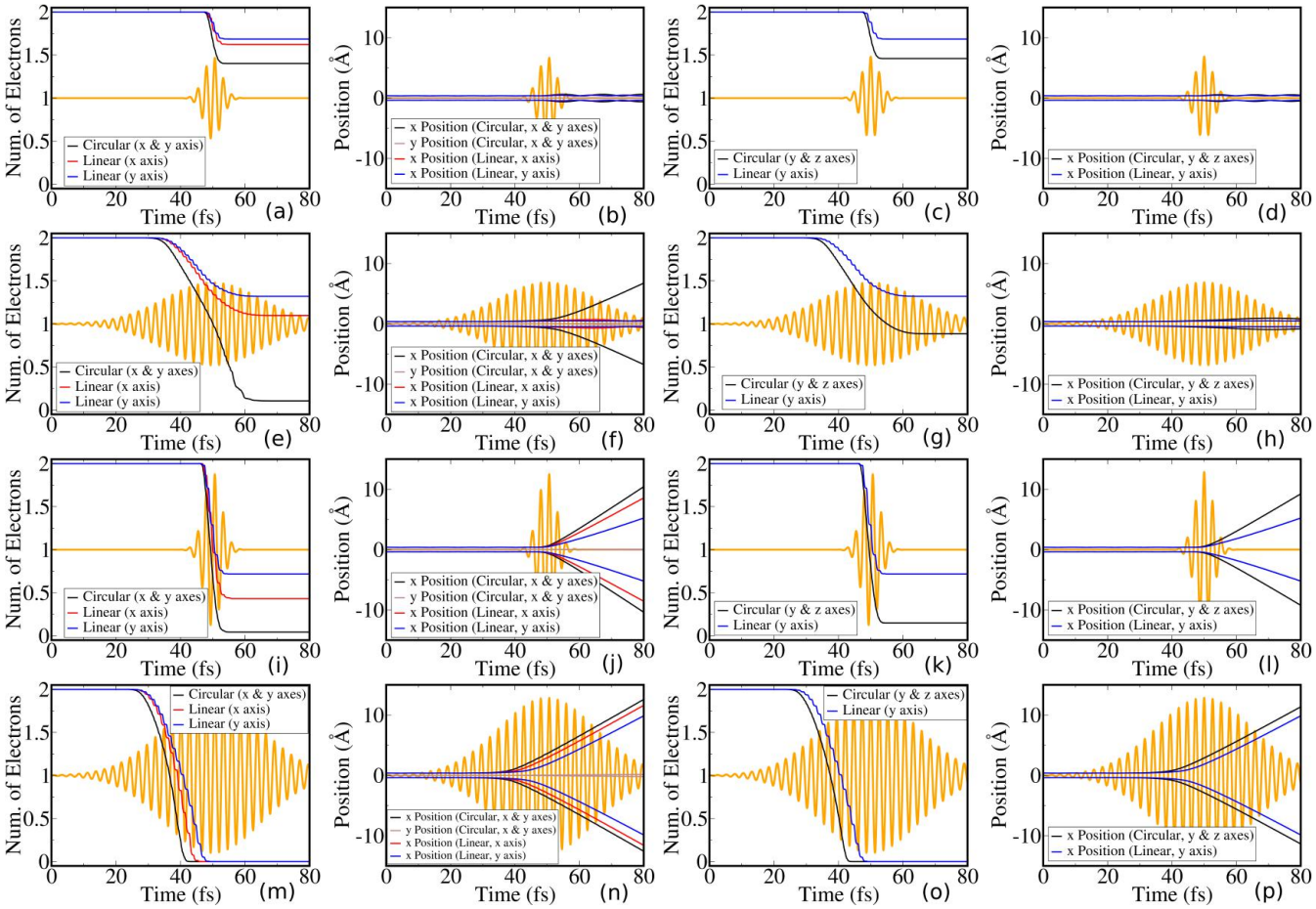

Figure 6.1: (Color online) Ionization and H^+ ion positions of H_2 under the influence of a circularly polarized laser pulse. The H_2 molecule initially lies along the x axis. The circularly polarized pulse consists of two orthogonal linearly polarized pulses with a phase difference of $\frac{\pi}{2}$ between them. The polarization vectors of these composite linear pulses lie along the x and y axes in columns (1-2) and along the y and z axes in columns (3-4). Columns (1) and (3) show the total ionization of the molecule and columns (2) and (4) show the position of the H^+ ions. For comparison, in each panel the total ionization and ion positions due to a single linearly polarized pulse is shown. The wavelength of all considered pulses is 790 nm. For panels (a-h) the laser intensity is $4 \cdot 10^{14} \frac{\mathrm{W}}{\mathrm{cm}^2}$ and in panels (i-p) it is $14 \cdot 10^{14} \frac{\mathrm{W}}{\mathrm{cm}^2}$. For panels (a-d) and (i-m) the FWHM pulse width is 4.5 fs, and in panels (e-h) and (m-p) the FWHM pulse width is 25 fs.

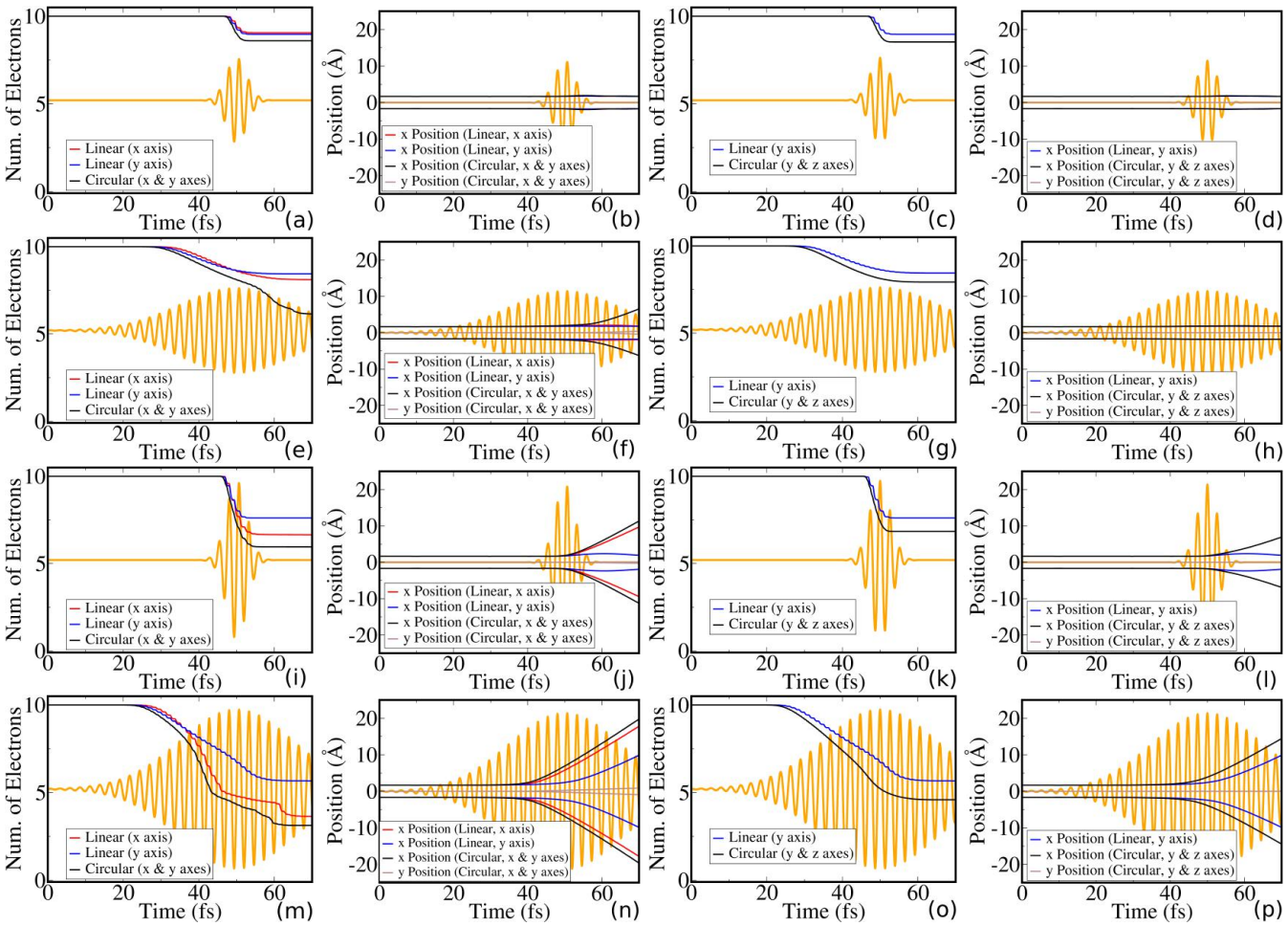

Figure 6.2: (Color online) Ionization and H^+ ion positions of C_2H_2 under the influence of a circularly polarized laser pulses. The molecule initially lies along the x axis. The circularly polarized pulse consists of two orthogonal linearly polarized pulses with a phase difference of $\frac{\pi}{2}$ between them. The polarization vectors of these composite linear pulses lie along the x and y axes in columns (1-2) and along the y and z axes in columns (3-4). Columns (1) and (3) show the total ionization of the molecule, and columns (2) and (4) show the position of the H^+ ions. For comparison, in each panel the total ionization and ion positions due to a single linearly polarized pulse is shown. The wavelength of all considered pulses is 790 nm. For panels (a-h) the laser intensity is $4 \cdot 10^{14} \frac{\mathrm{W}}{\mathrm{cm}^2}$ and in panels (i-p) it is $14 \cdot 10^{14} \frac{\mathrm{W}}{\mathrm{cm}^2}$. For panels (a-d) and (i-m) the FWHM pulse width is 4.5 fs, and in panels (e-h) and (m-p) the FWHM pulse width is 25 fs.

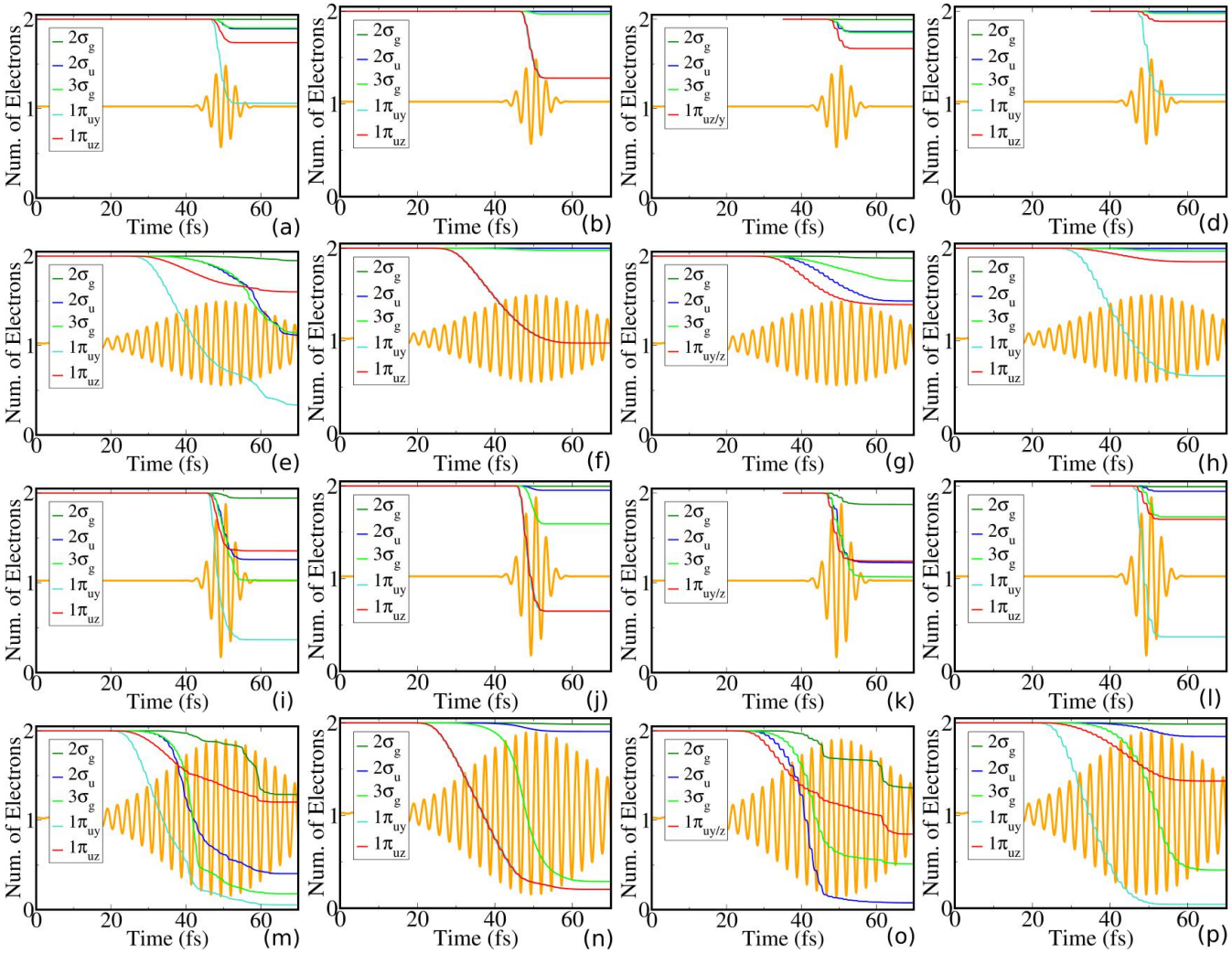

Figure 6.3: (Color online) Ionization of the time-dependent Kohn-Sham orbitals of C_2H_2 under the influence of a circularly or linearly polarized laser pulse. The linear molecule initially lies along the x axis. Columns (1-2) show the orbital ionization due to a circularly polarized laser pulse, which consists of two orthogonal linearly polarized fields, which lie along the x and y axes in column (1) and along the y and z axes in column (2), with a phase difference of $\frac{\pi}{2}$ between them. For comparison, columns (3-4) show the orbital ionization due to a linear laser pulse whose polarization vector lies along the x axis in column (3) and the y axis in column (4). The wavelength of all considered pulses is 790 nm. For panels (a-h) the laser intensity is $4 \cdot 10^{14} \frac{\mathrm{W}}{\mathrm{cm}^2}$ and in panels (i-p) $14 \cdot 10^{14} \frac{\mathrm{W}}{\mathrm{cm}^2}$. For panels (a-d) and (i-m) the FWHM pulse width is 4.5 fs, and in panels (e-h) and (m-p) the FWHM pulse width is 25 fs. For ease of comparison to the other panels, the plots in panels (c),(d),(k), and (l) have been shifted such that the peak of the laser's Gaussian envelope occurs at 50 fs.

6.3.2.1 Polarization vectors along the *x* and *y* axes

Columns (1-2) of Fig. 6.2 show the ionization and fragmentation dynamics of a C_2H_2 molecule driven by a circularly polarized laser pulse whose polarization vectors, $\hat{\mathbf{k_1}}$ and $\hat{\mathbf{k_2}}$, lie along the *x* and *y* axes respectively [see Eq. (2.36)]. As with H_2, the linear C_2H_2 molecule initially lies along the *x* axis.

As shown in Fig. 6.2.a, a circularly polarized pulse of intensity $4 \cdot 10^{14} \frac{\mathrm{W}}{\mathrm{cm}^2}$ and pulse width 4.5 fs ionizes the molecule by 1.41 electrons. This pulse is too weak to break the C-H bond (see Fig. 6.2.b).A linearly polarized pulse aligned along the *x* axis ionizes 0.95 electron, and *y* axis alignment induces an ionization of 1.04 electrons, and the circularly polarized pulse induces ionization smaller than the sum from two corresponding linear pulses.

In Fig. 6.2.e, the intensity is $4 \cdot 10^{14} \frac{\mathrm{W}}{\mathrm{cm}^2}$ and pulse width is 25 fs. The circularly polarized pulse induces an ionization of 3.86 electrons. In this case the ionization is sufficient to cause a Coulomb explosion, and the two H^+ move apart essentially along the molecular axis (*x* axis) with a very small separation along the *y* axis (see Fig. 6.2.f). The corresponding linearly polarized pulses aligned along the *x* and *y* axes induce an ionization of 1.93 and 1.58 electrons, respectively, but do not induce Coulomb explosion. Just as for H_2, at this pulse strength the circularly polarized pulse benefits from enhanced ionization as the C-H bonds increase, leading to a highly efficient ionization which surpasses the sum of the two individual linearly polarized pulses.

In Fig. 6.2.i, where the intensity is $14 \cdot 10^{14} \frac{\mathrm{W}}{\mathrm{cm}^2}$ and pulse width is 4.5 fs, a circularly polarized pulse induces an ionization of 4.07 electrons, while the corresponding linearly polarized pulses aligned along the *x* and *y* axes induce an ionization of 3.37 and 2.40 electrons, respectively. The circularly polarized pulse and the linearly polarized pulse aligned along the *x* axis are of sufficient strength to induce Coulomb explosion (see Fig. 6.2.j). When the linearly polarized pulse is aligned along the *y* axis the C-H bond does not break. While only the *x* aligned linear pulse experiences enhanced ionization, this is sufficient to

insure that the ionization induced by the circularly polarized pulse is smaller than the sum of the two linearly polarized pulses.

A circularly polarized pulse with intensity $14 \cdot 10^{14} \frac{\mathrm{W}}{\mathrm{cm}^2}$ and pulse width 25 fs ionizes 6.90 electrons (see Fig. 6.2.m). Meanwhile corresponding linearly polarized pulses aligned along the x or y axis ionize the molecule 6.38 and 4.37 electrons, respectively. The sum of the two individual pulses would exceed 10 electrons, the total number of valence electrons, but the circularly polarized pulse induces only somewhat more ionization than just the x axis aligned linearly polarized pulse. All three pulses have sufficient strength to induce Coulomb explosion (see Fig. 6.2.n). For the circularly polarized pulse there is a significant amount of motion in the y direction.

The C_2H_2 molecule has five Kohn-Sham (KS) orbitals and hence the ionization dynamics are much more complex than that of H_2, which only has one KS orbital. For the remainder of this section we consider the ionization from individual KS orbitals induced by the circularly and linearly polarized pulses.

Fig. 6.3.a shows the ionization of the KS orbitals induced by the circularly polarized pulse of intensity $4 \cdot 10^{14} \frac{\mathrm{W}}{\mathrm{cm}^2}$ and pulse width of 4.5 fs. The ionization due to linearly polarized pulses aligned along the x and y axes are shown in Fig. 6.3.c and 6.3.d, respectively. The orbital ionization induced by the circularly polarized pulse shares many of the features seen for the linearly polarized pulses. In particular, the ionization of most of the KS orbitals in Fig. 6.3.a qualitatively similar to the ionization observed in Fig. 6.3.c. However the circularly polarized pulse induces a very large ionization of the $1\pi_{uy}$ orbital, comparable to the ionization observed in Fig. 6.3.d.

Fig. 6.3.e shows the orbital ionization due to a circularly polarized laser pulse with intensity $4 \cdot 10^{14} \frac{\mathrm{W}}{\mathrm{cm}^2}$ and pulse width 25 fs. Interestingly, the $2\sigma_u$ and $3\sigma_g$ orbitals show a very large ionization which is not observed for either linearly polarized pulse (see Fig. 6.3.g and 6.3.h). The ionization of these two orbitals exceeds the ionization of the $1\pi_{uz}$ orbital. The $1\pi_{uz}$ orbital is one of the two highest occupied molecular orbitals (HOMO) prior to

the application of the laser, which breaks the orbital's symmetry with the $1\pi_{uy}$ orbital. The increased ionization of the inner σ orbitals is indicative of an enhanced ionization mechanism, where the ionization of the inner orbitals becomes more efficient as the C-H bond length is increased [104, 111]. Indeed, as was noted above the circularly polarized pulse induces bond breaking while the individual linearly polarized pulses do not. This explains the qualitative differences in the ionization of the $2\sigma_u$ and $3\sigma_g$ orbitals.

Fig. 6.3.i shows the orbital ionization due to a circularly laser pulse with intensity $14 \cdot 10^{14} \frac{\mathrm{W}}{\mathrm{cm}^2}$ and pulse width 4.5 fs. Since the bond breaking and enhanced ionization occur for both the circularly polarized pulse and the linearly polarized pulse aligned along the x axis (Fig. 6.3.k), the ionization induced by these two pulses of the inner $2\sigma_u$ and $3\sigma_g$ orbitals are qualitatively similar.

At intensity $14 \cdot 10^{14} \frac{\mathrm{W}}{\mathrm{cm}^2}$ and pulse width 25 fs, the circularly polarized pulse and the linearly polarized pulses all induce bond breaking (see Fig. 6.2.m, 6.2.o, and 6.2.p). One might expect that for the circularly polarized pulse the ionization of each of the KS orbitals would be strictly greater than that of either linear pulse alone. However, the ionization of the $2\sigma_u$ and $1\pi_{uz}$ orbitals induced by the circularly polarized pulse (see Fig. 6.3.m) is significantly less than that of the linearly polarized pulse aligned along the x axis (see Fig. 6.3.o). The orbital ionization dynamics here are very complex compared to the previous cases and cannot be explained simply by either the presence or absence of enhanced ionization.

In the enhanced ionization model as is usually described [115], the C-H bond length increases to a critical separation and then the ionization proceeds instantaneously at a fixed C-H bond length. However, the ionization does not occur instantaneously and the bond length changes even as the ionization proceeds. The ionization efficiency will therefore depend on the exact trajectories of the H^+ ions. As shown in Chapter V, the enhanced ionization mechanism affects the KS orbitals of C_2H_2 differently if the ionization occurs in a state of very large C-H bond lengths relative intermediate C-H bond lengths. For instance it was shown that for a linearly polarized pulse with polarization along the x axis, as the C-

H bond length is increased from equilibrium up to about 3 Å the ionization efficiency of the $3\sigma_g$ and $2\sigma_u$ orbitals both increase and are nearly identical. However, as the bond lengths are increased further the ionization efficiency of the $3\sigma_g$ increases while the ionization efficiency of the $2\sigma_u$ decreases. Fig. 6.2.n shows that for the circularly polarized pulse the H^+ ions move more quickly, and therefore some fraction of the ionization time occurs while the C-H bond lengths are large. Meanwhile, for the linearly polarized pulse aligned along the x axis the ionization occurs at intermediate bond lengths. Hence the ionization of the $3\sigma_g$ is greater in Fig. 6.3.m than in Fig. 6.3.o, while the ionization of the $2\sigma_u$ is smaller. Similarly, at very large C-H bond lengths the ionization efficiency of the $1\pi_{uz}$ orbital decreases explaining why the ionization of this orbital is smaller in in Fig. 6.3.m than in Fig. 6.3.o.

6.3.2.2 Polarization vectors along the y and z axes

Columns (3-4) of Fig. 6.2 show the ionization and fragmentation of a C_2H_2 molecule due to a circularly polarized laser pulse whose polarization vectors, $\hat{\mathbf{k_1}}$ and $\hat{\mathbf{k_2}}$, lie along the z and y axes respectively [see Eq. (2.36)].

As shown in Fig. 6.2.c, a circularly polarized laser pulse of intensity $4 \cdot 10^{14} \frac{\mathrm{W}}{\mathrm{cm}^2}$ and pulse width 4.5 fs ionizes the molecule by 1.47 electrons The linearly polarized pulse pulse ionizes 1.04 electrons. Neither pulse breaks C-H bond (see Fig. 6.2.d and 6.2.h), and since enhanced ionization does not occur for either pulse the ionization of the circularly polarized pulse is smaller than the sum induced by two linearly polarized pulses of the same intensity and duration.

At an intensity of $14 \cdot 10^{14} \frac{\mathrm{W}}{\mathrm{cm}^2}$ and a pulse width of 4.5 fs, the circularly polarized pulse induces an ionization of 3.2 electrons, while the corresponding linearly polarized pulse induces an ionization of 2.40 electrons (see Fig 6.2.k). Only the circularly polarized pulse is sufficiently strong to induce Coulomb explosion (see Fig. 6.2.l). However, the bond length only increases significantly after the ionization has already completed and very little

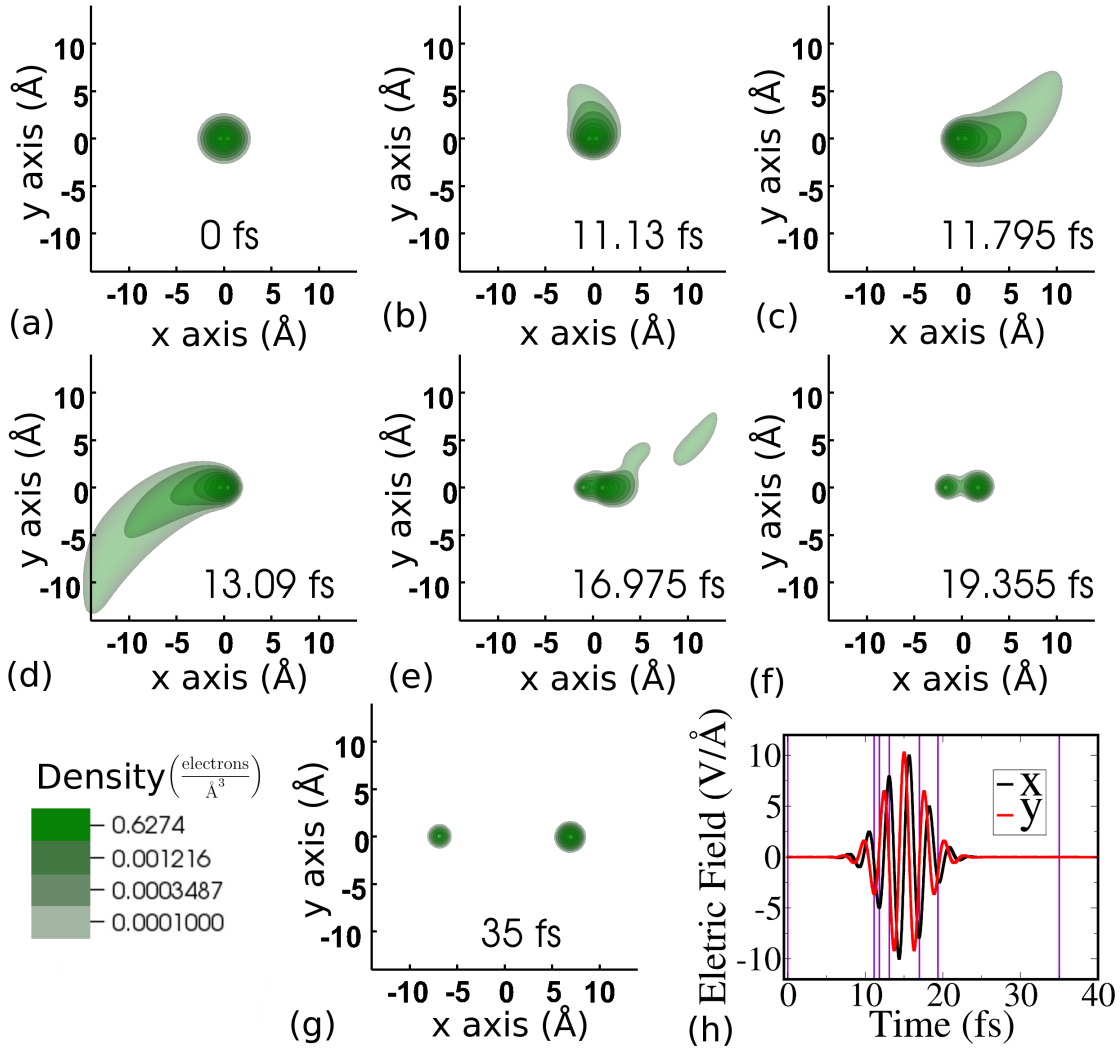

Figure 6.4: (Color online) Time evolution of the electron density of H_2 subjected to a 4.5 fs pulse with a peak intensity of $14 \cdot 10^{14}$W/cm^2 which is circularly polarized with linear components along the x and y axes. The H_2 molecule initially lies along the x axis. (a-g) Snapshots of the electron density of H_2 for various times (h) Plot of the electric field of the two linear components of the circularly polarized laser pulse and of the total number of electrons. Violet vertical lines indicate the times of the snapshots in panels (a-g). The electric field of the circularly polarized pulse rotates clockwise in the $x-y$ plane. As the electric field increases the electron density develops an extended tail, indicating excitation and ionization, which rotates clockwise, lagging somewhat behind the electric field. At 16 fs the ionization rate begins to slow and the Coulomb well of the H^+ ion nearest to the tail recaptures some of the electrons. By 19 fs the electron density localized to the right H^+ ion is visibly greater than that of the left H^+ ion. The molecule dissociates more quickly than the electron density can equilibrate between the two ions, and this asymmetric charge distribution persists until the end of the simulation.

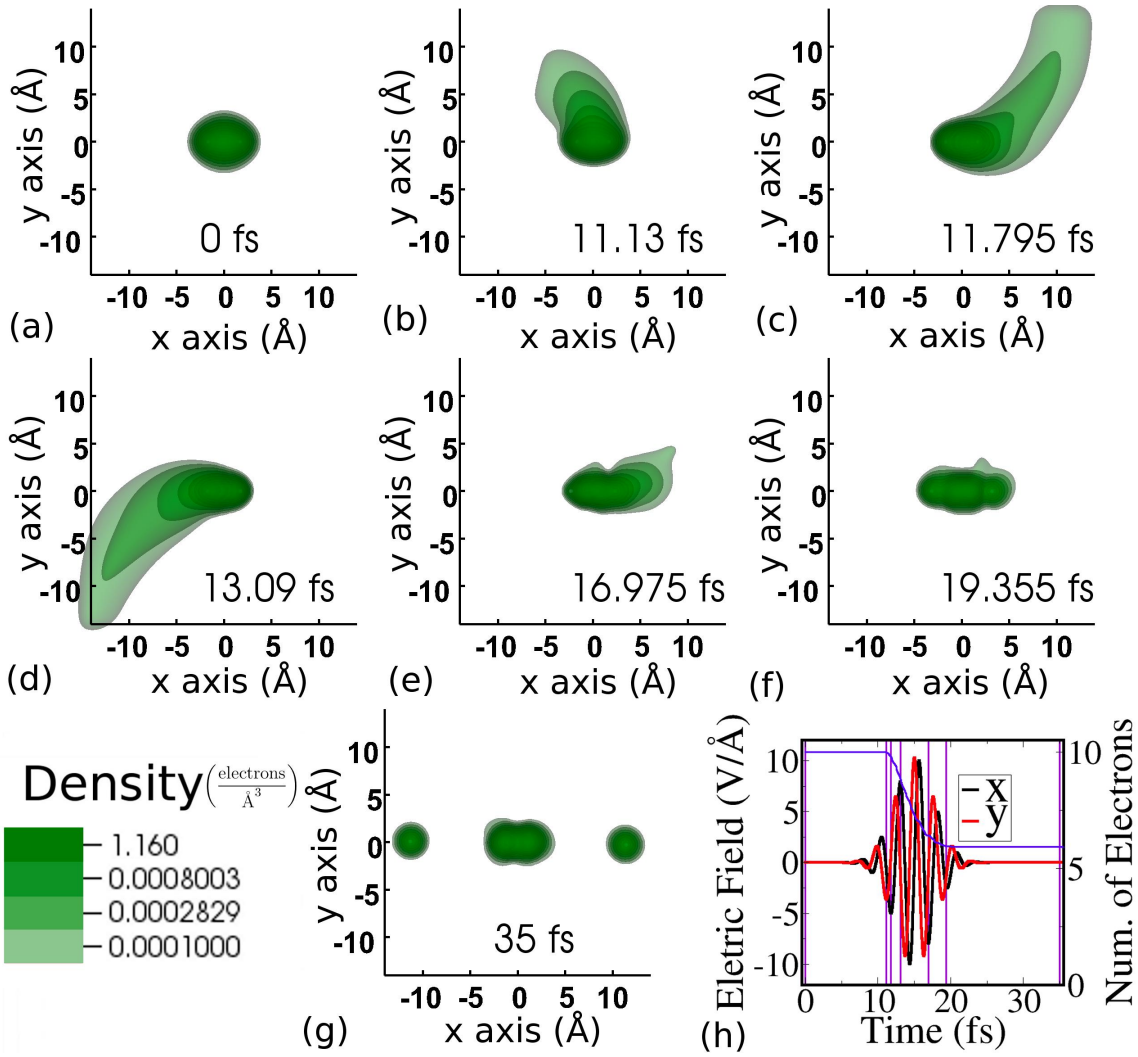

Figure 6.5: (Color online) Time evolution of the electron density of C_2H_2 subjected to a 4.5 fs pulse with a peak intensity of $14 \cdot 10^{14}$W/cm^2 which is circularly polarized with linear components along the x and y axes. The molecule initially lies along the x axis. (a-g) Snapshots of the electron density of C_2H_2 for various times (h) Plot of the electric field of the two linear components of the circularly polarized laser pulse and of the total number of electrons. Violet vertical lines indicate the times of the snapshots in panels (a-g). The electric field of the circularly polarized pulse rotates clockwise in the $x-y$ plane. As the electric field increases the electron density develops an extended tail, indicating excitation and ionization, which rotates clockwise, lagging somewhat behind the electric field.

enhanced ionization occurs. Hence, the ionization of the circularly polarized pulse is much smaller than the sum of the ionization from two individual linearly polarized pulses.

In Fig. 6.2.o, the intensity is $14 \cdot 10^{14} \frac{\mathrm{W}}{\mathrm{cm}^2}$ and the pulse width is 25 fs. The circularly polarized pulse induces an ionization of 5.43 electrons, and the linearly polarized pulse produces an ionization of 4.37 electrons. Both the linearly polarized and circularly polarized pulses cause Coulomb explosion (see Fig. 6.2.p), and hence the ionization of the circularly polarized pulse is much smaller than the sum of the ionization from two individual linearly polarized pulses.

We now turn our attention to the ionization of the individual KS orbitals. Column 2 of Fig. 6.3 shows the ionization induced by the circularly polarized pulses and Column 4 shows the ionization due to the linearly polarized pulses with polarization aligned along the y axis. Due to the symmetry about the molecular axis, the ionization induced by linearly polarized pulses aligned along the z axis would look exactly the same except that the ionization of the $1\pi_{uz}$ and $1\pi_{uy}$ orbitals would be exchanged. Unlike the alignment presented in the previous subsection, the orbital ionization induced by the circularly polarized pulses is qualitatively very similar to the ionization induced by linearly polarized pulses of the same pulse strength. The only notable difference between the circularly and linearly polarized pulses is that the circularly polarized pulse nearly exactly preserves the symmetry between the $1\pi_{uz}$ and $1\pi_{uy}$ orbitals. The time-dependent ionization of these orbitals would be exactly identical if not for the $\frac{\pi}{2}$ phase difference between the two linearly polarized laser pulses that compose the circularly polarized pulse [Eq. (2.36)]. The qualitative similarity of the orbital ionization induced by the circularly and linearly polarized pulses may be attributed to the fact that they do not induce different enhanced ionization dynamics for any of the intensities or durations considered.

6.4 Discussion and Summary

The usual mechanism for nonsequential ionization driven by a linearly polarized pulse is the recollision of electrons with its parent molecule. In this model, the laser pulse first ionizes the electron from the parent molecule and then when the electric field reverses direction it drives the electron back towards its parent molecule. The recolliding electron ionizes additional electrons bound to the parent molecule.

For a circularly polarized pulse there is no reversal of the field. However recollision may occur when the electron is driven along an elliptical path which recollides with the parent molecule [146]. In particular, for a diatomic molecule an electron bound to one nucleus may be driven to the other nucleus where it collides with and ionizes an electron localized at that site. This process is dependent on the internuclear distance, R [137].

Xie et al. [46] experimentally observed the C_2H^+/H^+ fragmentation channel of C_2H_2 induced by a circularly polarized pulses with intensity $3 \cdot 10^{14} \frac{W}{cm^2}$ and a linearly polarized pulse with intensity $4 \cdot 10^{14} \frac{W}{cm^2}$. Both pulses had sub-5fs duration. They find that the yield of high-energy fragments are suppressed for circular polarization, which is attributed to suppression of nonsequential double ionization. At higher intensities ($> 7 \cdot 10^{14} \frac{W}{cm^2}$ and pulse widths ($> 10\,fs$), they find that the high energy fragments are suppressed already for linear polarization. At intensities and pulse durations where sequential ionization is probable for a linearly polarized pulse one would expect to see a suppression of the ions' kinetic energy. At $4 \cdot 10^{14} \frac{W}{cm^2}$ intensity and 4.5 fs pulse duration fragmentation does not occur in our simulations for either H_2 or C_2H_2 (see Fig. 6.1 and 6.2). We therefore cannot compare the ion kinetic energy due to linear and circular polarizations in the regime where nonsequential ionization is probable. At higher intensities and pulse durations, the sequential ionization regime, our simulations show that circular polarization leads to greater ion kinetic energies as compared to linear polarization (see Fig. 6.1 and 6.2). At low intensity and pulse duration, our simulations do not show a fundamental difference in the the ionization dynamics of C_2H_2 for either circularly and linearly polarized pulses.

Wu et al. [147] employed a two-particle coincidence experiment to investigate the dynamics of the ions and electrons of H_2 under the influence of a circularly polarized pulse (35-fs, 790 nm, $1.2{\cdot}10^{14}\frac{\mathrm{W}}{\mathrm{cm}^2}$). They found a moderate asymmetry in the angle-resolved H^+ yield, indicating that electron localization is more probable on one nuclei than the other. In our simulations we observe a small electron localization for H_2 for the two medium strength pulses when the polarization vectors lie on the x and y axes. Fig. 6.4 shows dynamics of the electrons and ions for various times for the pulse with intensity $14{\cdot}10^{14}\frac{\mathrm{W}}{\mathrm{cm}^2}$ and pulse width 4.5 fs. By calculating the integrals $\int_{x>0}\rho\ d^3x$ and $\int_{x<0}\rho\ d^3x$ at t=35 fs, long after the ionization has completed and the molecule has dissociated, we obtain a measure of the number of electrons localized to each ion. For pulse intensity $14{\cdot}10^{14}\frac{\mathrm{W}}{\mathrm{cm}^2}$ and pulse width 4.5 fs, after ionization there are 0.042 electrons remaining with 0.035 electrons localized on the right H^+ ion and 0.007 electrons localized on the left H^+ ion. At intensity $4{\cdot}10^{14}\frac{\mathrm{W}}{\mathrm{cm}^2}$ and pulse width 25 fs, there are 0.011 electrons remaining after ionization with 0.095 electrons on the right ion and 0.011 electrons on the left ion. This moderate asymmetry is in qualitative agreement with the results of Wu et al.

Fig. 6.5 shows snapshots of the ionization and fragmentation of C_2H_2 for the same pulse and alignment considered in Fig. 6.4. The dynamics proceed similarly except in the final few panels. While the asymmetry in the electron localization is not strictly zero, the effect is much smaller compared to the H_2 molecule and cannot be distinguished by sight.

In summary, using TDDFT simulations coupled with the Ehrenfest dynamics we have presented an in depth investigation of the coupled ionization and fragmentation dynamics of H_2 and C_2H_2 for a variety of strong circularly and linearly polarized laser pulses and considered two alignments of the molecular axis relative to the laser polarization. We found that the coupled electron-ion dynamics driven by a circularly polarized pulse of sufficient strength follow the Enhanced Ionization mechanism [113–117] where the pulse stretches the molecule to extended geometries and then the ionization proceeds with greater efficiency. Furthermore we found that the increased of the C-H bond lengths in acetylene

leads to greater ionization efficiency of the inner $3\sigma_g$ and $2\sigma_u$ molecular orbitals, a signature of Enhanced Ionization, in qualitative agreement with the experimental findings of Gong et al. [111]. We also found that the ionization dynamics of the Kohn-Sham orbitals in C_2H_2 depend on the rate at which the C-H bond length increases. Finally, we found that a circularly polarized pulse leads to moderate asymmetric electron localization in the fragmented H_2 molecule, in qualitative agreement with the results of Wu et al. [147]. The present work investigated the interaction of small linear molecules and strong short laser pulses and capture many of the features of interactions with more general molecules. Topics for future work include an investigation of nonlinear or large molecules. The predictions of the present work may be used to motivate future experiments which consider the effects of aligned molecules interacting with strong fields.

Chapter 7

Conclusion

In this thesis we have used ab initio simulations to investigate the coupled and highly correlated dynamics of the electrons and nuclei of small molecules driven by strong short laser fields. Our tool for simulation has been the ab initio time dependent density functional theory coupled with the Ehrenfest dynamics.

In Chapter II we reviewed the density functional theory and time dependent density functional theory formalisms, which are formally exact reformulations of the non-relativistic many-body quantum theory up to the choice of approximation to the exchange-correlation functional. We motivated the use of the non-relativistic time-dependent Kohn-Sham equations of time dependent density functional theory. We further motivated the applicability of the dipole approximation to the description of laser fields at the intensities and wavelengths under consideration. We also introduced the Ehrenfest dynamics to describe the classical trajectories of the nuclei as driven by quantum forces.

In Chapter III we investigated various schemes for constructing the time propagator, which solves the time-dependent Kohn-Sham equations. We found that the Lanczos and spectral propagators promise a greatly reduced computational cost in exchange for a small reduction in accuracy in certain regimes.

In Chapter IV we investigated the ionization and fragmentation of acetylene (C_2H_2) and ethylene (C_2H_4) as driven by linearly polarized strong short laser pulses. An enhanced ionization mechanism, where the ionization efficiency increases with C-H bond lengths, was fully accounted for by the simulations in agreement with many recent experiments. It was shown that the enhanced ionization comes from increased ionization efficiency of inner valence molecular orbitals, and that for certain pulse parameters the ionization of the inner valence orbitals may be greater than the ionization of the highest occupied molecular

orbital. The highest occupied molecular orbital is, in principle, the least bound. The effects of molecular alignment relative to the laser polarization field was also investigated.

In Chapter V we analyzed the origins of the enhanced ionization of acetylene. By projecting the time–dependent Kohn–Sham orbitals of time dependent density functional theory into the lowest unoccupied molecular orbitals (LUMO) calculated by diagonalizing the ground state Hamiltonian of density functional theory, we obtained an estimate of the amount of excitation into excited states. It was found that increasing the C-H bond length increases the probability that electron population will enter the excited states. Increased ionization efficiency from these excited states accounts for the observed enhanced ionization.

The ionization and fragmentation driven by circularly polarized strong short laser fields of acetylene and the hydrogen molecule (H_2) was investigated in chapter VI. These effects of the circularly polarized pulses were compared to the linearly polarized pulses of the same intensity, duration, and wavelength. Just as for the linearly polarized pulses, the enhanced ionization played a critical role in the coupled electron-ion dynamics. Alignment effects were also considered. It was found that certain circularly polarized pulses induces a significant asymmetry in the electron localization.

Time-dependent density functional theory coupled with Ehrenfest dynamics has proved to be very successful in describing the interaction of small molecules with strong, short laser pulses. Nevertheless not all aspects of the complete electron-nuclear dynamics has been captured by this approach. Within the Ehrenfest dynamics the nuclei have well defined positions, and move along classical trajectories which represent some averaging of the available dissociation channels. In reality each dissociation channel has a quantum mechanical probability of occuring. The ion yields of these dissociation channels are obtainable by experiment [112, 116, 148–150]. Quantum interference between dissociation channels has also been observed [151]. A full description of the dynamics requires both the electronic and nuclear wave functions, and the nuclear wave function has been probed

by recent experiments [152–156]. Efficient computational methods to simulate the nuclear wave function is therefore highly desirable. We shall conclude this thesis with a discussion of potential avenues of future research beyond the Ehrenfest dynamics.

The ultimate goal is a non-Born-Oppenheimer approach to calculating the complete many-body wave function. Recall that the Born-Oppenheimer approximation splits the molecular wave function into a direct product of a nuclear and an electronic wave function. Often this partitioning is coupled with an adiabatic approximation where the dynamics of the nuclei are confined to a potential energy surface obtained from ground state electronic structure calculations. The adiabatic approximation may be applied to both wave packet [157, 158] or classical trajectory [159, 160] approaches. This becomes problematic when the potential energy surfaces are close enough in energy that transitions between surfaces are physically permitted, or if there is a conic intersection connecting two surfaces [161, 162]. One solution is to permit surface hopping [163–166], an approach which may be applied to either classical trajectories or nuclear wave packets. We note that the Ehrenfest dynamics is nonadiabatic, and in principle accounts for all electronic excited states.

A non-Born-Oppenheimer approach to the calculation of the full many-body wave function would give the most complete physical picture and the highest accuracy. This approach is necessarily computationally expensive. Attempts to solve the time-dependent Schrödinger equation have been restricted either to one dimension [167–169] or to three dimensions with a model Hamiltonian [170]. Recently a mean-field configuration-interaction method has been developed [171] in which the electronic wave function is propagated in a nuclear mean field, and the nuclear wave function is simulatneously propagated in an electronic mean field. As these non-Born-Oppenheimer approaches become more refined they will offer complete coupled electron-nuclear dynamics of molecules in real-time.

The future of quantum chemistry is immensely promising. Novel theoretical tools will provide a complete quantum mechanical description of the molecular dynamics including all dissociation channels. Attosecond laser pulses shall allow the exploration of a new

frontier on the electronic time scale. These developments suggest that the long standing goal for a quantum control of chemical reactions is swiftly approaching.

BIBLIOGRAPHY

[1] A. Einstein. Über einem die Erzeugung und Verwandlung des Lichtes betreffenden heuristischen Gesichtspunkt. *Annalen der Physik*, 17:132–148, 1905.

[2] T. H. Maiman. Stimulated optical radiation in ruby. *Nature*, 187(4736):493–494, Aug 1960.

[3] A. H. Zewail. Femtochemistry: Atomic-scale dynamics of the chemical bond. *J. Phys. Chem. A*, 104(24):5660–5694, 2000.

[4] F. Krausz and M. Ivanov. Attosecond physics. *Rev. Mod. Phys.*, 81:163–234, 2009.

[5] M. Göppert-Mayer. Über elementarakte mit zwei quantensprüngen. *Annalen der Physik*, 401(3):273–294, 1931.

[6] P. Agostini, F. Fabre, G. Mainfray, G. Petite, and N. K. Rahman. Free-free transitions following six-photon ionization of xenon atoms. *Phys. Rev. Lett.*, 42:1127–1130, Apr 1979.

[7] L. V. Keldysh. Ionization in the field of a strong electromagnetic wave. *Sov. Phys. JETP*, 47:1945, 1965.

[8] T. W. B. Kibble. Refraction of electron beams by intense electromagnetic waves. *Phys. Rev. Lett.*, 16:1054–1056, Jun 1966.

[9] W. Becker, X. Liu, P. J. Ho, and J. H. Eberly. Theories of photoelectron correlation in laser-driven multiple atomic ionization. *Rev. Mod. Phys.*, 84:1011–1043, Jul 2012.

[10] D. N. Fittinghoff, P. R. Bolton, B. Chang, and K. C. Kulander. Observation of nonsequential double ionization of helium with optical tunneling. *Phys. Rev. Lett.*, 69:2642–2645, Nov 1992.

[11] K. Kondo, A. Sagisaka, T. Tamida, Y. Nabekawa, and S. Watanabe. Wavelength dependence of nonsequential double ionization in He. *Phys. Rev. A*, 48:R2531–R2533, Oct 1993.

[12] B. Walker, B. Sheehy, L. F. DiMauro, P. Agostini, K. J. Schafer, and K. C. Kulander. Precision measurement of strong field double ionization of helium. *Phys. Rev. Lett.*, 73:1227–1230, 1994.

[13] A. Talebpour, S. Larochelle, and S. L. Chin. Non-sequential and sequential double ionization of NO in an intense femtosecond Ti:sapphire laser pulse. *Journal of Physics B: Atomic, Molecular and Optical Physics*, 30(7):L245, 1997.

[14] C. Cornaggia and P. Hering. Laser-induced non-sequential double ionization of small molecules. *Journal of Physics B: Atomic, Molecular and Optical Physics*, 31(11):L503, 1998.

[15] P. B. Corkum. Plasma perspective on strong field multiphoton ionization. *Phys. Rev. Lett.*, 71:1994–1997, 1993.

[16] T. Pfeifer, C. Spielmann, and G. Gerber. Femtosecond x-ray science. *Reports on Progress in Physics*, 69(2):443, 2006.

[17] X. M. Tong, Z. X. Zhao, and C. D. Lin. Theory of molecular tunneling ionization. *Phys. Rev. A*, 66:033402, 2002.

[18] M. V. Ammosov, N. B. Delone, and V. P. Krainov. Tunnel ionization of complex atoms and of atomic ions in an alternating electromagnetic field. *Sov. Phys. JETP*, 64:1191, 1986.

[19] A. Talebpour, A. Bandrauk, J. Yang, and S. Chin. Multiphoton ionization of inner-valence electrons and fragmentation of ethylene in an intense Ti:sapphire laser pulse. *Chemical Physics Letters*, 313(5-6):789–794, November 1999.

[20] B. K. McFarland, J. P. Farrell, P. H. Bucksbaum, and M. Ghr. High harmonic generation from multiple orbitals in N2. *Science*, 322(5905):1232–1235, 2008.

[21] H. Akagi, T. Otobe, A. Staudte, A. Shiner, F. Turner, R. Dörner, D. M. Villeneuve, and P. B. Corkum. Laser tunnel ionization from multiple orbitals in HCl. *Science*, 325(5946):1364–1367, 2009.

[22] P. Hoff, I. Znakovskaya, S. Zherebtsov, M. F. Kling, and R. Vivie-Riedle. Effects of multi orbital contributions in the angular-dependent ionization of molecules in intense few-cycle laser pulses. *Applied Physics B*, 98(4):659–666, December 2009.

[23] Z. Wu, C. Wu, X. Liu, Y. Deng, Q. Gong, D. Song, and H. Su. Double ionization of nitrogen from multiple orbitals. *J. Phys. Chem. A*, 114(25):6751–6756, 2010.

[24] A. E. Boguslavskiy, J. Mikosch, A. Gijsbertsen, M. Spanner, S. Patchkovskii, N. Gador, M. J. J. Vrakking, and A. Stolow. The multielectron ionization dynamics underlying attosecond strong-field spectroscopies. *Science*, 335(6074):1336–1340, 2012.

[25] J. Wu, L. Schmidt, M. Kunitski, M. Meckel, S. Voss, H. Sann, H. Kim, T. Jahnke, A. Czasch, and R. Dörner. Multiorbital tunneling ionization of the CO molecule. *Phys. Rev. Lett.*, 108:183001, 2012.

[26] C. Wu, H. Zhang, H. Yang, Q. Gong, D. Song, and H. Su. Tunneling ionization of carbon dioxide from lower-lying orbitals. *Physical Review A*, 83(3):033410, March 2011.

[27] J. Mikosch, A. E. Boguslavskiy, I. Wilkinson, M. Spanner, S. Patchkovskii, and A. Stolow. Channel- and Angle-Resolved Above Threshold Ionization in the Molecular Frame. *Physical Review Letters*, 110(2):023004, January 2013.

[28] S. Weber, M. Oppermann, M. Ivanov, and J. Marangos. Ellipticity dependence of strong field electron recollision for molecular structural imaging. *Journal of Modern Optics*, 60(17):1379–1387, October 2013.

[29] H. Stapelfeldt and T. Seideman. Colloquium: Aligning molecules with strong laser pulses. *Rev. Mod. Phys.*, 75:543–557, 2003.

[30] V. Kumarappan, L. Holmegaard, C. Martiny, C. B. Madsen, T. K. Kjeldsen, S. S. Viftrup, L. B. Madsen, and H. Stapelfeldt. Multiphoton electron angular distributions from laser-aligned CS_2 molecules. *Phys. Rev. Lett.*, 100:093006, 2008.

[31] L. Holmegaard, J. H. Nielsen, I. Nevo, H. Stapelfeldt, F. Filsinger, J. Küpper, and G. Meijer. Laser-induced alignment and orientation of quantum-state-selected large molecules. *Phys. Rev. Lett.*, 102:023001, 2009.

[32] L. Holmegaard, J. L. Hansen, L. Kalhøj, S. L. Kragh, H. Stapelfeldt, F. Filsinger, J. Küpper, G. M. D. Dimitrovski, M. Abu-samha, C. P. J. Martiny, and L. B. Madsen. Photoelectron angular distributions from strong-field ionization of oriented molecules. *Nature Phys.*, 6:428–432, 2010.

[33] C. Z. Bisgaard, O. J. Clarkin, G. Wu, A. M. D. Lee, O. Geßner, C. C. Hayden, and A. Stolow. Time-resolved molecular frame dynamics of fixed-in-space CS_2 molecules. *Science*, 323(5920):1464–1468, 2009.

[34] M. Meckel, D. Comtois, D. Zeidler, A. Staudte, D. Pavičić, H. C. Bandulet, H. Pépin, J. C. Kieffer, R. Dörner, D. M. Villeneuve, and P. B. Corkum. Laser-induced electron tunneling and diffraction. *Science*, 320(5882):1478–1482, 2008.

[35] K. N. Egodapitiya, S. Li, and R. R. Jones. Terahertz-induced field-free orientation of rotationally excited molecules. *Phys. Rev. Lett.*, 112:103002, Mar 2014.

[36] R. Dörner, V. Mergel, O. Jagutzki, L. Spielberger, J. Ullrich, R. Moshammer, and H. Schmidt-Böcking. Cold target recoil ion momentum spectroscopy: a 'momentum microscope' to view atomic collision dynamics. *Physics Reports*, 330:95 – 192, 2000.

[37] C. Brif, R. Chakrabarti, and H. Rabitz. Control of quantum phenomena: past, present and future. *New J. Phys.*, 12(7):075008, 2010.

[38] D. Dong and I. Petersen. Quantum control theory and applications: a survey. *Control Theory Applications, IET*, 4(12):2651–2671, December 2010.

[39] C. Chen, L.-C. Wang, and Y. Wang. Closed-loop and robust control of quantum systems. *The scientific world journal*, 2013, 2013.

[40] W. S. Warren, H. Rabitz, and M. Dahleh. Coherent control of quantum dynamics: the dream is alive. *Science*, 259(5101):1581–1589, 1993.

[41] H. Zhang and H. Rabitz. Robust optimal control of quantum molecular systems in the presence of disturbances and uncertainties. *Phys. Rev. A*, 49:2241–2254, Apr 1994.

[42] R. J. Levis, G. M. Menkir, and H. Rabitz. Selective bond dissociation and rearrangement with optimally tailored, strong-field laser pulses. *Science*, 292(5517):709–713, 2001.

[43] R. J. Levis and H. A. Rabitz. Closing the loop on bond selective chemistry using tailored strong field laser pulses. *J. Phys. Chem. A*, 106(27):6427–6444, 2002.

[44] Y. Liu, X. Liu, Y. Deng, C. Wu, H. Jiang, and Q. Gong. Selective steering of molecular multiple dissociative channels with strong few-cycle laser pulses. *Phys. Rev. Lett.*, 106:073004, 2011.

[45] X. Xie, K. Doblhoff-Dier, S. Roither, M. S. Schöffler, D. Kartashov, H. Xu, T. Rathje, G. G. Paulus, A. Baltuška, S. Gräfe, and M. Kitzler. Attosecond-recollision-controlled selective fragmentation of polyatomic molecules. *Phys. Rev. Lett.*, 109:243001, 2012.

[46] X. Xie, K. Doblhoff-Dier, H. Xu, S. Roither, M. S. Schöffler, D. Kartashov, S. Erattupuzha, T. Rathje, G. G. Paulus, K. Yamanouchi, A. Baltuška, S. Gräfe, and M. Kitzler. Selective control over fragmentation reactions in polyatomic molecules using impulsive laser alignment. *Phys. Rev. Lett.*, 112:163003, 2014.

[47] K. C. Kulander. Multiphoton ionization of hydrogen: A time-dependent theory. *Phys. Rev. A*, 35:445–447, Jan 1987.

[48] X. Tang, H. Rudolph, and P. Lambropoulos. Nonperturbative time-dependent theory of helium in a strong laser field. *Phys. Rev. A*, 44:R6994–R6997, Dec 1991.

[49] M. J. Nandor, M. A. Walker, L. D. Van Woerkom, and H. G. Muller. Detailed comparison of above-threshold-ionization spectra from accurate numerical integrations and high-resolution measurements. *Phys. Rev. A*, 60:R1771–R1774, Sep 1999.

[50] R. Wiehle, B. Witzel, H. Helm, and E. Cormier. Dynamics of strong-field above-threshold ionization of argon: Comparison between experiment and theory. *Phys. Rev. A*, 67:063405, Jun 2003.

[51] M. Awasthi, Y. V. Vanne, A. Saenz, A. Castro, and P. Decleva. Single-active-electron approximation for describing molecules in ultrashort laser pulses and its application to molecular hydrogen. *Phys. Rev. A*, 77:063403, Jun 2008.

[52] S. Petretti, Y. V. Vanne, A. Saenz, A. Castro, and P. Decleva. Alignment-dependent ionization of N_2, O_2, and CO_2 in intense laser fields. *Phys. Rev. Lett.*, 104:223001, Jun 2010.

[53] S. Petretti, A. Saenz, A. Castro, and P. Decleva. Water molecules in ultrashort intense laser fields. *Chemical Physics*, 414:45 – 52, 2013. Attosecond spectroscopy.

[54] A. D. McLACHLAN and M. A. BALL. Time-dependent Hartree-Fock theory for molecules. *Rev. Mod. Phys.*, 36:844–855, Jul 1964.

[55] K. C. Kulander. Time-dependent Hartree-Fock theory of multiphoton ionization: Helium. *Phys. Rev. A*, 36:2726–2738, Sep 1987.

[56] X. Li, S. M. Smith, A. N. Markevitch, D. A. Romanov, R. J. Levis, and H. B. Schlegel. A time-dependent Hartree-Fock approach for studying the electronic optical response of molecules in intense fields. *Phys. Chem. Chem. Phys.*, 7:233–239, 2005.

[57] H. Eshuis, G. G. Balint-Kurti, and F. R. Manby. Dynamics of molecules in strong oscillating electric fields using time-dependent Hartree-Fock theory. *The Journal of Chemical Physics*, 128(11):–, 2008.

[58] E. Lötstedt, T. Kato, and K. Yamanouchi. Enhanced ionization of acetylene in intense laser fields. *Phys. Rev. A*, 85(4):041402, 2012.

[59] E. Lötstedt, T. Kato, and K. Yamanouchi. Efficient ionization of one-dimensional acetylene investigated by time-dependent Hartree-Fock calculations. *Phys. Rev. A*, 86:023401, 2012.

[60] E. Lötstedt, T. Kato, and K. Yamanouchi. Intramolecular electron dynamics in the ionization of acetylene by an intense laser pulse. *J. Chem. Phys.*, 138(10):104304, 2013.

[61] T. Kunert, F. Grossmann, and R. Schmidt. Nonadiabatic dynamics of ethylene in femtosecond laser pulses. *Phys. Rev. A*, 72:023422, Aug 2005.

[62] R. O. Jones. Density functional theory: Its origins, rise to prominence, and future. *Rev. Mod. Phys.*, 87:897–923, Aug 2015.

[63] K. Burke, J. Werschnik, and E. K. U. Gross. Time-dependent density functional theory: Past, present, and future. *J. Chem. Phys.*, 123(6):062206, 2005.

[64] C. A. Ullrich and Z.-h. Yang. A brief compendium of time-dependent density functional theory. *Brazilian Journal of Physics*, 44:154–188, 2014.

[65] F. Wilken and D. Bauer. Adiabatic approximation of the correlation function in the density-functional treatment of ionization processes. *Phys. Rev. Lett.*, 97:203001, Nov 2006.

[66] F. Wilken and D. Bauer. Momentum distributions in time-dependent density-functional theory: Product-phase approximation for nonsequential double ionization in strong laser fields. *Phys. Rev. A*, 76:023409, Aug 2007.

[67] X.-M. Tong and S.-I. Chu. Time-dependent density-functional theory for strong-field multiphoton processes: Application to the study of the role of dynamical electron correlation in multiple high-order harmonic generation. *Phys. Rev. A*, 57:452–461, Jan 1998.

[68] X. Chu and S.-I. Chu. Time-dependent density-functional theory for molecular processes in strong fields: Study of multiphoton processes and dynamical response of individual valence electrons of N_2 in intense laser fields. *Phys. Rev. A*, 64(6):063404, 2001.

[69] E. P. Fowe and A. D. Bandrauk. Nonlinear time-dependent density-functional-theory study of ionization and harmonic generation in CO_2 by ultrashort intense laser pulses: Orientational effects. *Phys. Rev. A*, 81:023411, 2010.

[70] E. Livshits and R. Baer. Time-dependent density-functional studies of the D_2 coulomb explosion. *J. Phys. Chem. A*, 110(27):8443–8450, 2006.

[71] M. Isla and J. A. Alonso. Interaction of the charged deuterium cluster D_3^+ with femtosecond laser pulse. *J. Phys. Chem. C*, 111(48):17765–17772, 2007.

[72] S. Bubin, M. Atkinson, K. Varga, X. Xie, S. Roither, D. Kartashov, A. Baltuška, and M. Kitzler. Strong laser-pulse-driven ionization and Coulomb explosion of hydrocarbon molecules. *Phys. Rev. A*, 86:043407, 2012.

[73] J. Haruyama, C. Hu, and K. Watanabe. First-principles molecular-dynamics simulation of biphenyl under strong laser pulses by time-dependent density-functional theory. *Phys. Rev. A*, 85:062511, 2012.

[74] Y. Kawashita, T. Nakatsukasa, and K. Yabana. Time-dependent density-functional theory simulation for electron–ion dynamics in molecules under intense laser pulses. *J. Phys. Condens. Matter*, 21(6):064222, 2009.

[75] H. Eschrig. *The fundamentals of density functional theory*, volume 32. Springer, 1996.

[76] P. Hohenberg and W. Kohn. Inhomogeneous electron gas. *Phys. Rev.*, 136(3B):B864–B871, 1964.

[77] W. Kohn and L. J. Sham. Self-consistent equations including exchange and correlation effects. *Phys. Rev.*, 140(4A):A1133–A1138, 1965.

[78] S. F. Sousa, P. A. Fernandes, and M. J. Ramos. General performance of density functionals. *The Journal of Physical Chemistry A*, 111(42):10439–10452, 2007. PMID: 17718548.

[79] J. P. Perdew and A. Zunger. Self-interaction correction to density-functional approximations for many-electron systems. *Phys. Rev. B*, 23(10):5048–5079, 1981.

[80] H. L. Schmider and A. D. Becke. Optimized density functionals from the extended G2 test set. *The Journal of Chemical Physics*, 108(23):9624–9631, 1998.

[81] O. A. Vydrov and T. Van Voorhis. Nonlocal van der Waals density functional made simple. *Phys. Rev. Lett.*, 103:063004, Aug 2009.

[82] E. Runge and E. K. U. Gross. Density-functional theory for time-dependent systems. *Phys. Rev. Lett.*, 52(12):997–1000, 1984.

[83] M. E. Casida. Time-dependent density-functional response theory for molecules. *Recent advances in density functional methods*, 1:155, 1995.

[84] N. T. Maitra, I. Souza, and K. Burke. Current-density functional theory of the response of solids. *Phys. Rev. B*, 68:045109, Jul 2003.

[85] S. K. Ghosh and A. K. Dhara. Density-functional theory of many-electron systems subjected to time-dependent electric and magnetic fields. *Phys. Rev. A*, 38:1149–1158, Aug 1988.

[86] H. R. Reiss. Limits on tunneling theories of strong-field ionization. *Phys. Rev. Lett.*, 101:043002, 2008.

[87] H. R. Reiss. Unsuitability of the Keldysh parameter for laser fields. *Phys. Rev. A*, 82:023418, 2010.

[88] E. S. Sarachik and G. T. Schappert. Classical theory of the scattering of intense laser radiation by free electrons. *Phys. Rev. D*, 1:2738–2753, May 1970.

[89] F. Ding, W. Liang, C. T. Chapman, C. M. Isborn, and X. Li. On the gauge invariance of nonperturbative electronic dynamics using the time-dependent Hartree-Fock and time-dependent Kohn-Sham. *The Journal of Chemical Physics*, 135(16):–, 2011.

[90] D. H. Kobe. Gauge transformations and the electric dipole approximation. *American Journal of Physics*, 50(2):128–133, 1982.

[91] H. R. Reiss. Dipole-approximation magnetic fields in strong laser beams. *Phys. Rev. A*, 63:013409, Dec 2000.

[92] D. Marx and J. Hutter. Ab initio molecular dynamics: Theory and implementation. *Modern methods and algorithms of quantum chemistry*, 1:301–449, 2000.

[93] M. Born and R. Oppenheimer. Zur quantentheorie der molekeln. *Annalen der Physik*, 389(20):457–484, 1927.

[94] P. Ehrenfest. Bemerkung über die angenäherte Gültigkeit der klassischen Mechanik innerhalb der Quantenmechanik. *Z. Phys.*, 45:455–457, 1927.

[95] D. E. Manolopoulos. Derivation and reflection properties of a transmission-free absorbing potential. *J. Chem. Phys.*, 117:9552, 2002.

[96] N. Troullier and J. L. Martins. Efficient pseudopotentials for plane-wave calculations. *Phys. Rev. B*, 43(3):1993–2006, 1991.

[97] A. L. Fetter and J. D. Walecka. *Quantum theory of many-particle systems*. Courier Corporation, 2003.

[98] A. Castro, M. A. L. Marques, and A. Rubio. Propagators for the time-dependent Kohn–Sham equations. *J. Chem. Phys.*, 121(8):3425–3433, 2004.

[99] H. Tal-Ezer and R. Kosloff. An accurate and efficient scheme for propagating the time dependent Schrödinger equation. *J. Chem. Phys.*, 81:3967–3971, 1984.

[100] S. Bubin and K. Varga. Electron and ion dynamics in graphene and graphane fragments subjected to high-intensity laser pulses. *Phys. Rev. B*, 85:205441, 2012.

[101] S. Bubin and K. Varga. First-principles time-dependent simulation of laser assisted desorption of hydrogen atoms from H-Si(111) surface. *Appl. Phys. Lett.*, 98(15):154101, 2011.

[102] S. Bubin and K. Varga. Electron-ion dynamics in laser-assisted desorption of hydrogen atoms from H-Si(111) surface. *J. Appl. Phys.*, 110(6):064905, 2011.

[103] S. Bubin, B. Wang, S. Pantelides, and K. Varga. Simulation of high-energy ion collisions with graphene fragments. *Phys. Rev. B*, 85:235435, 2012.

[104] A. Russakoff, S. Bubin, X. Xie, S. Erattupuzha, M. Kitzler, and K. Varga. Time-dependent density-functional study of the alignment-dependent ionization of acetylene and ethylene by strong laser pulses. *Phys. Rev. A*, 91:023422, Feb 2015.

[105] C. Lanczos. *An iteration method for the solution of the eigenvalue problem of linear differential and integral operators*. United States Governm. Press Office, 1950.

[106] J. Crank and P. Nicolson. A practical method for numerical evaluation of solutions of partial differential equations of the heat-conduction type. *Math. Proc. Cambridge Philos. Soc.*, 43(01):50–67, 1947.

[107] B. Manschwetus, T. Nubbemeyer, K. Gorling, G. Steinmeyer, U. Eichmann, H. Rottke, and W. Sandner. Strong laser field fragmentation of h_2: Coulomb explosion without double ionization. *Phys. Rev. Lett.*, 102:113002, 2009.

[108] P. von den Hoff, I. Znakovskaya, M. F. Kling, and R. de Vivie-Riedle. Attosecond control of the dissociative ionization via electron localization: A comparison between D_2 and CO. *Chem. Phys.*, 366(1-3):139–147, 2009.

[109] G. Sansone, F. Kelkensberg, J. F. Perez-Torres, F. Morales, M. F. Kling, W. Siu, O. Ghafur, P. Johnsson, M. Swoboda, E. Benedetti, F. Ferrari, F. Lepine, J. L. Sanz-Vicario, S. Zherebtsov, I. Znakovskaya, A. L'Huillier, M. Y. Ivanov, M. Nisoli, F. Martin, and M. J. J. Vrakking. Electron localization following attosecond molecular photoionization. *Nature (London)*, 465(7299):763–766, 2010.

[110] I. Bocharova, R. Karimi, E. F. Penka, J.-P. Brichta, P. Lassonde, X. Fu, J.-C. Kieffer, A. D. Bandrauk, I. Litvinyuk, J. Sanderson, and F. Légaré. Charge resonance enhanced ionization of CO_2 probed by laser coulomb explosion imaging. *Phys. Rev. Lett.*, 107:063201, 2011.

[111] X. Gong, Q. Song, Q. Ji, H. Pan, J. Ding, J. Wu, and H. Zeng. Strong-field dissociative double ionization of acetylene. *Phys. Rev. Lett.*, 112:243001, 2014.

[112] X. Xie, S. Roither, M. Schöffler, E. Lötstedt, D. Kartashov, L. Zhang, G. G. Paulus, A. Iwasaki, A. Baltuška, K. Yamanouchi, and M. Kitzler. Electronic predetermination of ethylene fragmentation dynamics. *Phys. Rev. X*, 4:021005, 2014.

[113] T. Seideman, M. Y. Ivanov, and P. B. Corkum. Role of electron localization in intense-field molecular ionization. *Phys. Rev. Lett.*, 75:2819–2822, 1995.

[114] T. Zuo and A. D. Bandrauk. Charge-resonance-enhanced ionization of diatomic molecular ions by intense lasers. *Phys. Rev. A*, 52:R2511–R2514, Oct 1995.

[115] D. M. Villeneuve, M. Y. Ivanov, and P. B. Corkum. Enhanced ionization of diatomic molecules in strong laser fields: A classical model. *Phys. Rev. A*, 54:736–741, 1996.

[116] S. Roither, X. Xie, D. Kartashov, L. Zhang, M. Schöffler, H. Xu, A. Iwasaki, T. Okino, K. Yamanouchi, A. Baltuska, and M. Kitzler. High energy proton ejection from hydrocarbon molecules driven by highly efficient field ionization. *Phys. Rev. Lett.*, 106:163001, 2011.

[117] X. Xie, S. Roither, M. Schöffler, H. Xu, S. Bubin, E. Lötstedt, S. Erattuphuza, A. Iwasaki, D. Kartashov, K. Varga, G. G. Paulus, A. Baltuška, K. Yamanouchi, and M. Kitzler. Role of proton dynamics in efficient photoionization of hydrocarbon molecules. *Phys. Rev. A*, 89:023429, Feb 2014.

[118] K. Codling, L. J. Frasinski, and P. A. Hatherly. On the field ionisation of diatomic molecules by intense laser field. *J. Phys. B*, 22(12):L321, 1989.

[119] D. Dimitrovski, C. P. J. Martiny, and L. B. Madsen. Strong-field ionization of polar molecules: Stark-shift-corrected strong-field approximation. *Phys. Rev. A*, 82:053404, 2010.

[120] M.-P. Gaigeot, P. Lopez-Tarifa, F. Martin, M. Alcami, R. Vuilleumier, I. Tavernelli, M.-A. H. du Penhoat, and M.-F. Politis. Theoretical investigation of the ultrafast dissociation of ionised biomolecules immersed in water: Direct and indirect effects. *Mutat. Res. Rev. Mutat. Res.*, 704(1-3):45–53, 2010. ESF-EMBO Conference: Spatio-Temporal Radiation Biology: Transdisciplinary Advances for Biomedical Applications.

[121] A. Debnarova, S. Techert, and S. Schmatz. Limitations of high-intensity soft X-ray laser fields for the characterisation of water chemistry: Coulomb explosion of the octamer water cluster. *Phys. Chem. Chem. Phys.*, 14:9606–9614, 2012.

[122] P. J. Linstrom and W. G. Mallard, editors. *NIST Chemistry WebBook, NIST Standard Reference Database Number 69*. National Institute of Standards and Technology, Gaithersburg MD, 20899, 2001.

[123] I. V. Litvinyuk, F. Légaré, P. W. Dooley, D. M. Villeneuve, P. B. Corkum, J. . Zanghellini, A. Pegarkov, C. Fabian, and T. Brabec. Shakeup excitation during optical tunnel ionization. *Phys. Rev. Lett.*, 94:033003, Jan 2005.

[124] W. A. Bryan, S. L. Stebbings, J. McKenna, E. M. L. English, M. Suresh, J. Wood, B. Srigengan, I. C. E. Turcu, J. M. Smith, E. J. Divall, C. J. Hooker, A. J. Langley, J. L. Collier, I. D. Williams, and W. R. Newell. Atomic excitation during recollision-free ultrafast multi-electron tunnel ionization. *Nature Physics*, 2(6):379–383, 2006.

[125] T. Kanai, S. Minemoto, and H. Sakai. Quantum interference during high-order harmonic generation from aligned molecules. *Nature*, 435(7041):470–474, May 2005.

[126] W. Li, X. Zhou, R. Lock, S. Patchkovskii, A. Stolow, H. C. Kapteyn, and M. M. Murnane. Time-resolved dynamics in N2O4 probed using high harmonic generation. *Science*, 322(5905):1207–1211, 2008.

[127] X. Zhou, R. Lock, W. Li, N. Wagner, M. M. Murnane, and H. C. Kapteyn. Molecular recollision interferometry in high harmonic generation. *Phys. Rev. Lett.*, 100:073902, Feb 2008.

[128] W. Boutu, S. Haessler, H. Merdji, P. Breger, G. Waters, M. Stankiewicz, L. J. Frasinski, R. Taieb, J. Caillat, A. Maquet, P. Monchicourt, B. Carre, and P. Salieres. Coherent control of attosecond emission from aligned molecules. *Nature Physics*, 4(7):545–549, 2008.

[129] O. Smirnova, Y. Mairesse, S. Patchkovskii, N. Dudovich, D. Villeneuve, P. Corkum, and M. Y. Ivanov. High harmonic interferometry of multi-electron dynamics in molecules. *Nature*, 460(7258):972–7, August 2009.

[130] A. N. Pfeiffer, C. Cirelli, M. Smolarski, R. Dorner, and U. Keller. Timing the release in sequential double ionization. *Nat Phys*, 7(5):428–433, May 2011.

[131] Y. Zhou, C. Huang, Q. Liao, and P. Lu. Classical simulations including electron correlations for sequential double ionization. *Phys. Rev. Lett.*, 109:053004, Aug 2012.

[132] W. Becker and H. Rottke. Many-electron strong-field physics. *Contemp. Phys.*, 49(3):199–223, 2008.

[133] R. Dörner, T. Weber, M. Weckenbrock, A. Staudte, M. Hattass, R. Moshammer,

J. Ullrich, and H. Schmidt-Bocking. Multiple ionization in strong laser fields. *Advances in Atomic Molecular and Optical Physics*, 48:1–35, 2002.

[134] B. Walker, E. Mevel, B. Yang, P. Breger, J. P. Chambaret, A. Antonetti, L. F. DiMauro, and P. Agostini. Double ionization in the perturbative and tunneling regimes. *Phys. Rev. A*, 48:R894–R897, Aug 1993.

[135] P. B. Corkum. Recollision physics. *Phys. Today*, 64(3):36–41, 2011.

[136] C. Guo, M. Li, J. P. Nibarger, and G. N. Gibson. Single and double ionization of diatomic molecules in strong laser fields. *Phys. Rev. A*, 58:R4271–R4274, Dec 1998.

[137] A. Tong, Y. Zhou, C. Huang, and P. Lu. Electron dynamics of molecular double ionization by circularly polarized laser pulses. *The Journal of Chemical Physics*, 139(7):–, 2013.

[138] K.-J. Yuan and A. D. Bandrauk. High-order elliptically polarized harmonic generation in extended molecules with ultrashort intense bichromatic circularly polarized laser pulses. *Phys. Rev. A*, 81:063412, Jun 2010.

[139] X. Ren, J. Zhang, P. Liu, Y. Wang, and Z. Xu. Ionization suppression of diatomic molecules in strong laser fields. *Phys. Rev. A*, 78:043411, Oct 2008.

[140] K.-J. Yuan and A. D. Bandrauk. Photoelectron angular distributions of H+ 2 and HHe2+ by intense circularly polarized extreme ultraviolet laser pulses. *Journal of Physics B: Atomic, Molecular and Optical Physics*, 45(10):105601, 2012.

[141] A. Staudte, S. Patchkovskii, D. Pavičić, H. Akagi, O. Smirnova, D. Zeidler, M. Meckel, D. M. Villeneuve, R. Dörner, M. Y. Ivanov, and P. B. Corkum. Angular tunneling ionization probability of fixed-in-space H_2 molecules in intense laser pulses. *Phys. Rev. Lett.*, 102:033004, Jan 2009.

[142] P. B. Corkum, N. H. Burnett, and F. Brunel. Above-threshold ionization in the long-wavelength limit. *Phys. Rev. Lett.*, 62:1259–1262, Mar 1989.

[143] M. Odenweller, N. Takemoto, A. Vredenborg, K. Cole, K. Pahl, J. Titze, L. P. H. Schmidt, T. Jahnke, R. Dörner, and A. Becker. Strong field electron emission from fixed in space H_2^+ ions. *Phys. Rev. Lett.*, 107:143004, Sep 2011.

[144] M. Odenweller, J. Lower, K. Pahl, M. Schütt, J. Wu, K. Cole, A. Vredenborg, L. P. Schmidt, N. Neumann, J. Titze, T. Jahnke, M. Meckel, M. Kunitski, T. Havermeier, S. Voss, M. Schöffler, H. Sann, J. Voigtsberger, H. Schmidt-Böcking, and R. Dörner. Electron emission from $H_2{}^+$ in strong laser fields. *Phys. Rev. A*, 89:013424, Jan 2014.

[145] A. D. Bandrauk and H. Lu. Generalized space translation and new numerical methods for time-dependent Schroedinger equations of molecules in intense laser fields. *Journal of Molecular Structure: THEOCHEM*, 547(1):97–111, 2001.

[146] X. Wang and J. H. Eberly. Elliptical trajectories in nonsequential double ionization. *New Journal of Physics*, 12(9):093047, 2010.

[147] J. Wu, M. Magrakvelidze, L. P. H. Schmidt, M. Kunitski, T. Pfeifer, M. Schöffler, M. Pitzer, M. Richter, S. Voss, H. Sann, H. Kim, J. Lower, T. Jahnke, A. Czasch, U. Thumm, and R. Dörner. Understanding the role of phase in chemical bond breaking with coincidence angular streaking. *Nat Commun*, 4(2177), Jul 2013. Article.

[148] C. Cornaggia, D. Normand, and J. Morellec. Role of the molecular electronic configuration in the Coulomb fragmentation of N_2 , C_2H_2 and C_2H_4 in an intense laser field. *J. Phys. B*, 25(17):L415–L422, 1992.

[149] C. Cornaggia, M. Schmidt, and D. Normand. Laser-induced nuclear motions in the Coulomb explosion of $C_2H_2^+$ ions. *Phys. Rev. A*, 51(2):1431–1437, 1995.

[150] L. Zhang, S. Roither, X. Xie, D. Kartashov, M. Schöffler, H. Xu, A. Iwasaki, S. Gräfe, T. Okino, K. Yamanouchi, A. Baltuska, and M. Kitzler. Path-selective investigation of intense laser-pulse-induced fragmentation dynamics in triply charged 1,3-butadiene. *J. Phys. B*, 45(8):085603, 2012.

[151] B. Fischer, M. Kremer, T. Pfeifer, B. Feuerstein, V. Sharma, U. Thumm, C. D. Schröter, R. Moshammer, and J. Ullrich. Steering the electron in $H_2{}^+$ by nuclear wave packet dynamics. *Phys. Rev. Lett.*, 105:223001, Nov 2010.

[152] C. I. Blaga, J. Xu, A. D. DiChiara, E. Sistrunk, K. Zhang, P. Agostini, T. A. Miller, L. F. DiMauro, and C. D. Lin. Imaging ultrafast molecular dynamics with laser-induced electron diffraction. *Nature*, 483(7388):194–197, march 2012.

[153] S. De, M. Magrakvelidze, I. A. Bocharova, D. Ray, W. Cao, I. Znakovskaya, H. Li, Z. Wang, G. Laurent, U. Thumm, M. F. Kling, I. V. Litvinyuk, I. Ben-Itzhak, and C. L. Cocke. Following dynamic nuclear wave packets in N_2, O_2, and CO with few-cycle infrared pulses. *Phys. Rev. A*, 84:043410, Oct 2011.

[154] T. Ergler, A. Rudenko, B. Feuerstein, K. Zrost, C. D. Schröter, R. Moshammer, and J. Ullrich. Spatiotemporal imaging of ultrafast molecular motion: Collapse and revival of the $D_2{}^+$ nuclear wave packet. *Phys. Rev. Lett.*, 97:193001, Nov 2006.

[155] M. Magrakvelidze, O. Herrwerth, Y. H. Jiang, A. Rudenko, M. Kurka, L. Foucar, K. U. Kühnel, M. Kübel, N. G. Johnson, C. D. Schröter, S. Düsterer, R. Treusch, M. Lezius, I. Ben-Itzhak, R. Moshammer, J. Ullrich, M. F. Kling, and U. Thumm. Tracing nuclear-wave-packet dynamics in singly and doubly charged states of N_2 and O_2 with XUV-pumpˇXUV-probe experiments. *Phys. Rev. A*, 86:013415, Jul 2012.

[156] S. Baker, J. S. Robinson, C. A. Haworth, H. Teng, R. A. Smith, C. C. Chirila,

M. Lein, J. W. G. Tisch, and J. P. Marangos. Probing proton dynamics in molecules on an attosecond time scale. *Science*, 312(5772):424–427, 2006.

[157] D. Yang and S.-L. Cong. Nuclear interference in dissociating of HD^+ in ultrashort laser fields. *Phys. Rev. A*, 84:013424, Jul 2011.

[158] V. Mezoui Ndo, L. O. Owono, B. Piraux, S. Barmaki, M. Førre, and H. Bachau. Nuclear interference processes in the dissociation of H_2^+ in short vuv laser fields. *Phys. Rev. A*, 86:013416, Jul 2012.

[159] B. T. Psciuk, P. Tao, and H. B. Schlegel. Ab initio classical trajectory study of the fragmentation of C_3H_4 dications on the singlet and triplet surfaces. *J. Phys. Chem. A*, 114(29):7653–7660, 2010.

[160] S. K. Lee, W. Li, and H. B. Schlegel. HCO^+ dissociation in a strong laser field: An ab initio classical trajectory study. *Chem. Phys. Lett.*, 536:14–18, 2012.

[161] D. R. Yarkony. Diabolical conical intersections. *Rev. Mod. Phys.*, 68:985–1013, Oct 1996.

[162] G. J. Halász, A. Vibók, H.-D. Meyer, and L. S. Cederbaum. Effect of light-induced conical intersection on the photodissociation dynamics of the D_2^+ molecule. *J. Phys. Chem. A*, 117:8528–8535, 2013.

[163] J. C. Tully and R. K. Preston. Trajectory surface hopping approach to nonadiabatic molecular collisions: The reaction of H^+ with D_2. *J. Chem. Phys.*, 55(2):562–572, 1971.

[164] C. F. Craig, W. R. Duncan, and O. V. Prezhdo. Trajectory surface hopping in the time-dependent Kohn-Sham approach for electron-nuclear dynamics. *Phys. Rev. Lett.*, 95(16):163001, 2005.

[165] E. Tapavicza, I. Tavernelli, and U. Rothlisberger. Trajectory surface hopping within linear response time-dependent density-functional theory. *Phys. Rev. Lett.*, 98(2):023001, 2007.

[166] B. R. Landry and J. E. Subotnik. How to recover Marcus theory with fewest switches surface hopping: Add just a touch of decoherence. *J. Chem. Phys.*, 137(22):22A513, 2012.

[167] A. D. Bandrauk and S. Chelkowski. Dynamic imaging of nuclear wave functions with ultrashort UV laser pulses. *Phys. Rev. Lett.*, 87:273004, Dec 2001.

[168] T. Bredtmann, S. Chelkowski, and A. D. Bandrauk. Monitoring attosecond dynamics of coherent electron-nuclear wave packets by molecular high-order-harmonic generation. *Phys. Rev. A*, 84:021401, Aug 2011.

[169] S. Chelkowski, A. D. Bandrauk, A. Staudte, and P. B. Corkum. Dynamic nuclear interference structures in the Coulomb explosion spectra of a hydrogen molecule in intense laser fields: Reexamination of molecular enhanced ionization. *Phys. Rev. A*, 76:013405, Jul 2007.

[170] I. Kawata, H. Kono, and Y. Fujimura. Adiabatic and diabatic responses of H2+ to an intense femtosecond laser pulse: Dynamics of the electronic and nuclear wave packet. *The Journal of Chemical Physics*, 110(23):11152–11165, 1999.

[171] P. Cassam-Chenaï, B. Suo, and W. Liu. Decoupling electrons and nuclei without the Born-Oppenheimer approximation: The electron-nucleus mean-field configuration-interaction method. *Phys. Rev. A*, 92:012502, Jul 2015.